

# 國立交通大學

## 環境工程研究所

### 博士論文

以常壓電漿輔助程序製造氮摻雜二氧化鈦可見光觸媒奈  
米微粒之研究



Production of N-doped TiO<sub>2</sub> Photocatalysts by Atmospheric Pressure

Plasma Enhanced Nanoparticle Synthesis Process

研究生：陳建志

指導教授：白曠綾 教授

中華民國九十六年九月

以常壓電漿輔助程序製造氮摻雜二氧化鈦可見光觸媒奈米微粒之研究

Production of N-doped TiO<sub>2</sub> Photocatalysts by Atmospheric Pressure

Plasma Enhanced Nanoparticle Synthesis Process

研究生：陳建志

Student : Chienchih Chen

指導教授：白曠綾

Advisor : Hsunling Bai

國立交通大學



Submitted to Institute of Environmental Engineering

College of Engineering

National Chiao Tung University

in partial Fulfillment of the Requirements

for the Degree of Doctor of Philosophy

in Environmental Engineering

September 2007

Hsinchu, Taiwan

中華民國九十六年九月

## 中文摘要

本研究目的為利用常壓電漿輔助奈米微粒製造程序 (Atmospheric Pressure Plasma Enhanced Nanoparticle Synthesis; APPENS) 製造均勻粒徑之 N 摻雜 TiO<sub>2</sub> 奈米微粒，其可為能源材料或光觸媒使用，此外亦可應用作為均勻氣膠產生器(monodisperse aerosol generator)，提供對奈米顆粒健康效應等研究者一個簡易的奈米微粒即時產生源。

本研究利用自行開發之 APPENS 系統，在常溫常壓下，藉由各種不同製程條件之電漿反應器系統產生奈米微粒，再將所得之微粒利用 SEM、TEM、XPS、XRD 等儀器分析微粒之物理化學特性。研究結果顯示，本程序所合成之光觸媒微粒粒徑分佈約為 20nm~40nm。經過 XRD 及 XPS 分析後確認為含氮摻雜之 anatase TiO<sub>2</sub>。將製造所得之光觸媒以甲苯及異丙醇為揮發性有機物指標物種進行紫外光及可見光光催化批次反應，結果顯示本研究之觸媒在以可見光光源照射 40 分鐘，對甲苯及異丙醇分別有 40% 及 100% 去除效率，而在紫外光下對甲苯效率則提升為 60%，對異丙醇則在 30 分鐘內達到 100%。利用連續式光催化反應來比較本研究製造得之光觸媒與商用光觸媒(P-25、ST01)之活性，結果顯示在可見光照下確實有較優於商用觸媒之去除效率。本研究亦探討在不同製程條件下製造各種不同氮摻雜光觸媒之表面鍵結特性，研究顯示可見光觸媒表面鍵結型態為影響光催化活性之關鍵，O<sub>x</sub>-Ti-N<sub>y</sub> 型態摻雜 (doping) 對可見光的催化效果較 Ti-(NO) 為佳，而無論是 Ti-N、Ti-N 及 O<sub>x</sub>-Ti-N<sub>y</sub> 型態的氮摻雜 都有可見光的催化效果，Ti-(NO<sub>2</sub>) 型態的氮摻雜則可能會對可見光的催化效果有負影響。

研究中並針對合成程序條件對生成微粒之影響，發現在無電漿環境下形成的可見光觸媒微粒會成雙峰分佈，其平均粒徑為 100 nm 及 400 nm; 而在電場強度 9.6 kV/cm 之電漿環境下形成之微粒則成單峰分佈，粒徑大小依不同前驅物濃度而改變，範圍約在 30-60 nm 左右，此外改變不同電場強度及頻率亦會改變粒徑的分佈。本研究結果顯示本系統不僅能製造出高均勻度之奈米微粒，且該電漿系統具有參數調整容易之優點，可迅速的產生所需粒徑之奈米微粒，且在可見光觸媒製造上可獲致品質佳且較其他製程應用性更廣之成品。

關鍵字：常壓低溫電漿、奈米微粒、光觸媒、可見光、二氧化鈦、奈米微粒、氣膠產生器、燃料電池材料、太陽能電池材料、VOCs。

## ABSTRACT

An Atmospheric Pressure Plasma Enhanced Nanoparticle Synthesis (APPENS) process was proposed to produce nitrogen doped (N-doped) titanium dioxide ( $\text{TiO}_2$ ) visible light photocatalyst. The effect of N-doping statuses on the photocatalytic activity of N-doped  $\text{TiO}_2$  photocatalysts was investigated. The potential application of APPENS reactor as an aerosol generator was studied.

The results showed that photocatalytic activity of the N-doped  $\text{TiO}_2$  photocatalyst is higher than the commercial ST01 and P25 photocatalysts in terms of toluene removals in a continuous flow reactor. The light absorption in the visible light range for N-doped  $\text{TiO}_2$  was also confirmed by a clear red shift of the UV-visible spectra. The N-doped  $\text{TiO}_2$  particles with  $\text{O}_x\text{-Ti-N}_y$  and  $\text{-(NO)}$  dopants are produced via  $\text{N}_2$  plasma gas followed by air or  $\text{N}_2$  annealing gases. They have better visible and UV photocatalytic activities as compared to the pure  $\text{TiO}_2$  photocatalysts prepared under  $\text{O}_2/\text{Ar}$  plasma and annealing gases. The results reveal that the  $\text{O}_x\text{-Ti-N}_y$  and  $\text{-(NO)}$  dopants may have positive effects on the visible light photocatalytic activity while the  $\text{-(NO}_2)$  dopant tends to have a negative effect on the visible light photocatalytic activity.

For the aerosol generator employs the APPENS process of alternative current (AC), the influences of applied voltage, frequency and molar ratios of precursor on the generated particles were characterized by the SEM, XRD and SMPS analyses. Results showed that  $\text{TiO}_2$  nanoparticles appear to be in a broad size range of bi-modal distribution when no voltage is applied. After applying the AC plasma, uni-modal distribution with average sizes range of 30-60 nm was observed. The applied electric frequency can be adjusted to either generate nanoparticles after the plasma reactor or develop a thin film in the reactor. An increase in the precursor molar ratio leads to larger particles with a broader size distribution.

Keywords: visible light photocatalyst, photocatalysis, nonthermal plasma, dielectric barrier discharge, titania nanoparticles, plasma enhanced chemical vapor deposition, aerosol generator, binding energy.

## ACKNOWLEDGEMENTS

研究期間承蒙恩師 白曠綾博士於修習階段之諄諄教誨，與不厭其煩地對於研究及論文上的悉心指導與叮囑，方使論文得以順利完成，尤其是對於做人處事的道理更使我獲益良多，僅此致上最誠摯的謝意。口試期間蒙張木彬教授、董瑞安教授、鄧宗禹教授、蔡春進教授與張宗良教授對於本論文謬誤及疏漏之處提出指正與建議，在此致上萬分謝意。

本研究論文期間，受到許多人的關心、鼓勵及實驗的幫忙。感謝鄧宗禹教授及宗良學長對於實驗、研究上的指導與鼓勵；工研院簡博士及姿名姐實驗上的幫忙；家欣、育旨、育豪、映棠、政彰、小元等學長於研究經驗的傳承與關懷；雅葳、惠綺，小德學弟與空氣資源管理實驗室一起生活過的同仁；從碩士班以來的同儕王董、聖傑，壘球隊的隊友及一起走過三個週末的伙伴們，與你們度過的歲月是我一輩子也難忘的，在此致上最深的謝意。

特別感謝在我求學期間，台中大同扶輪社先進們的推薦，讓我成為中華扶輪教育基金會 2004 年度博士班獎學生，你們奉獻的精神是值得我一輩子效法的。今日的學位的完成，尤其要感謝父母多年來的鼓勵與支持，讓我一路走到今天。感謝昭政在日常起居上無微不至的照顧、鼓勵與支持，讓我能保持健康的身體，心無旁騖專致於研究，這段求學時間雖然繁忙我依然覺得很幸福。

# CONTENTS

<b>CHAPTER ONE INTRODUCTION .....</b>	<b>1</b>
1.1. MOTIVATION .....	1
1.2. OBJECTIVES .....	2
<b>CHAPTER TWO LITERATURE REVIEW .....</b>	<b>3</b>
2.1. TiO <sub>2</sub> PHOTOCATALYSTS .....	3
2.1.1. Basic concept of TiO <sub>2</sub> .....	3
2.1.2. Application of TiO <sub>2</sub> photocatalyst.....	5
2.2. RECENT DEVELOPMENT OF N-DOPED TiO <sub>2</sub> .....	10
2.2.1. Nitrogen doping methods .....	11
2.2.2. The properties of N-doped TiO <sub>2</sub> .....	12
2.2.3. N-doping status .....	14
2.3. PRODUCTION OF TiO <sub>2</sub> PARTICLES BY GAS PHASE METHODS .....	21
2.3.1. Nucleation controlled synthesis .....	22
2.3.2. Coagulation controlled synthesis.....	23
2.3.3. Condensation controlled synthesis.....	24
2.3.4. Dielectric barrier discharge .....	25
<b>CHAPTER THREE EXPERIMENTAL METHODS.....</b>	<b>30</b>
3.1. PREPARATION OF THE N-DOPED TiO <sub>2</sub> PHOTOCATALYST.....	30
3.1.1. Preparing N-doped TiO <sub>2</sub> particles under different process parameters.....	30
3.1.2. Preparation of different types of N-doping status of TiO <sub>2</sub> photocatalysts.....	31
3.2. CHARACTERIZATION OF N-DOPED TiO <sub>2</sub> PHOTOCATALYST.....	35
3.2.1. The morphology, size, crystal phase and absorption spectra of N-doped TiO <sub>2</sub> particles.....	35
3.2.2. The N-doping status of the N-doped TiO <sub>2</sub> particles .....	36
3.3. PHOTOCATALYTIC DECOMPOSITION OF VOCs AND NO <sub>x</sub> BY TiO <sub>2</sub> PHOTOCATALYST .....	37
3.3.1. Photocatalytic degradation of VOCs in a batch reactor .....	37
3.3.2. Photocatalytic degradation of VOCs in a continuous flow reactor.....	38
3.3.3. Photocatalytic degradation of NO <sub>x</sub> in a continuous flow reactor.....	39
<b>CHAPTER FOUR RESULTS AND DISCUSSION .....</b>	<b>43</b>
4.1. PREPARATION OF N-DOPED TiO <sub>2</sub> PHOTOCATALYST BY APPENS PROCESS....	43
4.1.1. The feasibility of non-thermal plasma to generate nanosize TiO <sub>2</sub> .....	43
4.1.2. Characterization of the N-doped TiO <sub>2</sub> photocatalyst .....	44

4.1.3. Comparison of the APPENS process with other plasma processes.....	45
4.1.4. Summary.....	48
4.2. PHOTOCATALYSIS STUDY OF N-DOPED TiO <sub>2</sub> .....	54
4.2.1. Photocatalytic activity of N-doped TiO <sub>2</sub> in a batch reactor .....	54
4.2.2. Photocatalytic removals of NO by N-doped TiO <sub>2</sub> under UV and visible light irradiation .....	56
4.2.3. Comparison of N-doped TiO <sub>2</sub> photocatalysis with commercial photocatalysts .....	57
4.2.4. Summary.....	59
4.3. EFFECT OF N-DOPING STATUS ON PHOTOCATALYTIC ACTIVITY OF TiO <sub>2</sub> .....	70
4.3.1. IPA Conversion .....	70
4.3.2. Crystallite and particle sizes .....	71
4.3.3. Crystal phase.....	72
4.3.4. UV-visible spectra .....	72
4.3.5. Core level binding energy .....	73
4.3.6. N-doped status of the TiO <sub>2</sub> photocatalyst .....	74
4.3.7. Summary.....	77
4.4. EFFECT OF PROCESS PARAMETERS IN CRYSTALLITE AND PARTICLE SIZE ..	87
4.4.1. Effect of applied voltage .....	87
4.4.2. Effect of electric frequency .....	89
4.4.3. Effect of precursor molar ratio .....	90
4.4.4. Long term stability .....	93
4.4.5. Comparison of APPENS generator with commercial aerosol generators .....	93
4.4.6. Summary.....	94
<b>CHAPTER FIVE CONCLUSIONS AND RECOMMENDATION.....</b>	<b>105</b>
5.1. CONCLUSIONS.....	105
5.2. RECOMMENDATION .....	106

## LIST OF TABLES

Table 2.1 Summarized Applications of photocatalysis for literatures.....	7
Table 2.2 Synthetic methods for N-doping TiO <sub>2</sub> summarized from literatures.....	17
Table 2.3 Literature data on the core level binding energies of Ti 2p, N 1s and O 1s from XPS. ....	18
Table 2.4 Homogeneous chemical reactions in plasma reactor .....	27
Table 3.1 List of parameters for producing different TiO <sub>2</sub> particles .....	33
Table 3.2 Plasma and annealing gas compositions for synthesizing different TiO <sub>2</sub> based photocatalysts.....	33
Table 4.1 The operation parameters and the product properties of the APPENS process and other plasma processes for producing N-doped TiO <sub>2</sub> photocatalysts. ....	49
Table 4.2 Crystallite sizes of SYN1~SYN4 photocatalytic particles. ....	79
Table 4.3 Plasma and annealing gas compositions and different N-doped status of TiO <sub>2</sub> photocatalysts.....	79
Table 4.4 Crystallite size of TiO <sub>2</sub> particles generated via different TTIP/H <sub>2</sub> O precursor molar ratios. ....	96
Table 4.5 Comparison of the APPENS generator with commercial aerosol generators.....	97



## LIST OF FIGURES

Figure 2.1 Structures of rutile and anatase TiO <sub>2</sub> .....	8
Figure 2.2 Mechanistic principles for photocatalytic degradation of pollutants and the charge carrier recombination of TiO <sub>2</sub> . ....	9
Figure 2.3 Electronic structure of substituted metal anion and anion TiO <sub>2</sub> photocatalysts.....	19
Figure 2.4 Electronic structures of (a) substituted N-doping TiO <sub>2</sub> and (b) interstitial N-doping TiO <sub>2</sub> . ....	19
Figure 2.5 Band structures of pure and N-doping TiO <sub>2</sub> in anatase and rutile, respectively. ....	20
Figure 2.6 Schematic of gas-to-particle formation process .....	28
Figure 2.7 Effect of characteristic times .....	29
Figure 2.8 Condensation mechanism of particle growth .....	29
Figure 3.1 Schematic diagram of APPENS reactor for producing TiO <sub>2</sub> nanoparticles. ....	34
Figure 3.2 Schematics of the (a) batch type and (b) continuous flow photocatalytic reactors for VOCs removal.....	41
Figure 3.3 The light spectra of the visible light source used in this study. The five major peaks were observed at 435, 488, 545, 587 and 611 nm. ....	42
Figure 3.4 Continuous flow reactor for photocatalytic removal of NO.....	42
Figure 4.1(a) SEM images of titania based particles formed without atmospheric pressure plasma. (b)&(c) SEM & TEM images of titania based particles formed with applying atmospheric pressure plasma, the particles were with size ranging from 20 to 40 nm....	50
Figure 4.2 XRPD patterns of the Titania-based nanoparticle. ....	51
Figure 4.3 XPS spectra of Ti 2p and N 1s that show evidence of nitrogen doping into the TiO <sub>2</sub> photocatalyst. ....	52
Figure 4.4 SEM image of the film thickness of N-doped TiO <sub>2</sub> deposited on a glass substrate via a plate type APPENS reactor. The electric field strength was 19.2 kV/cm and the	

deposition time was 2 hrs.....	53
Figure 4.5a The decomposition of IPA and the formation of acetone in a batch photocatalytic reactor under UV light (10 W, peak at 364.2 nm). Error bars indicated the error range of repeated experimental data.....	61
Figure 4.5b The decomposition of IPA and the formation of acetone in a batch photocatalytic reactor under visible light (10 W, peaks at 435, 488, 545, 587 and 611 nm). Error bars indicated the error range of repeated experimental data. ....	62
Figure 4.6 The removal efficiency of toluene as a function of time in a batch photocatalytic reactor under UV (10 W, peak at 364.2 nm) and visible light (10 W, peaks at 435, 488, 545, 587 and 611 nm) sources. Error bars indicated the error range of repeated experimental data. ....	63
Figure 4.7 Concentration variation of NO and NO <sub>2</sub> by photo-catalytic reaction under visible light irradiation. The inlet concentrations of NO and NO <sub>2</sub> was 16.7 ppm and 1.1 ppm, respectively. The carrier gas composition was 20%N <sub>2</sub> +80% O <sub>2</sub> . ....	64
Figure 4.8 Concentration variations of NO and NO <sub>2</sub> by photo-catalytic reaction under UV light irradiation. The inlet concentrations of NO and NO <sub>2</sub> was 17.4 ppm and 0.9 ppm, respectively. The carrier gas composition was 20%N <sub>2</sub> +80% O <sub>2</sub> . ....	65
Figure 4.9 Concentration variations of NO and NO <sub>2</sub> by photo-catalytic reaction under UV light irradiation. The inlet concentrations of NO and NO <sub>2</sub> was 10 ppm and 0.9 ppm, respectively. The carrier gas composition was 20%N <sub>2</sub> +80% O <sub>2</sub> . ....	66
Figure 4.10 Removal rates of NO and NO <sub>x</sub> at different inlet NO concentrations under UV light irradiation .....	67
Figure. 4.11 Comparison of the toluene decomposition between P25, ST01 and the N-doped TiO <sub>2</sub> (TiO <sub>2-x</sub> N <sub>x</sub> ) photocatalysts tested in a continuous flow reactor under visible light (10W) illumination. The residence time in the reactor was 2.35 minutes.....	68
Figure 4.12 Kubelka-Munk absorption spectra of the commercial photocatalysts (P25 and ST01) and the N-doped TiO <sub>2</sub> (TiO <sub>2-x</sub> N <sub>x</sub> ) photocatalyst prepared in this study. ....	69
Figure 4.13 The IPA conversion under visible light source (435, 488, 545, 587 and 611 nm, 10 W) at 45°C with a batch type photocatalytic reactor. All error bars of each data were determined form the repeated experimental data. ....	80

Figure 4.14 The IPA conversion under UV light source (364.5 nm, 10 W) at 45°C with a batch type photocatalytic reactor. All error bars of each data were determined from the repeated experimental data. ....	81
Figure 4.15 SEM photo images of particles produced via (a). SYN1, (b) SYN2, (c). SYN3 and (d). SYN4.....	82
Figure 4.16 The XRPD patterns of photocatalytic particles synthesized in this study.....	83
Figure 4.17 The Kubelka-Munk absorption spectra of N-doped photocatalysts synthesized in this study.....	84
Figure 4.18 The XPS patterns of O 1s, Ti 2p and N 1s spectra for photocatalytic particles produced in this study. ....	85
Figure 4.19 The nitrogen doping status for SYN1~SYN4 synthesized photocatalysts based on cross comparison of N 1s and O 1s binding energies. ....	86
Figure 4.20 SEM images of TiO <sub>2</sub> particles collected in the reactor at different applied voltages. (a) No applied voltage, (b) 6.48 kV, (c) 8.58 kV and (d) 9.60 kV. The frequency was 60 Hz, the TTIP/H <sub>2</sub> O precursors molar ratio was 11.9 as TTIP bubbled at 150°C. The scale bar in the SEM photo is 1 μm. ....	98
Figure 4.21 Particle size distributions measured by SMPS after dilution ratio of 1. The operation condition was the same as that of Figure 4.20. Step-lines are SMPS measured data obtained at different applied voltages, and dash-lines are their lognormal fittings. ....	99
Figure 4.22 Particle size distributions measured by SMPS after dilution ratio of 12 under different electric frequencies. Also shown are SEM images of the reactor-deposited particles. The applied voltage was 10.20 kV, the TTIP/H <sub>2</sub> O precursor molar ratio was 11.9 as TTIP bubbled at 150°C.....	100
Figure 4.23 The XRPD patterns of generated particles synthesized in this study. The operation condition was the same as that of Table 1 with TTIP/H <sub>2</sub> O precursor molar ratio (MR) from 0.4 to 76.1 and TTIP bubbling temperature of 150 or 200°C.....	101
Figure 4.24 Effect of precursor molar ratio on the size distributions of particles collected in the reactor and measured by SEM images. The applied voltage was 9.60 kV and the TTIP bubbling temperatures were at 150 or 200°C.....	102
Figure 4.25 TEM images (scale bar = 20 nm) of particles collected in the reactor as obtained at two	

different TTIP/H<sub>2</sub>O precursor ratios of 1.1 and 76.1, respectively. The applied voltage was 9.60 kV and the TTIP bubbling temperatures were at 150 and 200°C, respectively.

..... 103

Figure 4.26 Stability of geometric mean particle diameter ( $D_{p_g}$ ) and geometric standard deviation ( $\sigma_g$ ) measured by SMPS during one hour of operation time. The frequency was 60 Hz, the TTIP/H<sub>2</sub>O molar ratio was 0.7 as TTIP bubbled at 150°C and the applied voltage was 9.60 kV..... 104



## ABBREVIATIONS

<b>AC</b>	Alternating Current
<b>APPENS</b>	Atmospheric Pressure Plasma Enhanced Nanoparticle Synthesis
<b>BET</b>	Brunauer-Emmett-Teller
<b>DBD</b>	Dielectric Barrier Discharge
<b>DSSC</b>	Dye-Sensitized Solar Cells
<b>FID</b>	Flame Ionization Detector
<b>FWHM</b>	Full Width at Half Maximum
<b>GC</b>	Gas Chromatography
<b>IBAD</b>	Ion-Beam-Assisted Deposition
<b>IPA</b>	Isopropanol
<b>PECVD</b>	Plasma-Enhanced Chemical Vapor Deposition
<b>RF</b>	Radio Frequency
<b>SEM</b>	Scanning Electron Microscope
<b>SMPS</b>	Scanning Mobility Particle Sizer
<b>TEM</b>	Transmission Electron Microscope
<b>TMC</b>	Total Mass Concentration
<b>TTIP</b>	Titanium Tetraisopropoxide
<b>UV</b>	Ultraviolet
<b>XPS</b>	X-Ray Photoelectron Spectroscopy
<b>XRPD</b>	X-Ray Powder Diffractometer



# CHAPTER ONE INTRODUCTION

## 1.1. MOTIVATION

The environmental problems related to the remediation of hazardous wastes, contaminated groundwaters, the control of toxic air contaminants, and the energy resources have been the global concerned topics in recent years. Therefore development of environmentally friendly technology and energy resources are demanded. For these purposes titanium dioxide ( $\text{TiO}_2$ ) as a photo-catalyst has been extensively studied due to their stability and wide applications in environmental pollution control and solar energy resources (Hoffmann et al., 1995; Fujishima et al., 2000; Grätzel, 2001; Kitano et al., 2007; Wang et al., 2007).



However, the pure  $\text{TiO}_2$  photocatalysts can only be effectively utilized under ultraviolet (UV;  $\lambda < 365$  nm) light source. Thus the development of visible light photocatalysts has attracted wide attention in order to enhance the utilization efficiency of solar energy. The modified  $\text{TiO}_2$  that utilizes visible light source can be achieved by doping various elements such as metals, F, S, and N (Asahi et al., 2001; Wang et al., 2001; Umebayashi et al., 2003). Among the viable non-metal doping elements (C, N, F, P and S) for  $\text{TiO}_2$ , the substitutional doping of N has been recognized to be one of the most effective means for producing visible light irradiation effect (Asahi et al., 2001).

Most studies on N-doped  $\text{TiO}_2$  commonly utilized the X-ray photoelectron spectroscopy (XPS) for the characterization of N atoms presented in  $\text{TiO}_2$ . However, the N-doping status was frequently

reported as  $\text{TiO}_{2-x}\text{N}_x$  without specifying the actual N-doping status of the N-impurity. In addition to the wide application of  $\text{TiO}_2$  nanoparticles, their implications on human health and biological impact are also of concerns. Thus the generation of size controlled nanoparticles for both implication and application studies have always been an important research.

## 1.2. OBJECTIVES

The objectives of this study are listed in the following:

1. To investigate the potential of a novel process of employing non-thermal plasma process for producing  $\text{TiO}_2$  and N-doped  $\text{TiO}_2$ .
2. To investigate the photocatalytic performance of VOCs (toluene and isopropanol; IPA) and nitric oxides ( $\text{NO}_x$ ) by the N-doped  $\text{TiO}_2$  under illumination of UV and visible light sources.
3. To investigate the effects of plasma and annealing gas compositions on the species of Ti, N, O and on the photo-activities of photocatalysts.
4. To investigate the possibility of the APPENS process as a chemical-approached aerosol generator for the continuous generation of  $\text{TiO}_2$  nanoparticles (<100 nm).

## CHAPTER TWO LITERATURE REVIEW

### 2.1. TiO<sub>2</sub> PHOTOCATALYSTS

Titanium dioxide has received enormous studies due to their stability and wide applications in decomposition of environmental pollutants and materials for solar energy resources (Fujishima et al., 2000). A brief synopsis will be introduced in this section for the basic properties and application of TiO<sub>2</sub> that related to this study.

#### 2.1.1. Basic concept of TiO<sub>2</sub>

The three major structures of TiO<sub>2</sub> are rutile, anatase and brookite. However, only the rutile and anatase forms of TiO<sub>2</sub> play the important role in the application of environmental energy, thus these two types were described in this study (Diebold, 2003). Figure 2.1 shows the unit cell structures of the rutile and anatase forms of TiO<sub>2</sub>. The Ti atom is surrounded by six O atoms in both of structures. These two crystal structures are in distorted octahedron class. A slight orthorhombic distortion structure is occurred in rutile, while the distortion of cubic lattice is significant in anatase.

The distances of Ti-Ti in anatase are larger but the Ti-O distances are shorter than those in rutile. Thus, these differences in lattice structures lead to the different mass densities and electronic band structures between the two forms of TiO<sub>2</sub> (Chen and Mao, 2007; Diebold, 2003; Thompson and Yates, 2007), and the photo-catalytic activity of anatase TiO<sub>2</sub> shows higher than that of the rutile TiO<sub>2</sub> (Ramis et al., 1987).



The mechanistic principles for photocatalytic degradation of pollutants are shown in Figure 2.2.

The electron-hole ( $e^-$ - $h^+$ ) pair generated by light irradiation is trapped at surface, and the hydroxyl radicals ( $\bullet$ OH) were formed from  $h^+$  and  $OH^-$ . The  $\bullet$ OH is a highly reactive species that can oxidize pollutants adsorbed on the catalyst surface. The mechanisms of reaction are shown as following

(Cao et al., 1999):



The concentration of charge carriers under light irradiation excitation in any semiconductor is reduced by the inherent recombination process of electron-hole pairs. Thompson and Yates (2007) indicated that this action can be explained by the Shockley-Read-Hall model in  $TiO_2$ . The active sites for electron or hole trapping may vary and are usually described as defect states within the crystal due to interstitial atoms, defect states, vacancy, or grain boundaries. In the Shockley-Read-Hall mechanism, as schematically depicted in Figure 2.2, four transition processes may occur: (1) electron capture; (2) electron emission; (3) hole capture; or (4) hole emission (Thompson and Yates, 2007). The photocatalytic activity can be enhanced by avoiding the

electron-hole recombination by the defect on the TiO<sub>2</sub> surface (Bore, 1990; Alberici and Jardim, 1997; Brillas et al., 1998). Nakamura et al. (2000) indicated that the formation of the oxygen vacancy state located between the valence and conduction bands can be serve as an electron trapping center in plasma-treated TiO<sub>2</sub>. The plasma-treated TiO<sub>2</sub> shows a good efficiency of the photocatalytic oxidation of NO to NO<sub>3</sub><sup>-</sup> under irradiation of visible light.

### *2.1.2. Application of TiO<sub>2</sub> photocatalyst*

The TiO<sub>2</sub> nanoparticles have attracted many studies due to their potential applications including photocatalysis, photovoltaic, water splitting and gas sensing (Hoffmann et al., 1995; Fujishima et al., 2000; Grätzel, 2001; Nakada et al., 2002; Chen and Mao, 2007; Kitano et al., 2007). Table 2.1 shows the applications of TiO<sub>2</sub> photocatalysts summarized from literatures (Fujishima et al., 2000; Grätzel, 2001; Chen and Mao, 2007; Ni et al., 2007). TiO<sub>2</sub> photocatalysts have been applied to various fields such as photocatalytic destruction of various environmental pollutants (air and water), photocatalytic sterilization, photocatalytic cancer treatment, antifogging, self-cleaning, solar cell materials, hydrogen fuel cells, display and gas sensor (Fujishima et al., 2000; Grätzel, 2001; Chen and Mao, 2007; Ni et al., 2007).

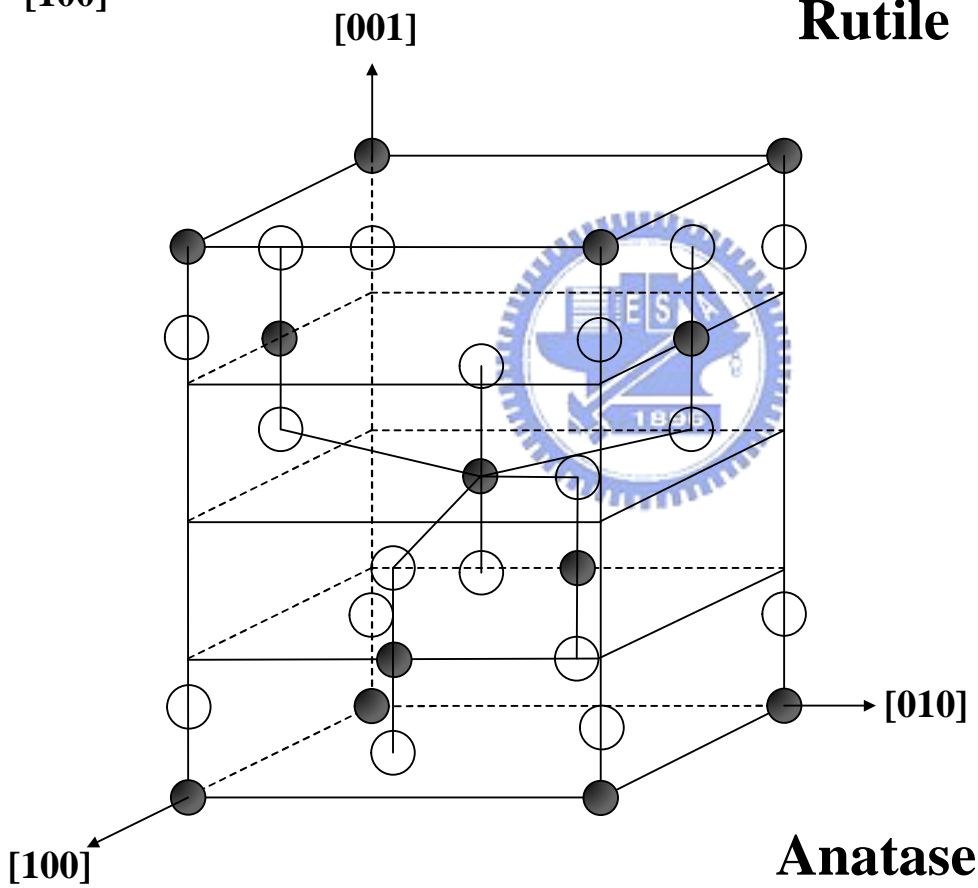
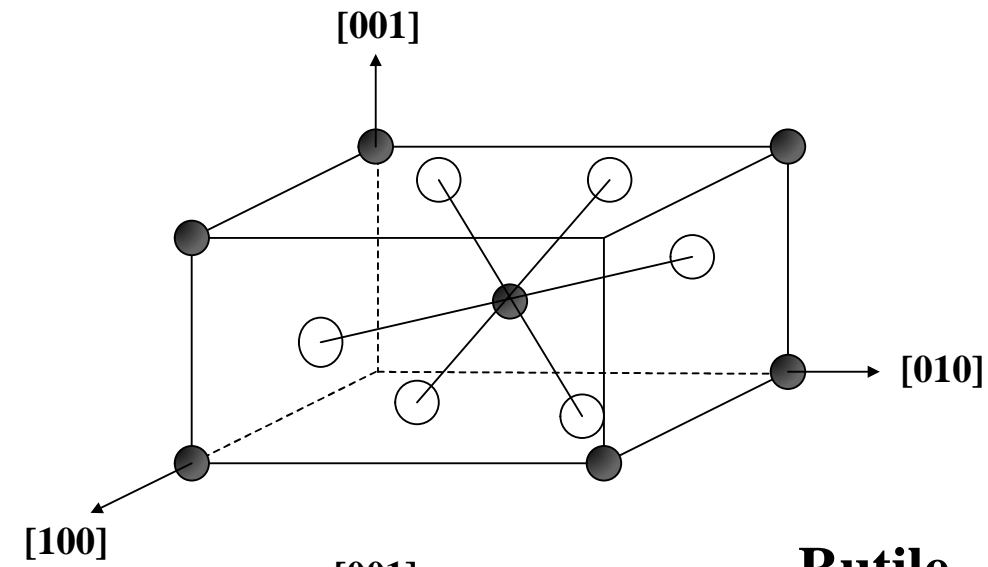
TiO<sub>2</sub> nanomaterials can be utilized for antifogging and self-cleaning materials on various glass products, i.e., mirrors and eyeglasses due to its superhydrophobic surfaces (Fujishima et al., 2000). TiO<sub>2</sub> has been used for photodecomposition of pollutants, anti bacteria and kill tumor cells in cancer treatment (Fujishima et al., 2000; Hoffmann et al., 1995; Kitano et al., 2007).

The Dye-Sensitized Solar Cells (DSSC) technology has been proposed that the efficiency of solar to current conversion is reached about 10.6% (Grätzel et al., 2001). Water splitting and hydrogen production have attracted many studies due to its feature of clean, suitable and renewable. In addition, TiO<sub>2</sub> nanomaterial has been studied as sensors for various gases, and the sensors have been approached for H<sub>2</sub>, O<sub>2</sub> and CO gas sensing (Fujishima et al., 2000; Grätzel, 2001; Chen and Mao, 2007; Ni et al., 2007).



**Table 2.1 Summarized Applications of photocatalysis for literatures (Fujishima et al., 2000; Grätzel, 2001; Chen and Mao, 2007; Ni et al., 2007).**

<b>Property</b>	<b>Category</b>	<b>Application</b>
Self-cleaning	Materials for lamps, roads, residential and office buildings	Tunnel wall, soundproofed wall, traffic signs and reflectors, plastic surfaces, building stone and lamp covers or coatings
Pollutants destruction	Air cleaning	Room air cleaner, photocatalyst-equipped air conditioners, the materials for roadways and tunnel walls.
	Water purification	River water, ground water, lakes, water-storage tanks and industrial wastewater
Antitumor activity	Cancer therapy	Endoscopic-like instruments
Self-sterilizing	Anti- bacteria	Tiles to cover the floor and walls of operating rooms, silicone rubber for medical catheters and hospital garments and public rest rooms, bed room
Photovoltaic	Energy sources	Solar cell, Dye-Sensitized Solar Cells (DSSC)
Photocatalytic water splitting	Energy sources	Hydrogen fuel cells
Electrochromic	Electrochromic devices	Electrochromic windows and display
Sensing	Gas sensors	Gas sensors for H <sub>2</sub> , O <sub>2</sub> , CO gases



○ O atom  
● Ti atom

Figure 2.1 Structures of rutile and anatase  $\text{TiO}_2$ .

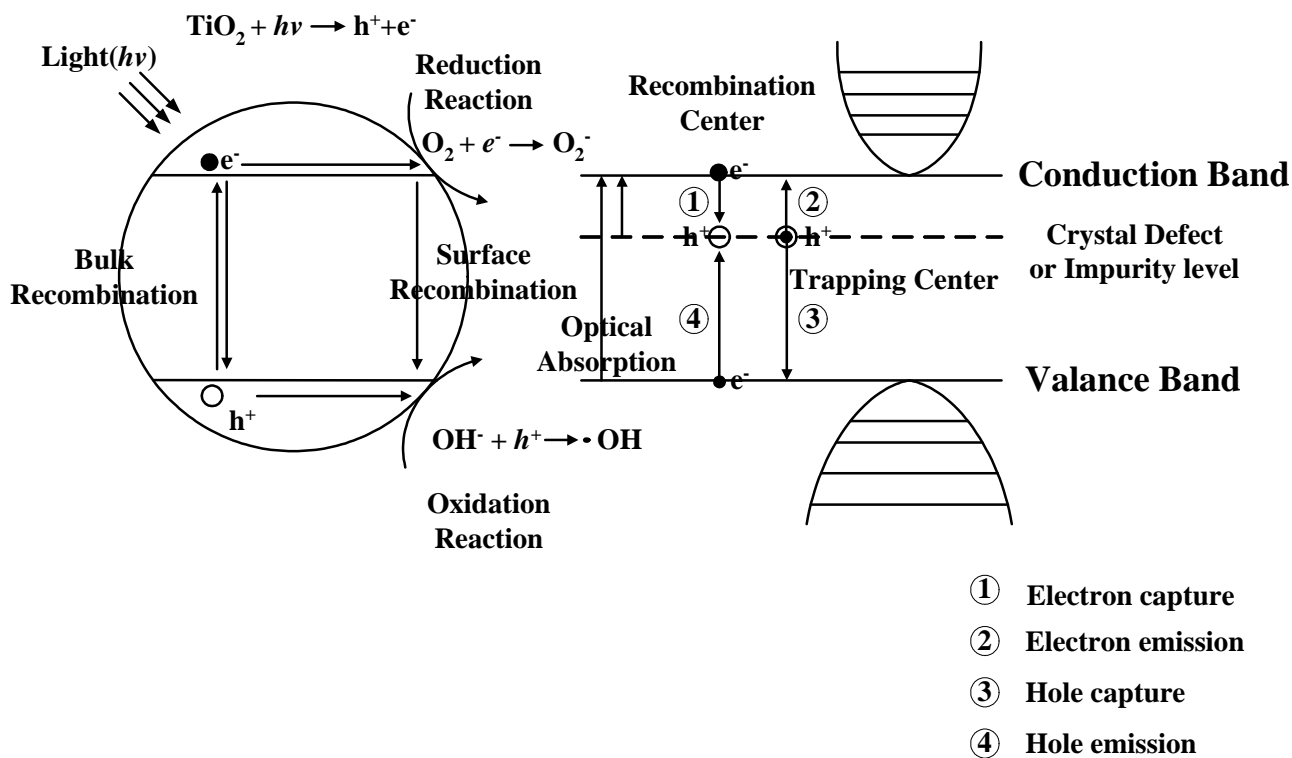
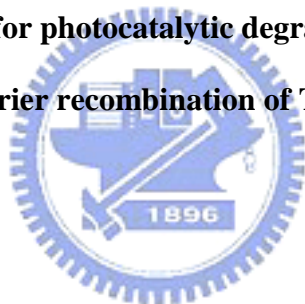
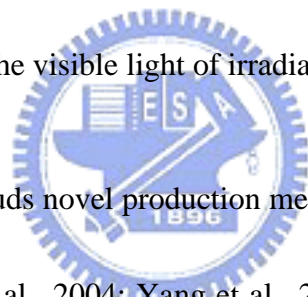


Figure 2.2 Mechanistic principles for photocatalytic degradation of pollutants and the charge carrier recombination of  $\text{TiO}_2$ .



## 2.2. RECENT DEVELOPMENT OF N-DOPED TiO<sub>2</sub>

The N-doped TiO<sub>2</sub> has received enormous attention from researches of photocatalytic field since ever Asahi et al. (2001) have reported that N-doping TiO<sub>2</sub> could initiate photo activation by visible light sources, thereby improving methyl blue destruction efficiency and potentially expanding its fields of application. Asahi et al. (2001) indicated that among the viable non-metal doping elements (C, N, F, P and S) for TiO<sub>2</sub>, the substitutional doping of nitrogen has been recognized to be one of the most effective means for producing visible light irradiation effect. This TiO<sub>2-x</sub>N<sub>x</sub> film absorbed wavelength more than 500 nm, and the TiO<sub>2-x</sub>N<sub>x</sub> nano-particles are superior to that of the TiO<sub>2</sub> nano-particles in the visible light of irradiation.



Studies on the N-doping TiO<sub>2</sub> includes novel production methods (Asahi et al., 2001; György et al., 2003; Miao et al., 2004; Sakatani et al., 2004; Yang et al., 2004a; Yang et al., 2004b; Chen et al., 2005; Livraghi et al., 2005; Nosaka et al., 2005; Suda et al., 2005; Wu et al., 2005; Yin et al., 2005), effect of N-dopant concentration on photocatalytic activity (Irie et al., 2003), crystal phase of N-doped TiO<sub>2</sub> (Di Valentin et al., 2004), optical properties (Wu et al., 2005) and structure of N-doped TiO<sub>2</sub> (Di Valentin et al., 2005; Livraghi et al., 2006). Most of the studies on N-doped TiO<sub>2</sub> commonly utilized XPS for the characterization of N atoms presented in TiO<sub>2</sub>, but the N-doping in TiO<sub>2</sub> was frequently reported as TiO<sub>2-x</sub>N<sub>x</sub> without specifying the actual N-doping status of the N-impurity. This section intends to review literatures that related to this study.

### 2.2.1. Nitrogen doping methods

Up to the present, many methods have been documented to successfully prepare N-doped TiO<sub>2</sub> films or particles. Table 2.2 lists the synthetic methods for N-doping TiO<sub>2</sub>, which include direct surface treatment of TiO<sub>2</sub> target by sputtering (Asahi et al., 2001) or plasma (Miao et al., 2004), using TiO<sub>2</sub> precursors to produce TiO<sub>2</sub> photocatalysts via the Plasma Enhanced Chemical Vapor Deposition (PECVD) process (Maeda and Watanabe, 2006), the pulse laser deposition (Suda et al., 2005), the ion-assisted electron beam evaporation method (Yang et al., 2004) and the aqueous phase reactions such as sol-gel method (Chen et al., 2005; Nosaka et al., 2005; Sato et al., 2005; Yin et al., 2005; Livraghi et al., 2006)



One can see from Table 2.2 that the materials for synthesizing N-doped TiO<sub>2</sub> were bare TiO<sub>2</sub> or titanium precursors, while the nitrogen sources were N<sub>2</sub>, NH<sub>3</sub>, NH<sub>4</sub>OH and NH<sub>4</sub>Cl. The mechanism of N-doping could be either in thermal diffusion, excited N ion implanted or chemical reaction. Thermal diffusion and N ion implanted was in feature of utilizing the bare TiO<sub>2</sub> and then doped the nitrogen by heating or ion sputtering. On the other hand, chemical reaction is usually observed in wet method and the reaction occurs between the TiO<sub>2</sub> or titanium precursor and nitrogen sources of NH<sub>3</sub>, NH<sub>4</sub>OH or NH<sub>4</sub>Cl at high temperature.

In the N-doping process, the nitrogen source such as NH<sub>3</sub>, NH<sub>4</sub>OH and NH<sub>4</sub>Cl may be converted to harmful byproducts. But N-doping is difficult to be approached by simple heating of N<sub>2</sub> gas only. On the contrary, the process of plasma, sputtering and ion beam can implanted the N



ion into TiO<sub>2</sub> photocatalyst via utilizing the N<sub>2</sub> gas directly. However utilizing bare TiO<sub>2</sub> during the process leads to confinement of the physical and chemical properties of N-doped TiO<sub>2</sub>.

The plasma enhanced chemical process (PECVD) can synthesize the N-doped TiO<sub>2</sub> directly from titanium precursor with N<sub>2</sub> gas (Battiston et al., 2000; Maeda and Watanabe, 2006). It supports sufficient energy for breaking and doping N<sub>2</sub> or NH<sub>3</sub> molecules into the titania precursors. But, most of the plasma processes entail stringent operating environment of low pressures (vacuum) and/or high temperatures.

### 2.2.2. *The properties of N-doped TiO<sub>2</sub>*

Asahi et al. (2001) indicated that the substitutional doping of N was most effective because its *p* state contributes to the band-gap narrowing by mixing with O 2*p* states. They have reported the theoretical calculation of density of state (DOS) from the substituted O atom by C, N, F, P, and S in TiO<sub>2</sub> lattice. The visible light-induced TiO<sub>2</sub> can be achieved by doping with various elements such as metals, F, S, and N (Asahi et al., 2001; Wang et al., 2001; Umebayashi et al., 2003). In recent years, some studies have been focused on the effect of N-dopant concentration (Irie et al., 2003), crystal phase of N-doped TiO<sub>2</sub> (Di Valentin et al., 2004), and the structure of N-doped TiO<sub>2</sub> (Di Valentin et al., 2005; Livraghi et al., 2006) on photocatalytic activity.

The local structure of the metal anion and anion substituted TiO<sub>2</sub> photocatalysts are schematically shown in Figure 2.3. The anions or defects were substituted of the sites O<sup>2-</sup> ions, but

the metal ions were substituted of Ti ions in the lattice position of TiO<sub>2</sub>. Both of them were found to have significant impact on the modification of the electronic structure of TiO<sub>2</sub> for extending the absorption edge to visible light range (Asahi et al., 2001; Wang et al., 2001; Umebayashi et al., 2003; Kitano et al., 2007).

Furthermore, the N-doping (anion) TiO<sub>2</sub> has been considered as two modal, substituted N-doping (Figure 2.4a) and interstitial N-doping (Figure 2.5b) TiO<sub>2</sub> (Di valentin et al., 2005). Di valentin et al. (2004, 2005) and Livraghi et al. (2006) indicated that the electronic transition from localized states to the conduction band instead of a band-to-band transition under visible light irradiation. The localized states of substitutional N-doped anatase TiO<sub>2</sub> were occupied N 2p that slightly above the valence band edge (Figure 2.5a). The NO bond formed localized states noted as  $\pi$  (Figure 2.4b). The highest localized state for the interstitial species is 0.73 eV above the top of the valence band, and is 0.14 eV above it for substitutional species. Both of these two N-doping types were formed localized occupied states between the bands for visible light induced photoactivity.

Di valentin et al. (2004) also indicated that the N-doping has opposite effects on the photoactivity of anatase and rutile forms of TiO<sub>2</sub>, leading to a redshift and a blueshift, respectively (Figure 2.5). They indicated that the doping is accompanied in both cases by the appearance of well localized N 2p states above the O 2p valence band but in rutile the shift of the top of the valence band towards lower energies leads to an increase of the band gap transition. The similar result was also proposed by Diwald et al. (2004a; b) by nitrogen implantation of rutile TiO<sub>2</sub>. In addition, Irie et

al. (2003) indicated that the values of quantum yield decreased as nitrogen dopant increased due to the doping sites serve as recombination centers.

### 2.2.3. N-doping status

The N-doped  $\text{TiO}_2$  has been recognized as one of the most effective means for band-gap narrowing via mixing of 2p state of substituted N with 2p state of O in  $\text{TiO}_2$  lattice (Asahi et al., 2001). Although it is widely accepted (Miao et al., 2004; Nosaka et al., 2005; Suda et al., 2005; Yin et al., 2005; Maeda and Watanabe, 2006; Yin et al., 2006) that the TiN doping in  $\text{TiO}_2$  photocatalyst has a positive effect on the photocatalytic activity under illumination of visible light, there still exist other types of N-doping such as  $\text{-(NO)}$ ,  $\text{-(NO}_2\text{)}$  and  $\text{(O-Ti-N)}$  (Gyorgy et al., 2003; Diwald et al., 2004a; 2004b; Chen and Burda, 2004; Chen et al., 2005; Livraghi et al., 2005; Nosaka et al., 2005; Sato et al., 2005). Nosaka et al. (2005) doped N atoms into commercial  $\text{TiO}_2$  particles in the presence of organic compounds and observed the presence of TiN and  $\text{-(NO)}$  in the photocatalysts. They indicated that both TiN and  $\text{-(NO)}$  doped  $\text{TiO}_2$  contributed to absorption of the visible light. TiN tended to increase the visible light photocatalytic activity, while  $\text{-(NO)}$  doping had a negative effect on visible light photocatalytic activity.

However, Sato et al. (2005) and Yin et al. (2005) prepared the N-doped anatase  $\text{TiO}_2$  powders and obtained  $\text{-(NO)}$  doping as the only status of N-doped  $\text{TiO}_2$ . Their results showed that the presence of  $\text{-(NO)}$  at N 1s binding energy at around 400 eV is an effective N-doping site. Diwald et al. (2004a; b) also showed that the peak observed at 399.6 eV is responsible for the shift of the

photochemical threshold down to  $\sim 2.4$  eV, and this form of nitrogen is most likely located in an interstitial site bound to hydrogen. They also indicated that this form of N-doping disagrees with the conclusion of Asahi et al. (2001). Similar observation was shown by Chen et al. (2004; 2005) that  $\text{TiO}_2$  with oxynitride doping at N 1s binding energy of around 402 eV is an effective photocatalyst for the decomposition of methylene blue.

Table 2.3 lists the binding energies of Ti 2p, N 1s and O 1s obtained from the XPS Handbook as well as reported data on N-doped  $\text{TiO}_2$  photocatalysts or other nitrogen impurities materials (Rodriguez et al., 2000; Jirsak et al., 1999). Although there might have some differences in the values of binding energy of Ti 2p, N 1s and O 1s as detected by different instruments and laboratories, they can still be identified as  $\text{TiO}_2$  and TiN at  $2p_{3/2}$  and  $2p_{1/2}$ , and be grouped into several ranges as N(I)~N(IV) for N 1s and O(I)~O(III) for O 1s.

The Ti 2p binding energies of Ti  $2p_{3/2}$  (455.0~459.5 eV) and Ti  $2p_{1/2}$  (461.0~465.0 eV) were different between  $\text{TiO}_2$  and TiN. As appearance of TiN, the core level binding energy of Ti 2p tended to be lower than that of  $\text{TiO}_2$ . The N 1s spectra with peaks at 395.8~397.8 eV indicated that the N-doping status was TiN, while those of N(II)~N(III) at around 399~403 eV revealed the presence of  $\text{N}_2$  chemisorption or the oxynitride doping such as Ti-N-O, Ti-O-N,  $\text{N}_x\text{-Ti-O}_y$  and O-Ti-N. For N(IV), there exist an additional N-doping status of  $-(\text{NO}_2)$  in  $\text{TiO}_2$  particles. The binding energy of O(I) with peaks at 528.1~530.2 eV showed that the O atom was bound to metals such as Ti, while for O(II)~O(III) the O atom was bound to N or other atoms such as C and H. The

binding energies of Ti 2p, N 1s and O 1s listed in Table 2.3 will be used hereafter as references for cross identification of the status of N-doped TiO<sub>2</sub> particles produced in this study.



**Table 2.2 Synthetic methods for N-doping TiO<sub>2</sub> summarized from literatures**

Doping method	TiO <sub>2</sub> / precursor	Nitrogen source	TiO <sub>2</sub> crystal phase	Author
<b>Thermal diffusion</b>				
heating at 200~1000°C	TiO <sub>2</sub>	NH <sub>3</sub>	-	Mozia et al., 2005
heating at 400~600°C	TiO <sub>2</sub>	NH <sub>4</sub> OH	anatase (400°C) rutile(600°C)	Wang et al., 2006
heating at 550~600°C	TiO <sub>2</sub> (ST01)	NH <sub>3</sub>	anatase	Irie et al., 2003
heating at 597°C	TiO <sub>2</sub>	NH <sub>3</sub>	-	Diwald et al., 2004a
<b>Plasma/sputtering/ion implant</b>				
sputtering + heating 550°C	TiO <sub>2</sub>	N <sub>2</sub>	anatase	Asahi et al., 2001
ion-beam sputtering + heating 697°C	TiO <sub>2</sub>	N <sub>2</sub> gas	anatase	Wu et al., 2005
plasma + heating 400°C	TiO <sub>2</sub> (ST01)	N <sub>2</sub>	anatase	Huang et al., 2007
<b>Wet method</b>				
heated at 400~600°C	TIP	NH <sub>3</sub>	anatase	Joung et al., 2006
heated at 350~550°C	TiO <sub>2</sub>	Urea + Gua-Hcl	anatase + rutile	Nosaka et al., 2005
heating 497°C	TIP	NH <sub>4</sub> Cl	anatase	Livraghi et al., 2006
heating 497°C	TIP	NH <sub>4</sub> Cl	anatase	Di Valentin et al., 2006

**Table 2.3 Literature data on the core level binding energies of Ti 2p, N 1s and O 1s from XPS.  
(Chen et al., 2007)**

Species	Assigned doping status
<b>Ti 2p<sub>3/2</sub></b> 455.0-459.5	TiN (455.2±0.2, 455.6, 455.9±0.2)
	TiN <sub>x</sub> O <sub>y</sub> (455.2)
	TiO <sub>2-x</sub> N <sub>x</sub> (456-459, 459.1)
	Titanium oxynitride (456.5)
	Oxidized TiN (456.8)
	TiO <sub>2</sub> (458.5, 458.8, 458.8±0.34, 459.1)
<b>Ti 2p<sub>1/2</sub></b> 461.0-465.0	TiN <sub>x</sub> O <sub>y</sub> (461)
	Oxidized TiN (462.6)
	TiO <sub>2-x</sub> N <sub>x</sub> (464.4, 463-465)
	TiO <sub>2</sub> (464.34, 464.4, 464.7)
<b>N 1s</b> (I)	TiN <sub>x&gt;1</sub> (395.85)
	TiN (396, 396.1, 396.5, 396.6, 396.7, 397, 397.2±0.5, 397.8)
395.8-397.8	TiN <sub>x</sub> O <sub>y</sub> (397)
<b>N 1s</b> (II)	N-C, N-O, N-N (399.25, 400, 398.8-400.3, 398.9±0.8)
	Molecularly chemisorbed γ-N <sub>2</sub> (399.3, 400, 401.15)
	Nitrogen contaminant (398.8-400.3)
	Ti-N-O (399.5)
	Interstitially dopant N-H(399.6)
398.8-401.2	Ti-O-N (400)
<b>N 1s</b> (III)	O-Ti-N (402)
	Molecularly chemisorbed γ-N <sub>2</sub> (402)
	Oxidized TiN (N <sub>x</sub> -Ti-O <sub>y</sub> ; 402-403.3)
402.0-403.3	NO <sub>x</sub> (402.5)
<b>N 1s</b> (IV)	-NO <sub>2</sub> (404, 404.1±0.2)
403.9-404.3	
<b>O 1s</b> (I)	Metal oxide(529.6±1.5)
	TiO <sub>2</sub> (529.7, 530±0.2, 530.2, 530.5)
528.1-530.2	
<b>O 1s</b> (II)	TiN <sub>x</sub> O <sub>y</sub> (531.0)
	Substoichiometric oxide, oxynitride(531.4), Ti-N-O(532), O-Ti-N(532),
	Adsorbed oxygen(532.2)
531.0-532.4	OH(532.4)
<b>O 1s</b> (III)	-NO <sub>2</sub> (533.2±0.5)
	CO(533.4)
532.7-533.7	

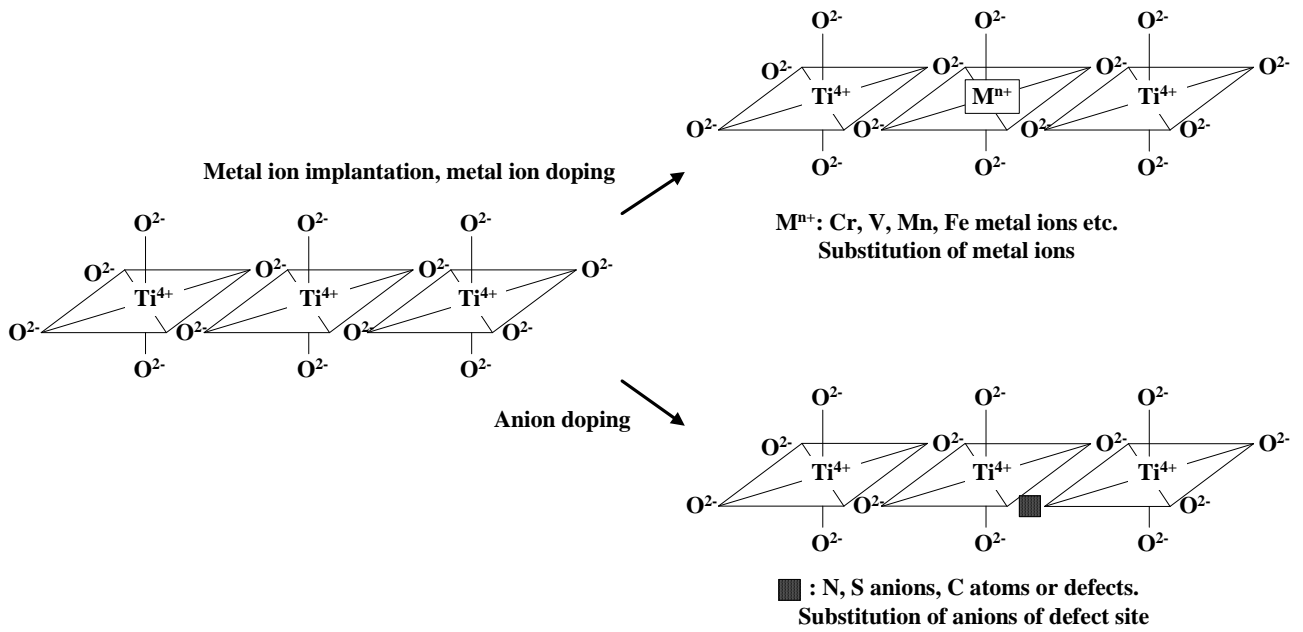


**Figure 2.3 Electronic structure of substituted metal anion and anion TiO<sub>2</sub> photocatalysts.**

(Kitano et al., 2007)

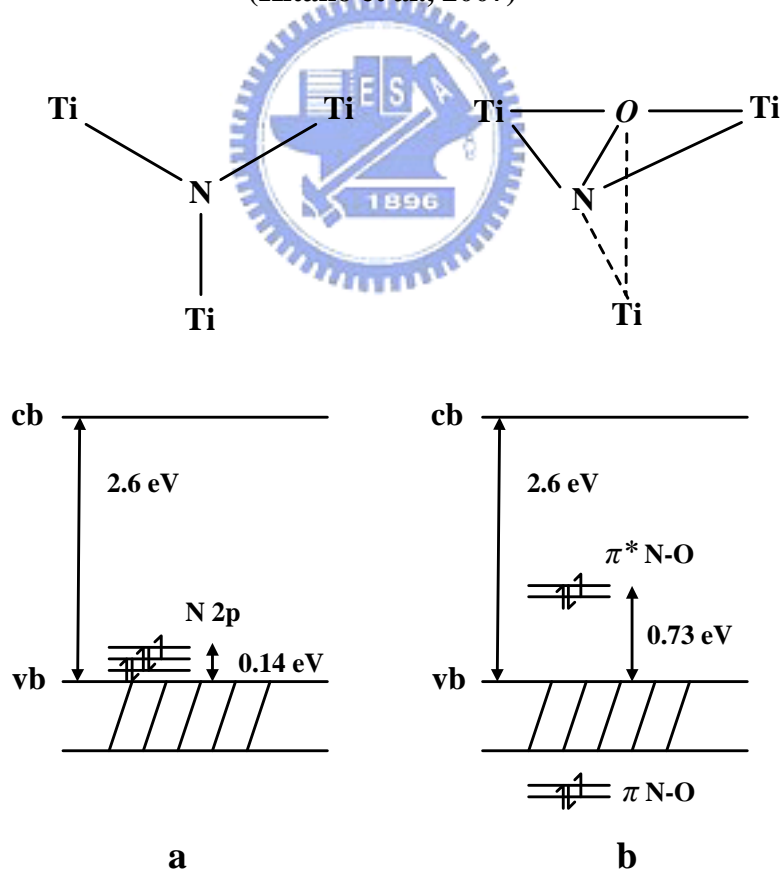


**Figure 2.4 Electronic structures of (a) substituted N-doping TiO<sub>2</sub> and (b) interstitial N-doping TiO<sub>2</sub>. (Di valentin et al., 2005)**



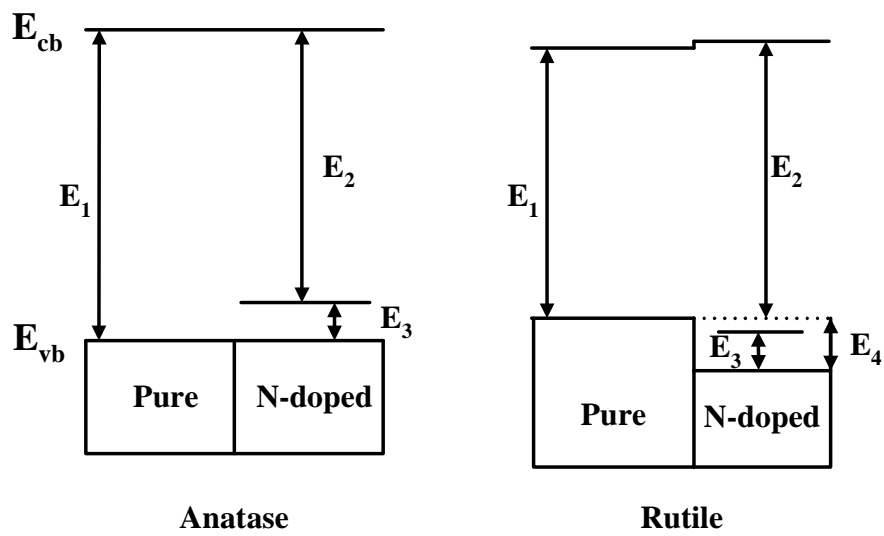


Figure 2.5 Band structures of pure and N-doping  $TiO_2$  in anatase and rutile, respectively. (Di valentin et al., 2004)



### 2.3. PRODUCTION OF TiO<sub>2</sub> PARTICLES BY GAS PHASE METHODS

Production of nanoparticle by gas phase method is superior to that of wet method (sol-gel) in higher purity crystal and continuous generation. Many of the nanoparticles are produced and utilized as an aerosol generator by physical processes where the chemical composition of generated particles is the same as the precursors. For examples, the vibrating orifice (Berglund and Liu, 1973), evaporation-condensation aerosol generator (Veranth et al. 2003; Peinekea et al., 2006), spray (Chein and Lundgren, 1995) or electrospray (Chen et al., 1995) aerosol generator, modified fluidized bed (Prenni et al., 2000), gas-metal arc welding of steels (Zimmer et al. 2002) and the spark discharge particle generator (Evans et al. 2003; Harvath and Gangl, 2003). The species of physically generated particles are subjected to their dissolubility or evaporation properties.

On the contrary, the chemical process in which the chemical composition of generated particles is different from the precursors is widely applied for the production of semiconductor materials, e.g. flame synthesis (Pratsinis et al., 1996; Yang et al., 1996; Arabi-Katbi et al., 2001; Wang et al., 2001; Almquist and Biswas, 2002; Lee and Choi, 2002; Tsantilis et al., 2002;), chemical vapor deposition (Park et al., 2001; Nakaso et al., 2003b; Kim et al., 2005), thermo decomposition furnace aerosol reactor (Okuyama et al., 1986; Nakaso et al., 2001; Spicer et al., 2002; Tsantilis and Pratsinis, 2004a; Cho and Biswas, 2006) and plasma process (Kim et al., 2003).

Figure 2.6 sketches the gas-to-particle formation mechanisms including nucleation, condensation, coagulation and coalescence (Kuster and Pratsinis, 1995; Friedlander, 2000). As the precursor

vapors were nucleating to form primary particles, the primary particles were then grown to secondary particles from the mechanism condensation, coagulation and the coalescence.

During the last decade, there has been a rapid growth in controlling size of particle due to the development of nanotechnology. It has been the object of increasing number of studies not only on producing the nano-sized particles, but also on narrowing the particle size distribution. In this section, literatures that related to this study were reviewed and summarized on the factors or mechanisms in controlling the particle size and the size distribution.

### *2.3.1. Nucleation controlled synthesis*

The nucleation while occurred without another foreign phase is called homogeneous nucleation and is commonly appeared during materials manufacture processes via gas phase reaction. On the contrary, heterogeneous nucleation was occurred in the presence of nuclei particles and is often appeared in atmospheric environment (Kodas and Hampden-Smith, 1999). In the precursor vapor phase, some atoms or molecules can be formed as clusters by random collisions, and the clusters would be grown or dispersed in the vapor phase (Kodas and Hampden-Smith, 1999; Friedlander, 2000).

For a supersaturated vapor, the sufficiently large clusters were reached to thermodynamically stable state and then formed particles. In this state, the partial pressure around the particles was larger than the vapor pressure on the curved surface of particle. This phenomena is called Kelvin effect and in a relation as:

$$d_p = \frac{4\sigma v_1}{k_B T \ln S} \quad (7)$$

The  $\sigma$  (ergs/cm<sup>2</sup>) is surface tension,  $v_1$  (cm<sup>3</sup>) is molecular volume,  $k_B$  is Boltzmann's constant,  $T$  (K) is temperature, and  $S$  is saturation ratio. The  $S$  is defined as  $p_1/p_e$ ,  $p_1$  is the partial pressure of species 1 and  $p_e$  is equilibrium vapor pressure over a flat surface. Therefore, the primary particle size can be controlled by the concentration of monomer or the temperature of process. In this mode, the primary particle size increased with increasing concentration of precursor (Kim et al., 2005; Yin and Alivisatos, 2005).

### 2.3.2. Coagulation controlled synthesis

The mode of coagulation controlled synthesis is commonly occurred at high concentration of particles and accompanied the collision and coalescence for particles growth. The hardness and fractal dimensions of agglomerates are depended on the conditions of process (Friedlander, 2000; Kodas and Hampden-Smith, 1999). Figure 2.7 shows two modes of particles growth by collision and coalescence. The characteristic time for collision ( $\tau_c$ ) was defined as the average collision time between two particles, and the time for two contacted particles to coalescence was  $\tau_f$ , and  $\alpha$  was defined as  $\tau_c/\tau_f$ . When  $\tau_c \gg \tau_f$  ( $\alpha \rightarrow \infty$ ), the coalescence rate is much faster than the collision rate and is not a strong function of properties of materials. When  $\tau_f \gg \tau_c$  ( $\alpha \rightarrow 0$ ), colliding particles cease to form a fractal-like agglomerates. The primary particle size is mainly a function of the parameters that control the rate of coalescence. The intermediate situation ( $\alpha \rightarrow 1$ ) may commonly be appeared in the real synthesizing process. In this case, the presence of higher temperature leads to the higher

sintering rate and favors to form the spherical and the greater particles (Friedlander, 2000; Kodas and Hampden-Smith, 1999; Kuster and Pratsinis, 1995).

The mechanisms of coagulation and coalescence have been utilized for narrowing particle size distribution. The narrowing size distribution of particles was produced by avoiding coagulation of particles (Adachi et al, 2003; Kim et al., 2003; Nakaso et al., 2003a; Kuster and Pratsinis, 1995).

On the contrary, narrowing size distribution of particles also can be approached by enhancement of coalescence/sintering rate (Lee and Choi, 2002; Nakaso et al., 2003b; Tsantilis and Pratsinis, 2004a).

### 2.3.3. *Condensation controlled synthesis*

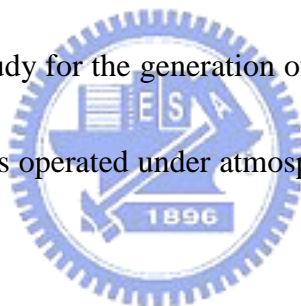
The mode of condensation controlled synthesis is often occurred at low concentration of particles. In this mode, the nucleated particles were grown by the mechanism of condensation. Not only the monomers were condensed to the surface of particles, but also the precursor was deposited on it. The particles grown by the condensation of monomers and the reaction of deposited precursor on the surface is shown in Figure 2.8, using the  $\text{TiO}_2$  particle as an example.

In the condensation controlled synthesis, the diameter of particle, surface area, concentration of monomer, reactor temperature, and the residence time are all influential factors of the size distribution of generated particles. Some studies indicated that the surface grown of  $\text{TiO}_2$  could be utilized for narrowing the size distribution of particles by increasing the surface reaction rate or the residence time (Artelt et al., 2005; Kuster and Pratsinis, 1995; Spicer et al., 2002; Tsantilis and

Pratsinis, 2004a). Such higher rate of condensation and surface reaction lead to the higher growth rate of smaller particles than that of greater particles (Yin and Alivisatos, 2005).

#### 2.3.4. Dielectric barrier discharge

The atmospheric pressure plasma of dielectric barrier discharge (DBD) was developed for ozone production by Siemens in 1852. It has also been applied to the air pollutant removals (Chang et al., 1992; Lin and Bai, 2001), surface treatment (Thyen et al., 1997), and the SiO<sub>2</sub> thin film deposition (Foest et al., 2003; Martin et al., 2004). The atmospheric pressure plasma has also been utilized for enhancing the capture of ultra-fine particles (Kulkarni et al., 2002). An atmospheric pressure plasma process was first employed in this study for the generation of nanoparticles. It is regarded as one of the PECVD processes except that it is operated under atmospheric pressure and temperature (Bai et al., 2004; Chen et al., 2006).



The chemical reactions in plasma can be classified into homogeneous and heterogeneous reactions. The homogeneous reactions occur between species in the gaseous phase as the result of inelastic collisions between electrons and heavy species (Grill, 1992; Lieberman & Lichtenberg, 1994). Table 2.4 lists the homogeneous reactions of electrons with heavy species and reactions between heavy species. The major energy transfer from electrons to heavy species takes place by inelastic collisions, and then leads to a variety of reactions. The excitation of molecule A<sub>2</sub> can be vibrational, rotational, or electronic. The dissociative attachment, ionization and the dissociation are the major source for production of atoms, free radicals and negative ions in plasma (Grill, 1992).

Reactions between heavy species occur during the collisions of molecules, atoms, radicals, and ions.

The reactions were separated in two types, ion-molecule and radical-molecule reactions. The density of radicals is much higher than that of ions in plasma, but ion-molecule reactions can have significant contributions to plasma chemistry and can enhance the rate of the total reaction occurring in the plasma (Grill, 1992; Lieberman & Lichtenberg, 1994).



**Table 2.4 Homogeneous chemical reactions in plasma reactor (summarized from Grill, 1992)**

<b>Reactions of electrons with heavy species</b>	
<i>Excitation</i>	$e + A_2 \rightarrow e + A_2^*$
<i>Dissociation</i>	$e + A_2 \rightarrow e + 2A$
<i>Dissociative ionization</i>	$e + A_2 \rightarrow e + A^+ + A^-$
<i>Ionization</i>	$e + A_2 \rightarrow 2e + 2A^+$
	$e + A_2 \rightarrow 2A^-$
	$e + A_2 \rightarrow 2e + A^+ + A^-$
<i>Recombination</i>	$e + A_2^+ \rightarrow A_2$
<i>Detachment</i>	$e + A_2^- \rightarrow A_2$
<b>Reactions between heavy species</b>	
<b>Ion-molecule reaction</b>	
<i>Recombination of ions</i>	$A^+ + B^- \rightarrow AB + h\nu$
	$A^+ + B^- \rightarrow A^* + B^* + h\nu$
	$M + A^+ + B^- \rightarrow AB + M$
<i>Charge transfer</i>	$A^+ + A \rightarrow A + A^+$
<b>Radical-molecule reaction</b>	
<i>Electron transfer</i>	$A + B \rightarrow A^+ + B^-$
<i>Ionization</i>	$A + B \rightarrow A^+ + B + e$
<i>Penning ionization</i>	$B^* + A \rightarrow A^+ + B + e$
<i>Penning dissociation</i>	$B^* + A_2 \rightarrow 2A + B$

A: Gas atom

B: Gas atom

M: The three body

\*: Excited state



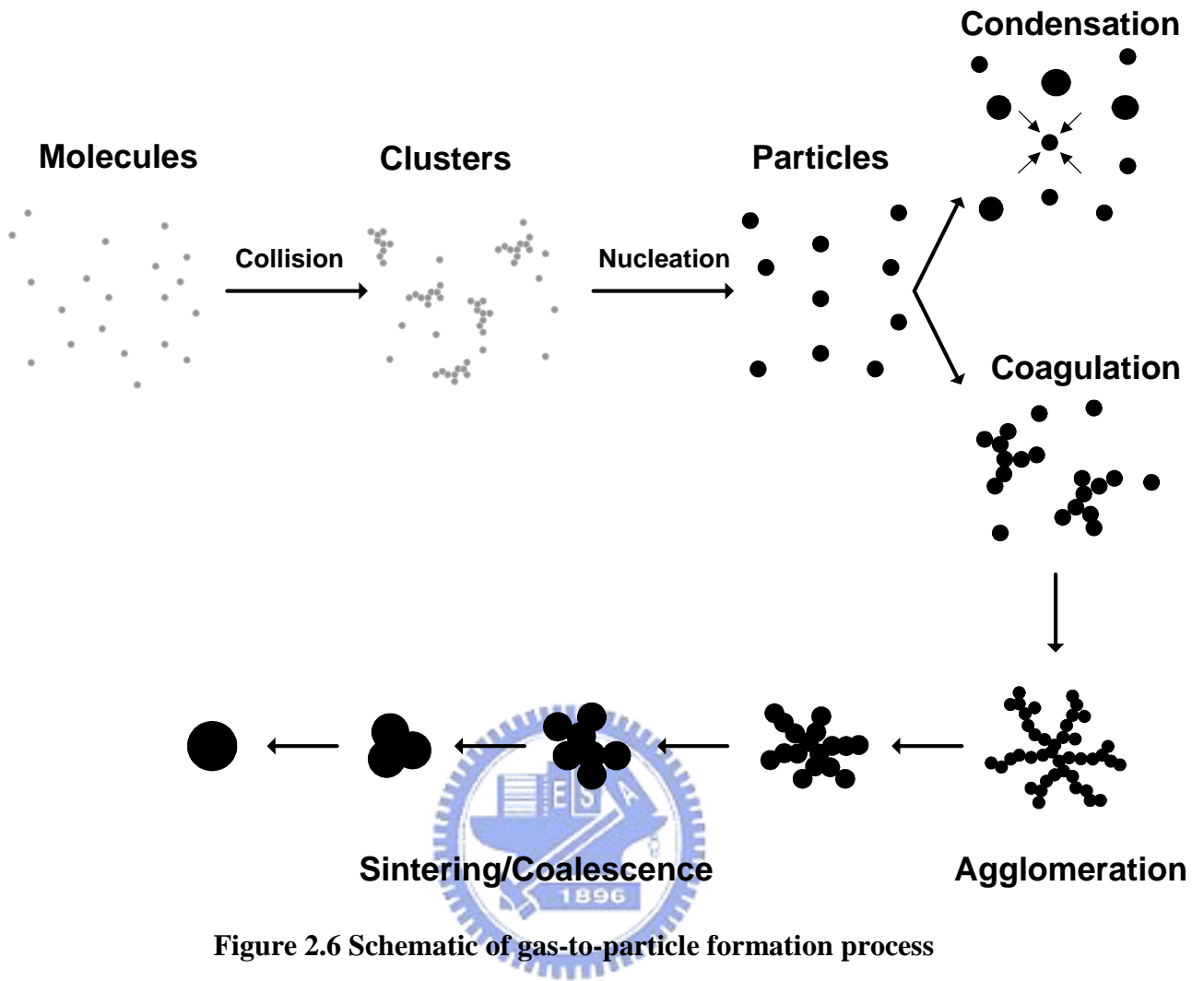


Figure 2.6 Schematic of gas-to-particle formation process

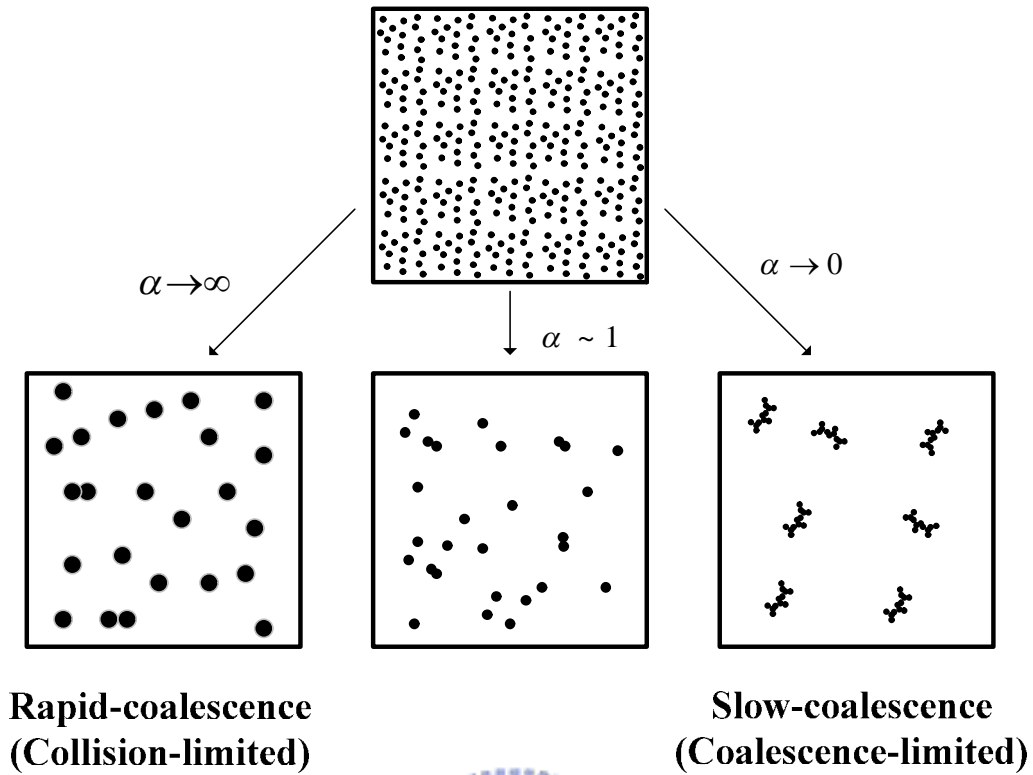


Figure 2.7 Effect of characteristic times (Friedlander, 2000)

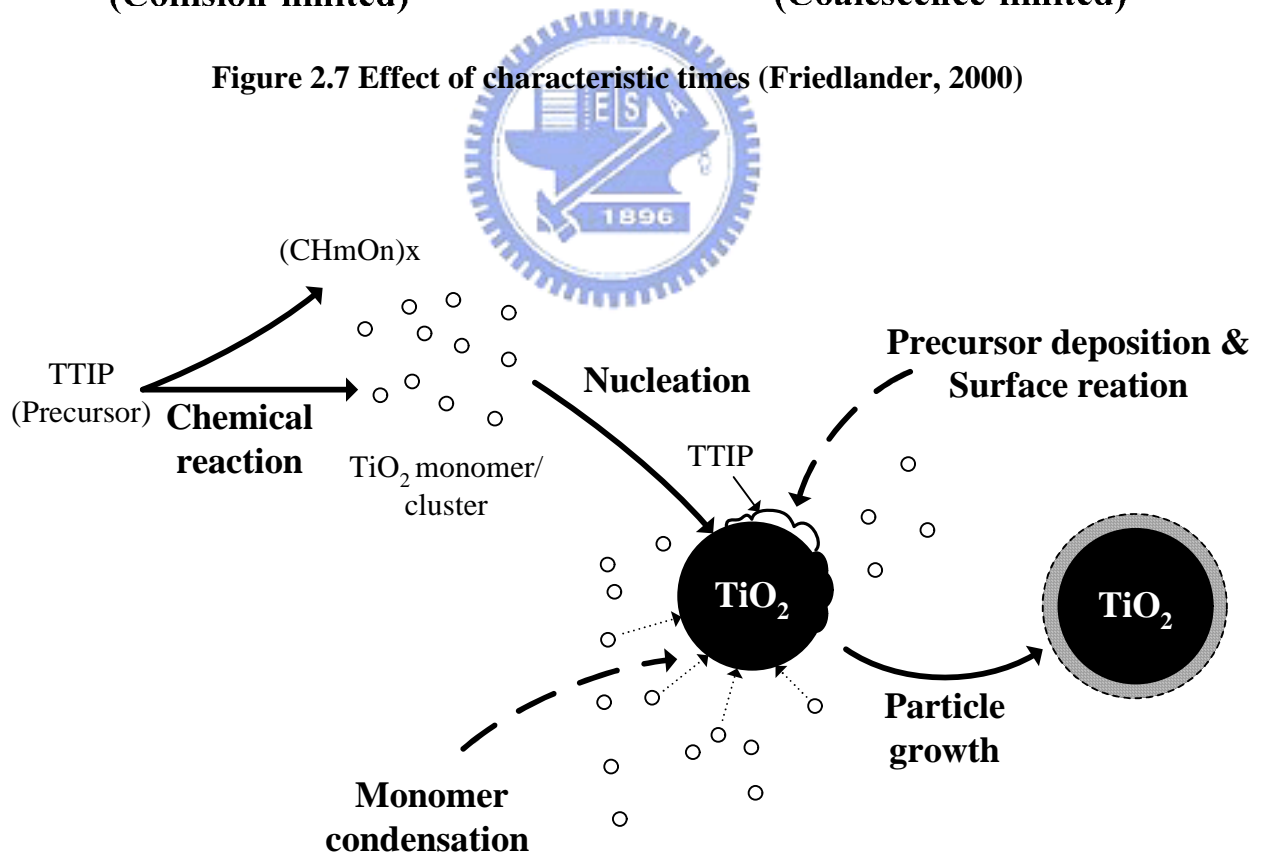


Figure 2.8 Condensation mechanism of particle growth

## CHAPTER THREE EXPERIMENTAL METHODS

### 3.1. PREPARATION OF THE N-DOPED TiO<sub>2</sub> PHOTOCATALYST

#### 3.1.1. Preparing N-doped TiO<sub>2</sub> particles under different process parameters

The APPENS process for generating TiO<sub>2</sub> nanoparticles is sketched in Figure 3.1. The aerosol reactor was a wire-tube type DBD reactor operated at atmospheric pressure and low temperature conditions. The plasma also can be utilized as plate type reactor also shown in figure 3.1. Titanium tetraisopropoxide (TTIP; Ti(OC<sub>3</sub>H<sub>7</sub>)<sub>4</sub>; 98%, Acros, USA) and H<sub>2</sub>O were used as the precursor solutions for generating TiO<sub>2</sub> nanoparticles in this study. The precursors were vaporized and sent into the plasma reactor via passing the carrier gas through two series of impingers, they were controlled at temperatures (TB101, Tungtec instrument, Taiwan) of 100~200°C and 25°C, respectively, for TTIP and water. The N<sub>2</sub> carrier gas was controlled by mass flow controllers (5860E, Brooks, USA), and the total flow rate of precursor vapors was 137.4 sccm (cm<sup>3</sup>/min at 0°C). The applied voltage of plasma system was supplied by alternative current (AC) power supply (2700M-05, Chenhwa, Taiwan) and amplifier (1:107, Hsinhsin). The plasma reactor was made of Pyrex glass with 21 mm I.D., 23 mm O.D. and 200 mm in length. One electrode was a stainless steel (SS 316) rod of 2 mm in diameter positioned along the central line of the reactor. The other electrode was a sheet of stainless steel mesh wrapped around the reactor with wrapping length of 135 mm.

The applied voltage, frequency and the precursor molar ratio were the controlling factors of particle size distribution generated by the APPENS process, as shown in Table 3.1. The applied voltage was adjusted in the range 0~10.20 kV, the frequency of AC was 60, 120 or 240 Hz, and the precursor molar ratios controlling TTIP/H<sub>2</sub>O volumetric flow rate ratio, were from 0.125 to 8. The corresponding TTIP/H<sub>2</sub>O molar ratios were calculated from the vapor pressure of TTIP and H<sub>2</sub>O to be 0.4 to 76.1, based on the equilibrium equation at a certain TTIP bubbling temperature (Duminica et al., 2004),

$$\log P_{TTIP}(\text{Torr}) = 9.465 - \frac{3222}{T(\text{K})}, \quad (8)$$

where  $P_{TTIP}$  is the TTIP vapor pressure (Torr), and  $T$  is the TTIP bubbling temperature (°K).

### 3.1.2. Preparation of different types of N-doping status of TiO<sub>2</sub> photocatalysts

The same APPENS reactor was utilized for preparing different type of N-doping status of TiO<sub>2</sub> photocatalysts. The alternative current (AC) at 60 Hz frequency was applied to the APPENS reactor. The reactor was operated at 9.6 kV/cm electrical field strength under atmospheric pressure conditions. The compositions of carrier gas (Ar/N<sub>2</sub>/O<sub>2</sub>) were controlled by mass flow controllers. The total flow rate of precursor vapors was 137.4 sccm with TTIP/H<sub>2</sub>O volumetric flow rate ratio of 1.0. The carrier gases of N<sub>2</sub> or O<sub>2</sub> molecules were excited in the non-thermal plasma environment and N atoms or N-containing molecules were implanted into the TiO<sub>2</sub> vapor precursors or particles. The product particles were deposited on the inner surface of the reactor for further photocatalytic activity test and particle characterization.

The four different types of N-doping in the TiO<sub>2</sub> particles were conducted under different plasma and annealing gas compositions. The photocatalysts produced under the four tests were denoted as SYN1 to SYN4 in the hereafter. After 10 hours of the plasma process, the product particles were then annealed at 500°C for 3 hours with a gas flow rate of 9.2 sccm. SYN1 and SYN2 were processed under the same plasma gas environment composed of pure N<sub>2</sub> gas. SYN3 was produced without the presence of N<sub>2</sub> gas for the purpose of producing pure TiO<sub>2</sub> particles without any N-doping. The plasma gases for producing SYN4 were combined 10% N<sub>2</sub>, 10% O<sub>2</sub>, and 80% Ar, and the annealing gases were 20% N<sub>2</sub> and 80% Ar.

Table 3.2 shows synthesized gas compositions for obtaining different types of N-doping in the TiO<sub>2</sub> particles. SYN1 and SYN2 were processed under the same plasma gas environment composed of pure N<sub>2</sub> gas, then SYN1 was annealed under air environment while SYN2 was annealed with 20% N<sub>2</sub> + 80% Ar gases. SYN3 was produced without the presence of N<sub>2</sub> gas for the purpose of producing pure TiO<sub>2</sub> particles without any N-doping. It was processed at 20% O<sub>2</sub> + 80% Ar plasma and annealing gas environment. The plasma gases for producing SYN4 were 10% N<sub>2</sub> + 10% O<sub>2</sub> + 80% Ar, and the annealing gases were 20% N<sub>2</sub> and 80% Ar.

**Table 3.1 List of parameters for producing different TiO<sub>2</sub> particles**

Bubbling temperature (°C)	Frequency (Hz)	Applied voltage (kV)	Precursor molar ratio (TTIP/H <sub>2</sub> O)
150	60	0	11.9
		6.48	11.9
		8.58	11.9
		9.6	0.4, 0.7, 1.5, 3.0, 6.0, 11.9, 23.9
		10.2	11.9
		10.2	11.9
150	120	10.2	11.9
	240	10.2	11.9
	200	60	9.6

**Table 3.2 Plasma and annealing gas compositions for synthesizing different TiO<sub>2</sub> based photocatalysts.**

Photocatalysts	Plasma Gas	Anneal Gas
SYN1	100% N <sub>2</sub>	Air(20% O <sub>2</sub> + 80% N <sub>2</sub> )
SYN2	100% N <sub>2</sub>	20% N <sub>2</sub> + 80% Ar
SYN3	20% O <sub>2</sub> + 80% Ar	20% O <sub>2</sub> + 80% Ar
SYN4	10% N <sub>2</sub> + 10% O <sub>2</sub> + 80% Ar	20% N <sub>2</sub> + 80% Ar

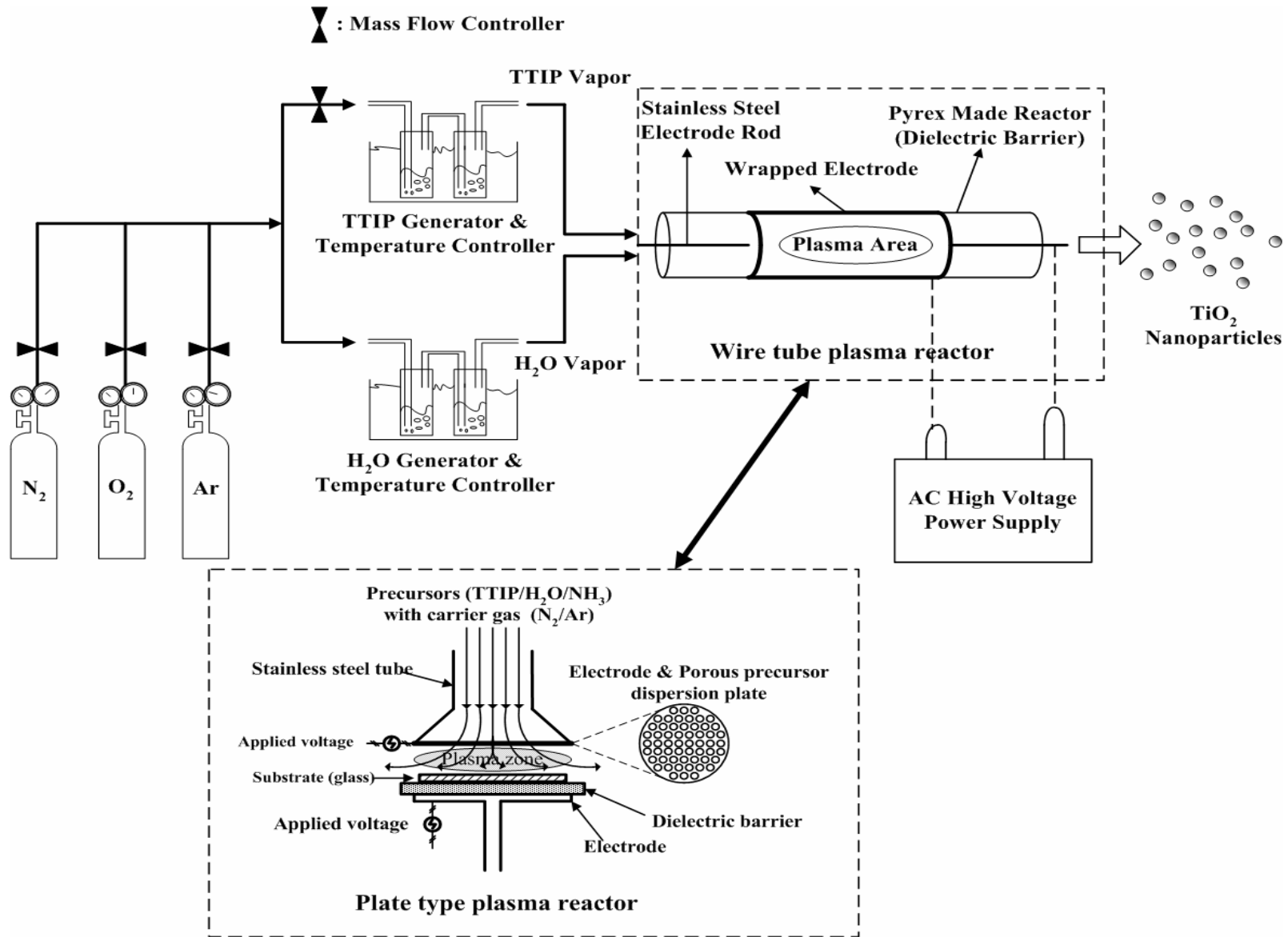


Figure 3.1 Schematic diagram of APPENS reactor for producing TiO<sub>2</sub> nanoparticles.

## 3.2. CHARACTERIZATION OF N-DOPED TiO<sub>2</sub> PHOTOCATALYST

### 3.2.1. The morphology, size, crystal phase and absorption spectra of N-doped TiO<sub>2</sub> particles

The nanoparticles deposited on the reactor wall were collected for further analyses by Scanning Electron Microscope (SEM; S4700, Hitachi, Japan) and Transmission Electron Microscope (TEM; TECNAI 20, Philips, Japan). The SEM microscope was operated at accelerating voltage of 5-15 kV and the images were collected under a vacuum of 10<sup>-8</sup> torr, all of the samples for SEM analysis were coated with platinum. The samples for TEM analysis were coated on the copper mesh and operated at accelerating voltage of 200 kV and under a vacuum of 10<sup>-9</sup> torr. The X-ray Powder Diffractometer (XRPD; Rigaku, Japan) was used to determine the crystal phase of produced particles. The XRPD was operated under 30kV and 20mA with Cu target, all samples for XRPD analysis were coated on the glass (20 mm× 20 mm) as thin films. The geometric mean diameter (D<sub>pg</sub>) and geometric standard deviation (σ<sub>g</sub>), were determined based on averaging over 80 particles as observed from the SEM images. And for on-line measurement of particle size distribution, a Scanning Mobility Particle Sizer (SMPS; 3080L, TSI, USA) was connected after the APPENS reactor to determine the D<sub>pg</sub>, σ<sub>g</sub>, and the total mass concentration (TMC) of generated particles. The volumetric flow of SMPS measurement was 0.3 L/min. In order to achieve the minimum required flow rate of the SMPS, a N<sub>2</sub> dilution gas stream was introduced after the plasma reactor with a N<sub>2</sub>/aerosol dilution flow rate ratio of 1.0 (i.e. the inlet flow rate to the SMPS is double of the reactor outlet flow rate). To further prevent agglomeration of the TiO<sub>2</sub> particles, a N<sub>2</sub>/aerosol dilution flow



rate ratio of 12.0 was sometimes introduced (i.e. the inlet flow rate to the SMPS is 13 times of the reactor outlet flow rate). The UV–Visible diffuse reflection spectra were measured by a spectrophotometer (U-3010, Hitachi, Japan) with 60 mm integrating sphere. The scan speed of spectrophotometer was 600 nm/min, all samples for diffuse reflection spectra analysis were coated on the glass (20 mm× 20 mm) as thin film.

### 3.2.2. The N-doping status of the N-doped TiO<sub>2</sub> particles

The N-doping status of the N-doped TiO<sub>2</sub> was analyzed by XPS (PHI 1600, Perkin Elmer) using Al K<sub>α</sub> X-ray source (1486.6 eV) and under ultra-high vacuum ( $5.0 \times 10^{-9}$  torr). All data from XPS analysis were calibrated with the binding energy of C in 284.5 eV. It must be noted that binding energy of XPS data is binding of electron in the atom, not binding between atoms. So one can not directly assign a chemical bond between the Ti, O and N atoms in the presence of a given peak in XPS spectra. But one can speculate the chemical bond, e.g., it is Ti-N or Ti-(NO), by a cross comparison of the chemical shifts of Ti, O and N atoms from the XPS data.

Thus in this study chemical bonds between Ti, N and O atoms were proposed first by comparing the chemical shift of elements and then confirmed by cross comparison of the chemical shift of Ti 2p, O 1s and N 1s atoms. The raw XPS data were fitted using a non-linear least-squares splitting program by Gaussian- Lorentzian function after performing a Shirley-type background subtraction. The binding energy of Ti 2p, N 1s and O 1s be identified as TiO<sub>2</sub> and TiN at 2p<sub>3/2</sub> and 2p<sub>1/2</sub>, and be grouped into several ranges as N(I)~N(IV) for N 1s and O(I)~O(III) for O 1s.

### 3.3. PHOTOCATALYTIC DECOMPOSITION OF VOCs AND NO<sub>x</sub> BY TiO<sub>2</sub>

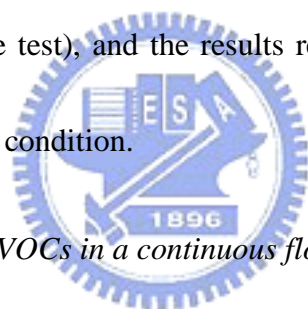
#### PHOTOCATALYST

##### 3.3.1. Photocatalytic degradation of VOCs in a batch reactor

A batch photocatalytic reactor for IPA and Toluene removal is sketched in Figure 3.2(a). The reactor was essentially the same device as the one used for producing the TiO<sub>2</sub> particles, except that the inlet and outlet ends were sealed to form a batch-type configuration. Before the photocatalytic reaction test, small amounts of IPA (0.04 μL) or toluene (0.01 μL) were injected into the sealed reactor by syringe at a constant temperature of 45±3°C and relative humidity of 70±5%. After 60 min, the IPA and toluene reached a steady-state vapor concentration of 145±1 and 250±10 ppm as confirmed by a GC/FID (9800, China Chromatography) at the oven temperature of 90°C. The illuminating light was then turned on and the concentrations of target pollutants subjected to the photocatalytic decomposition by either the TiO<sub>2</sub> or the N-doped TiO<sub>2</sub> photocatalysts were recorded. To avoid the diffusion limitation in a batch reactor, the light was turned off for 30 min after each sampling to ensure well mixture of the air pollutant molecules, and then the light was turned on again to continue the photocatalysis tests.

The illumination light sources used in the batch and continuous flow photocatalytic decomposition studies were either UV (364.2 nm; FL10BLB, Sankyo Denki) or visible light (FL10D-EX, Tyo Light) sources having the same output power (10 W). To facilitate understanding of the prepared photocatalyst for indoor air pollution control application, the visible light bulb used

in this study is simply the one used in household living space. Both the intensity and the spectra of the light sources were obtained from a spectrophotometer (USB2000, Ocean Optics). The intensities of illumination in the reactor were  $3.78 \text{ mW/cm}^2$  for UV light source and  $4.81 \text{ mW/cm}^2$  for visible light source. The light spectra of the visible light source are shown in Figure 3.3 with major peaks observed at 435, 488, 545, 587 and 611 nm. One can also observed a very small peak for visible light lamp at UV range of 364 nm with intensity of  $0.35 \text{ mW/cm}^2$ . To ensure the effect of this small peak at 364 nm on visible light photocatalysis, a photocatalysis test was also conducted with UV lamp (364.2 nm) of  $0.43 \text{ mW/cm}^2$  intensity (a precise control of the light intensity to be  $0.35 \text{ mW/cm}^2$  was not feasible during the test), and the results revealed that both the IPA and toluene removals can be neglected under this condition.



### 3.3.2. Photocatalytic degradation of VOCs in a continuous flow reactor

In addition to the batch-type decomposition studies, continuous flow (with a schematic diagram shown in Figure 3.2(b)) studies targeting toluene removal were also performed using 5 mm glass beads (Beco Mfg Corp., German) as the packing media. The glass beads were directly deposited with N-doped  $\text{TiO}_2$  after 10 hours of the plasma process. The Brunauer-Emmett-Teller (BET) surface area of the glass beads was determined (ASAP 2020, Micromeritics) to be  $0.0278 \text{ m}^2/\text{g}$  with negligible pores by nitrogen-adsorption-desorption isotherm at  $77 \text{ }^\circ\text{K}$ . The mass of the coated photocatalysts per clean glass beads was  $1.17 \text{ mg/g}$ , and the mass of photocatalyst per surface area of clean glass beads was  $42.24 \text{ mg/m}^2$ .

For comparison basis, approximately the same amounts ( $\pm 0.07$  mg/g) of ST01 and P25 photocatalysts as the N-doped  $\text{TiO}_2$  were also coated on the glass beads and tested in separate reactors under the identical conditions. The commercial photocatalysts of ST01 (Ishihara Sangyo) and P25 (Degussa) powders were dispersed into the deionized water to a concentration of 50 g/L. Then the clean glass beads were dipped into the slurries and dried at  $105^\circ\text{C}$ . The glass beads were weighted before and after coating procedure to determine the actual coating amount of ST01 and P25 on the glass beads.

The toluene vapor was obtained from an impinger with clean air as the carrier gas, with the total gas flow rate of 18.3 sccm and typical toluene concentration of  $463 \pm 13$  ppm. The reaction temperature and the relative humidity were maintained at  $25^\circ\text{C}$  and 70%, respectively. The corresponding residence time in the continuous flow photocatalytic reactor was 2.35 min. Blank tests were conducted for both batch and continuous flow photocatalytic tests. The blank tests included those conducted with catalyst but without illumination, and those without catalyst but with light illumination. Each type of blank tests showed that the removals of IPA and toluene vapors are negligible.

### 3.3.3. Photocatalytic degradation of $\text{NO}_x$ in a continuous flow reactor

The weight of synthesized N-doped  $\text{TiO}_2$  was 0.1 g coated on a glass substrate by a spray gun (GP-1, Longyea, Taiwan). The dimension of glass substrate was 5 cm  $\times$  20 cm (W $\times$ L). A continuous flow photocatalytic reactor for NO removal is shown in Figure 3.4. The distance

between the quartz window and the bottom of the reactor is 1 cm. The illumination light sources used in the continuous flow photocatalytic reactor were in either UV or visible light ranges. The intensities of illumination in the reactor were  $2.5 \text{ mW/cm}^2$  for UV light source and  $3.18 \text{ mW/cm}^2$  for visible light source. The inlet concentration of NO was 10-18 ppm, the relative humidity was  $50 \pm 5\%$ , the total volumetric flow was 137.4 sccm and the residence time was 33.3 sec. The chemiluminescence NO/NO<sub>2</sub> analyzer (S5012, SIR, Madrid-Spain) was utilized for the NO, NO<sub>2</sub> and NO<sub>x</sub> measurements during photocatalytic tests. The operating temperatures of converter and internal valves in NO/NO<sub>2</sub> analyzer were 240°C and 40°C, respectively.



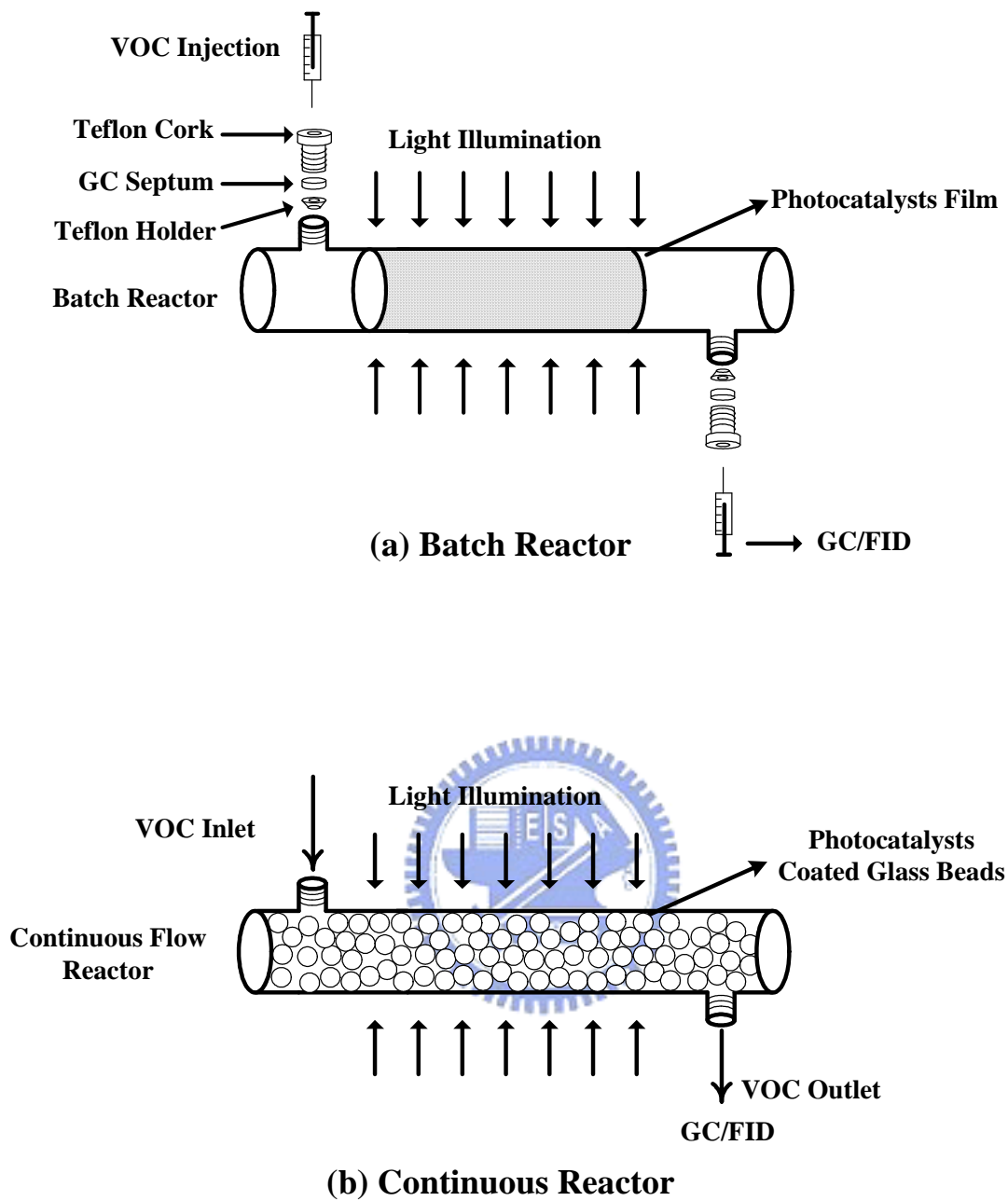


**Figure 3.2 Schematics of the (a) batch type and (b) continuous flow photocatalytic reactors for VOCs removal.**

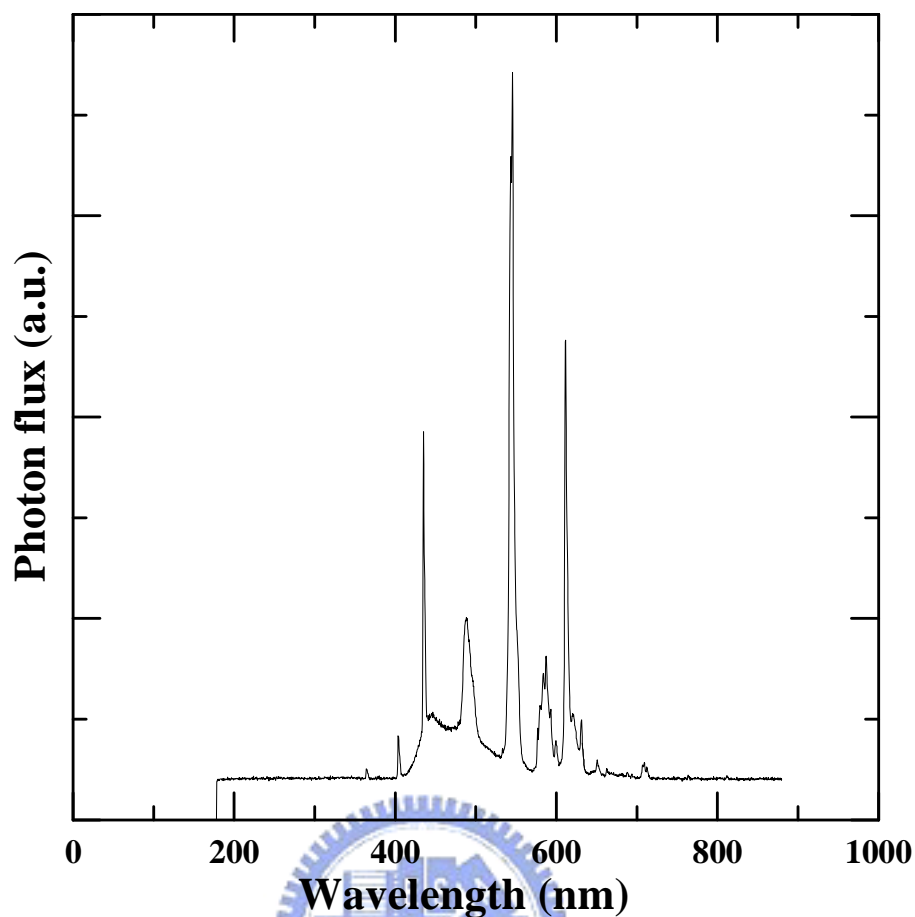


Figure 3.3 The light spectra of the visible light source used in this study. The five major peaks were observed at 435, 488, 545, 587 and 611 nm.

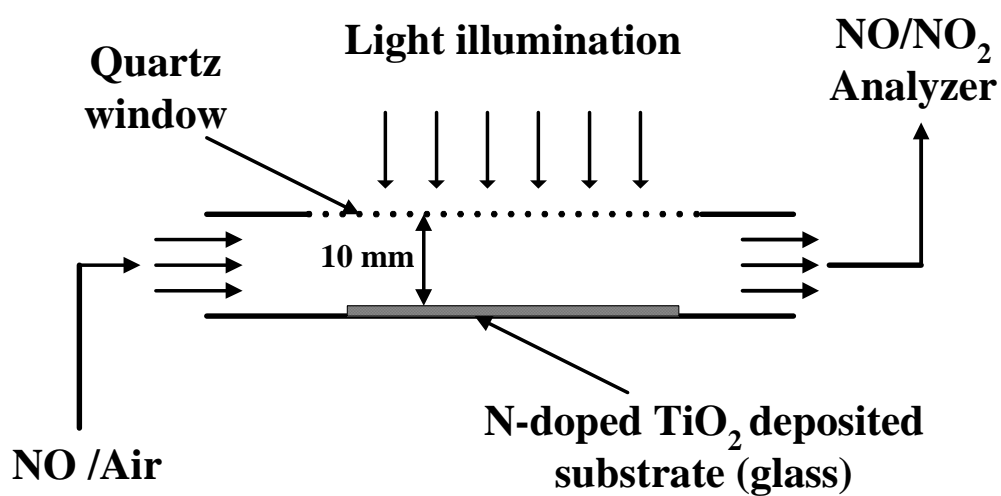


Figure 3.4 Continuous flow reactor for photocatalytic removal of NO.

## CHAPTER FOUR RESULTS AND DISCUSSION

### 4.1. PREPARATION OF N-DOPED TiO<sub>2</sub> PHOTOCATALYST BY APPENS PROCESS

#### 4.1.1. The feasibility of non-thermal plasma to generate nanosize TiO<sub>2</sub>

Because the non-thermal plasma process has never been applied to generate both TiO<sub>2</sub> and N-doped TiO<sub>2</sub> particles, the feasibility of the process for generating TiO<sub>2</sub> particles was tested first in this study. As the system was operated in the absence of applying atmospheric pressure plasma, polydisperse particles were formed as observed by SEM image shown in Figure 4.1(a). The particle distribution of size was very broad, which ranged from nano- to micron-sizes. The micro-sized particles can be either in spherical, porous or doughnut shapes, forming from direct hydrolysis of TTIP precursor vapors or highly agglomeration of primary nano-TiO<sub>2</sub> particles.

The SEM and TEM images of particles produced in plasma environment, i.e. by the APPENS process, are shown in Figures 4.1(b) and 4.1(c). As the precursor vapors were nucleating to form primary particles, their growth was hindered due to the AC applied voltage that produced ions of the same sign at a time. The particles were all charged either in positive sign or in negative sign and repelled each other. Besides, the local thermal equilibrium plasma under alternating current provides a near neutral environment, thus a neutralizer may not be required after the non-thermal plasma reactor.



The SEM and TEM image of particles revealed that a change in the precursor bath temperatures from 100 to 175°C did not alter the size of produced particles. Similarly by collecting particles at different locations of the reactor showed that a change in the plasma residence time from 1 to 17 secs did not change the particle size. An increase in the TTIP/H<sub>2</sub>O precursor ratio, however, resulted in an increase in the particle size. In the present study, the photocatalytic particles with size ranging from 20 to 40 nm are achievable for TTIP/H<sub>2</sub>O ratios of 0.125 to 4.

The titania-based product particles for the non-thermal plasma process were characterized by XRPD and the result is shown in Figure 4.2. As compared to the Joint Committee on Powder Diffraction Standards (JCPDS) file, the peaks of product particles were confirmed to be as anatase form.



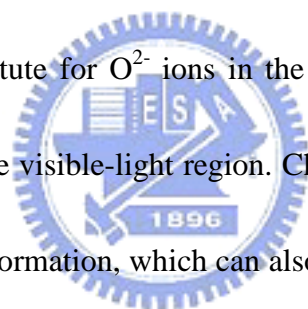
In summary, it has been demonstrated that the non-thermal plasma process is application in producing anatase TiO<sub>2</sub> therefore named as APPENS in hereafter.

#### 4.1.2. Characterization of the N-doped TiO<sub>2</sub> photocatalyst

The evidence of the nitrogen doping is provided by the XPS spectra of Ti 2p and N 1s, as shown in Figure 4.3. TiO<sub>2</sub> is characterized with peaks appearing at around 458~459 eV for Ti 2p<sub>3/2</sub> and 464 eV for Ti 2p<sub>1/2</sub> (Jill Ed., 1992). The presence of TiO<sub>2-x</sub>N<sub>x</sub>, however, tends to shift the Ti 2p peaks to lower binding energy (Miao et al., 2004; Chen et al., 2005). More importantly, the presence of N-doping in the TiO<sub>2</sub> particles is substantiated by the N 1s spectra, where a significant peak at around 402 eV and a minor peak at around 400 eV were observed for the photocatalysts doped with

nitrogen. In contrast, there were no obvious N 1s peaks for the TiO<sub>2</sub> photocatalysts prepared in O<sub>2</sub>/Ar environment.

These feature peaks at 400~402 eV were assigned either to be bound to hydrogen (Diwald et al., 2004), to the chemisorbed  $\gamma$ -N<sub>2</sub> (Yang et al., 2004a) or to the formation of oxynitride (Chen et al., 2005) as the N-doping status. For examples, Diwald et al. (2004) showed that the peak observed at 399.6 eV is responsible for the shift of the photochemical threshold down to ~2.4 eV. And this form of nitrogen is most likely located in an interstitial site bound to hydrogen. Diwald et al. (2004) also indicated that this form of nitrogen doping disagrees with the conclusion of Asahi et al. (2001), who reported that nitride ions that substitute for O<sup>2-</sup> ions in the TiO<sub>2</sub> lattice are the necessary dopant species for TiO<sub>2</sub> photocatalysis in the visible-light region. Chen and Burda (2005) assigned the N<sub>1s</sub> peak observed at 402 eV to O-Ti-N formation, which can also enhance the photocatalytic activity in visible light region. In reference to literature data, it reveals that N-doping sites other than TiN observed at N 1s of 396 eV could also be responsible for effective photocatalysis in the visible light region. A detailed discussion on the N-doping status due to different process gas compositions will be present in section 4.3.



#### 4.1.3. Comparison of the APPENS process with other plasma processes

Values of the operating parameters and the basic properties of the N-doped TiO<sub>2</sub> prepared via the APPENS process are summarized in Table 4.1. These values are compared to the available literature data which employed other plasma processes for producing N-doped TiO<sub>2</sub> photocatalysts,

namely the ion-beam-assisted deposition (IBAD) and the radio frequency (RF) plasma-enhanced chemical vapor deposition (PECVD) processes.

As a common feature of all plasma processes, the particles produced by the APPENS process were firmly coated on the reactor surface and could not be easily removed by mechanical or chemical washing. Therefore, it is possible that the TiO<sub>2</sub> vapors were deposited onto the reactor surface (i.e. via CVD process) first and then crystallized to form TiO<sub>2</sub> particles. In addition to the common feature of firm coating and high quality films among all plasma processes, the APPENS process was operative under normal conditions (i.e., room temperature and atmospheric pressure) as opposed to the IBAD and the PECVD processes. Therefore, the photocatalyst prepared by the APPENS process could be deposited on a substantially wider variation of substrate materials. Furthermore, the power consumption of the APPENS process (<80 W) was less than that of the PECVD (100~500 W) and the IBAD (3 kW) processes.

The production rate of the N-doped photocatalyst was in the range of 60~94 nm/min as verified by the plate-type APPENS process, with a SEM image of the N-doped TiO<sub>2</sub> deposited on a glass substrate shown in Figure 4.4. This production rate is much greater than those exhibited by the IBAD and PECVD processes, presumably due to the higher gas flow rate of 137.4 sccm employed in this study as compared to those (~20 sccm) used in the IBAD and PECVD processes. It is also noted that although a direct comparison between the production rate of the wire-tube plasma reactor

and those of the IBAD and PECVD processes was not feasible, the total mass production rate in the wire-tube plasma reactor as collected by the glass beads ( $8.3 \pm 0.5$  mg/hr) was about 20 times greater than that in the plate-type plasma reactor ( $0.4 \pm 0.05$  mg/hr). Hence the production rate of the APPENS reactor should be higher than that of the IBAD and PECVD process because scaling up of the IBAD and PECVD processes for operating at higher flow rates are technically not feasible due to the necessity of vacuum condition.

The SEM and TEM images indicate that the produced particles were very uniform in size, whether or not nitrogen was doped into the  $\text{TiO}_2$  particles, as shown in Figure 4.1 (b), (c). The variation in the average diameters between 30 and 60 nm depended on the operating conditions such as the precursor ratio and the plasma intensity. The crystallite sizes were also calculated by the Scherrer equation (Musić et al., 1997),

$$D = \frac{0.9\lambda}{\beta \cos \theta} \quad (9)$$

where  $D$  (nm) is the crystallite size,  $\lambda$  (nm) is X-ray wavelength for the XRPD tests,  $\theta$  is Bragg angle and  $\beta$  is full width of diffraction at half of maximum intensity (FWHM) obtained from the XRPD pattern for the  $\text{TiO}_{2-x}\text{N}_x$  nanoparticles. The calculation results showed that the crystallite sizes were 22 nm for particles having an estimated average size of 25 nm based on averaging 62 primary particles observed in the TEM images.

To check the difference between the TEM observed particle size and the XRPD-determined crystallite size, the BET surface area measurements were conducted. The powder specific surface

area by nitrogen adsorption was determined to be 69.9 m<sup>2</sup>/g, thus the specific surface area-determined particle size ( $d_p$ ) was 22 nm using  $d_p=6/(\rho_p A)$ , where  $\rho_p$  is the density of anatase TiO<sub>2</sub> (3.83 g/cm<sup>3</sup>), and A is the BET specific surface area. Because there was no obvious porosity of the photocatalysts observed by the adsorption-desorption curve of BET measurement, one can conclude that the difference in TEM particle size and XRPD-determined crystallite size was mainly due to coagulation of crystallite particles. The particles collected directly from the substrate via the APPENS process were amorphous, but they became strictly anatase after being annealed at 500°C for 3 hrs. The anatase structure was observed regardless whether nitrogen was doped into TiO<sub>2</sub> photocatalysts.

#### 4.1.4. Summary



An APPENS process was proposed to produce N-doped TiO<sub>2</sub> photocatalyst. The produced TiO<sub>2-x</sub>N<sub>x</sub> nanoparticles were highly uniform and adjustable in size. The advantages of the APPENS process, as compared to other plasma processes for producing N-doped TiO<sub>2</sub> films or particles, encompass operation under normal temperature and pressure, as well as possessing a higher film deposition rate with lower power consumption. The titania based particle sizes ranged from 25 to 40 nm and they depended on the precursor ratio of TTIP/H<sub>2</sub>O. In addition to the application of the APPENS process to the production of photocatalyst in nano-size range, it has a potential application to serve as a continuous flow nanoparticle generator.

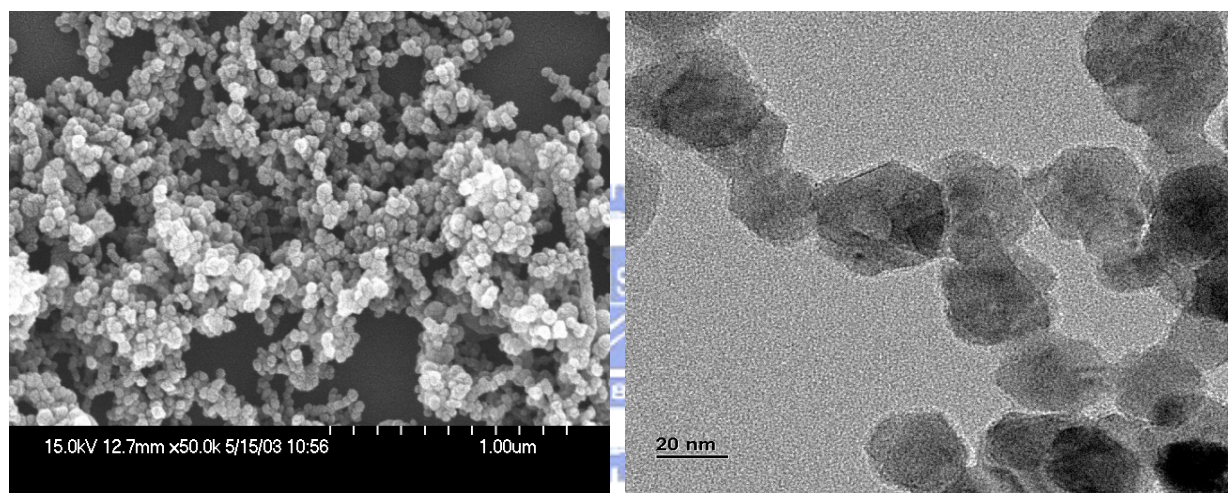
**Table 4.1 The operation parameters and the product properties of the APPENS process and other plasma processes for producing N-doped TiO<sub>2</sub> photocatalysts.**

<i>Properties</i>	<i>APPENS</i>	<i>Reference Processes</i>	
	<i>(This study)</i>	IBAD (Wu et al., 2005; Yang et al., 2004a; 2004b)	PECVD (Battison et al., 2000)
System Temp	298 °K	523~573 K	393~523 °K
Temp. of TTIP	423 °K	not available	313°K
System Pressure	~101300 Pa (i.e. ~1 atm)	10 <sup>-4</sup> ~10 <sup>-2</sup> Pa	60 Pa
Power	Wire tube: ~9 W; Plate: 60~80 W	3 kW (Wu et al., 2005)	10500 W
Gas Flow rate	137.4 sccm	<20 sccm	20 sccm
Production rate	60~94 nm/min (plate type)	6~12 nm/min	<10~25 nm/min
grain size	~12 nm (25 nm) <sup>a</sup>	20~200 nm	20~30 nm
Crystal phase	Amorphous, then to anatase after 3 hrs annealing at 773 K	Direct use of anatase source (Wu et al., 2005). Rutile TiO <sub>2</sub> source material transferred to amorphous or anatase (Yang et al., 2004a; 2004b)	Amorphous, then to anatase after 6 hrs annealing at 773 K.

<sup>a</sup>The grain size was around 22 nm as estimated by the Scherrer equation (Musić et al., 1997) based on XRPD data and the particle size was around 25 nm as observed from TEM photo images for tests shown in this study. The particle size may vary from 30~60 nm as the precursor ratio and the applied voltage were varied in the APPENS process.



(a)



(b)

(c)

**Figure 4.1(a) SEM images of titania based particles formed without atmospheric pressure plasma. (b)&(c) SEM & TEM images of titania based particles formed with applying atmospheric pressure plasma, the particles were with size ranging from 20 to 40 nm.**

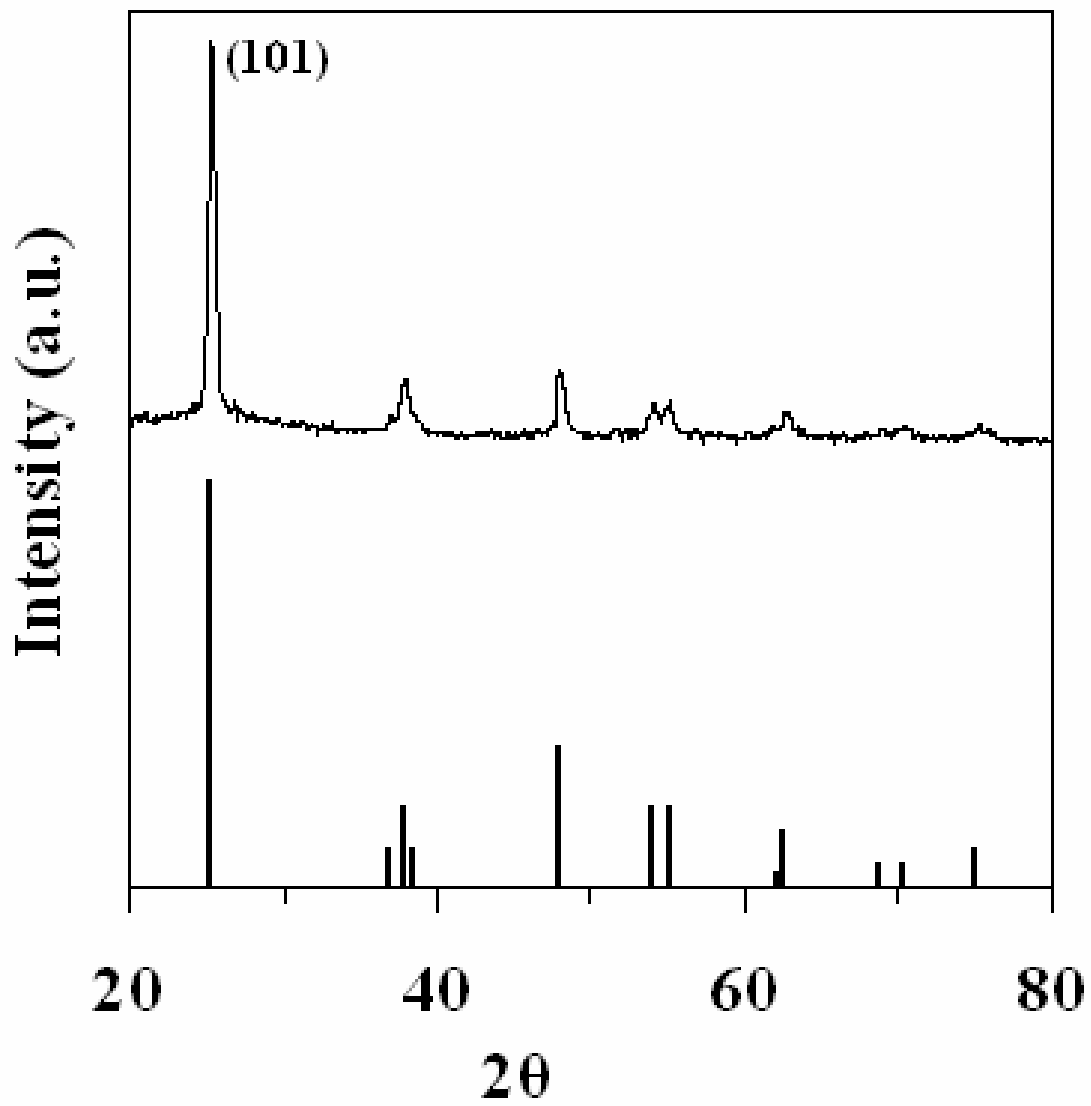


Figure 4.2 XRPD patterns of the Titania-based nanoparticle.



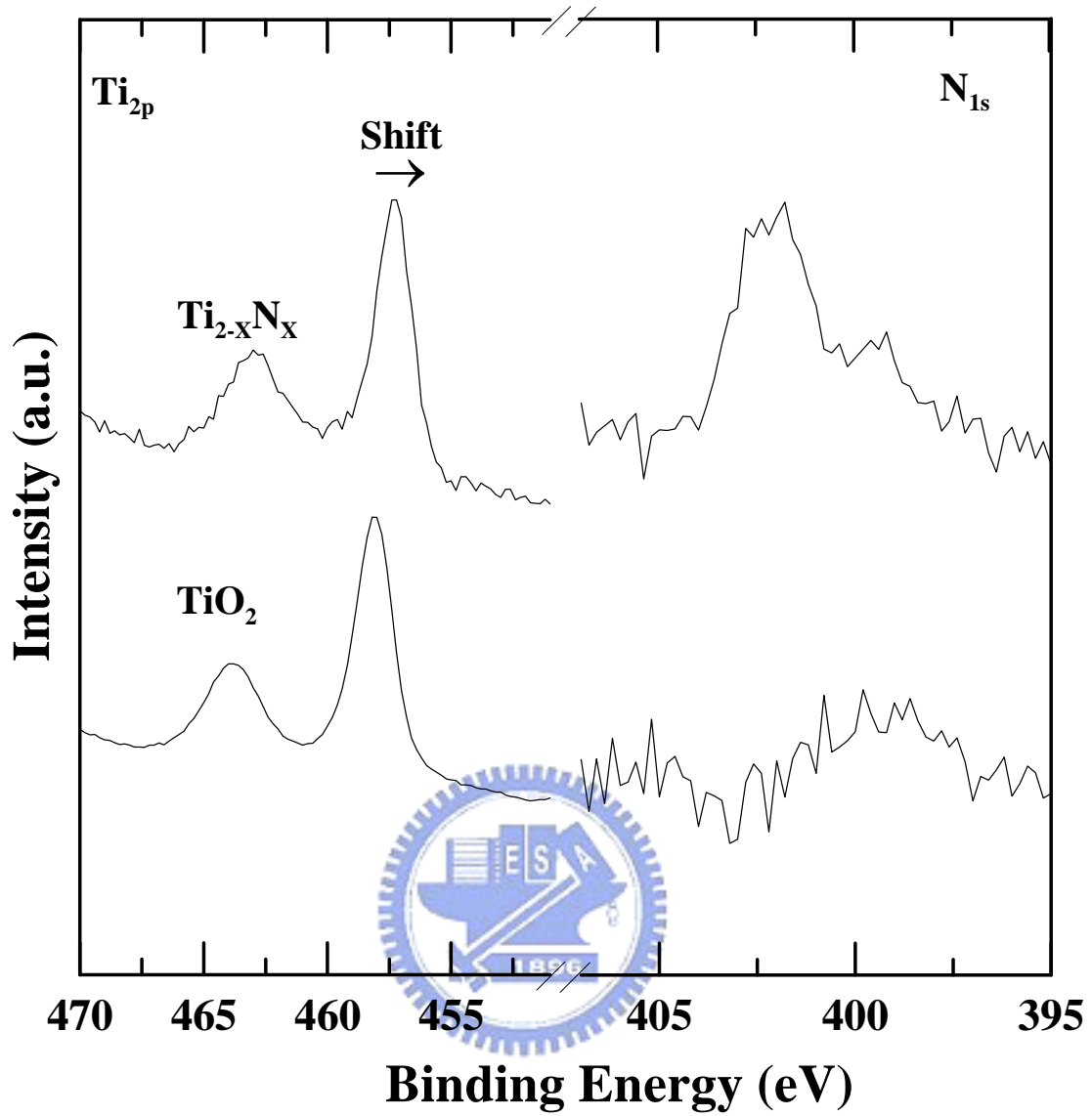


Figure 4.3 XPS spectra of Ti 2p and N 1s that show evidence of nitrogen doping into the  $\text{TiO}_2$  photocatalyst.

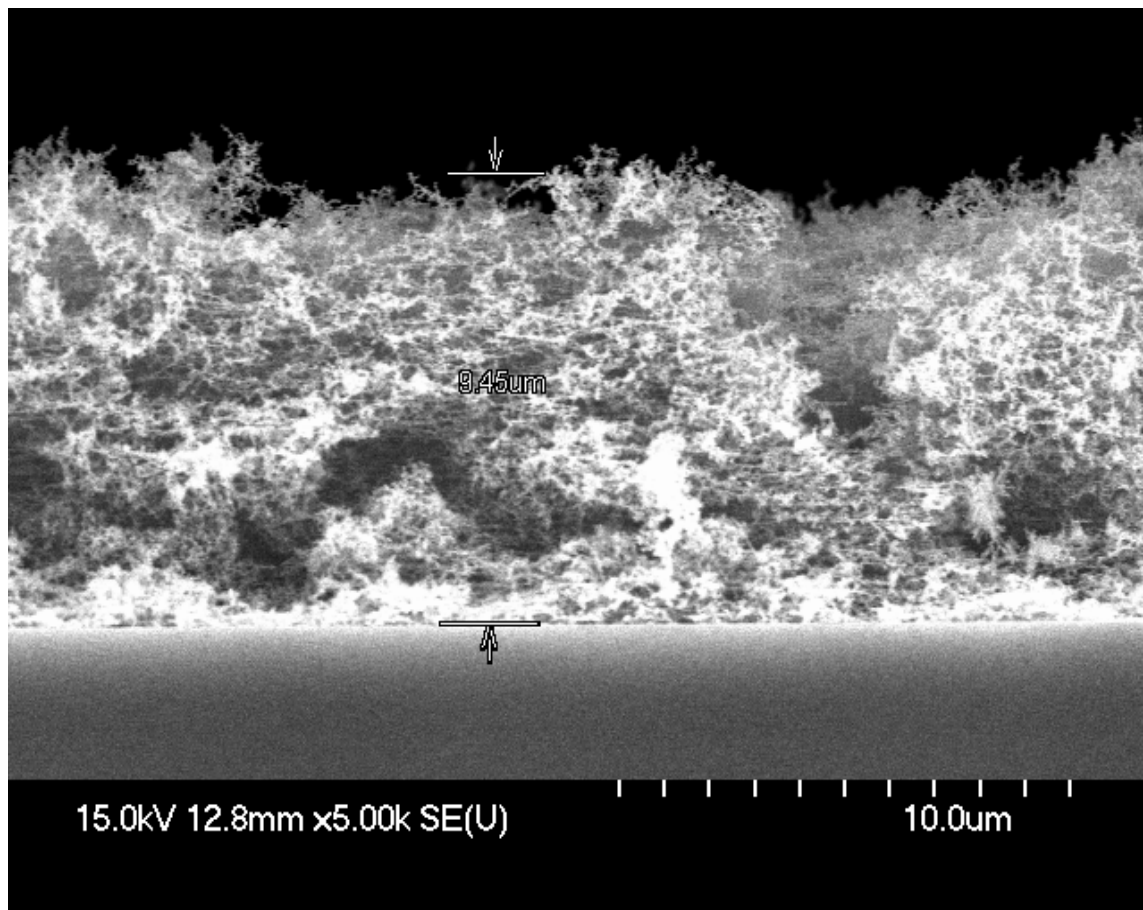


Figure 4.4 SEM image of the film thickness of N-doped  $\text{TiO}_2$  deposited on a glass substrate via a plate type APPENS reactor. The electric field strength was 19.2 kV/cm and the deposition time was 2 hrs.

## 4.2. PHOTOCATALYSIS STUDY OF N-DOPED TiO<sub>2</sub>

### 4.2.1. Photocatalytic activity of N-doped TiO<sub>2</sub> in a batch reactor

The extent of IPA photocatalysis to form acetone vapors was tested in a batch-type reactor exposed under both 10 W of UV (Figure 4.5a) and visible light (Figure 4.5b) illumination. The intensities of illumination in the reactor were 3.78 mW/cm<sup>2</sup> for UV light source and 4.81 mW/cm<sup>2</sup> for visible light source, respectively. One can observe from Figure 4.5a that near complete removals of IPA was achieved in about 20 min by both bare TiO<sub>2</sub> and N-doped TiO<sub>2</sub>. The peak concentrations of acetone were observed at around 8 min before the complete destruction of IPA and the acetone concentrations gradually approached zero at around 30 minutes.

On the other hand, as observed in Figure 4.5b the IPA and acetone removal rates were much slower under visible light irradiation when compared to the UV light irradiation. For test with N-doped TiO<sub>2</sub>, near complete destruction of IPA was achieved at around 50 min. The formation of acetone also reached its peak concentration at the same time and then the acetone concentration started to decay. While for test with bare TiO<sub>2</sub>, the IPA oxidation was still underway even after 80 min of irradiation.

In comparison with Figures 4.5a and 4.5b, one can see that under UV-irradiation where acetone could be oxidized to CO<sub>2</sub> even though the IPA destruction was not complete. But this was not the case under visible light irradiation; the destruction of acetone would occur only after the IPA was completely oxidized. Thus the visible light photocatalysts may be good for organics degradation but

they may require much longer time.

Even though the bare anatase  $\text{TiO}_2$  showed less photocatalytic activity than the N-doped  $\text{TiO}_2$  in the visible light source, it was still photocatalytic effective in the visible light range. This may be different from typical understanding that bare anatase  $\text{TiO}_2$  should be non-effective in the visible light range. But since photocatalytic tests with 364.2 nm UV lamp at the intensity of  $0.43 \text{ mW/cm}^2$  showed negligible photo-activity, it was not due to the minor UV peak ( $0.35 \text{ mW/cm}^2$  at 364 nm) of the visible light lamp for this photo-activity. Hence it could be attributed to the trapped electrons that enhance the photocatalytic activity of the bare  $\text{TiO}_2$  in the visible light (Nakamura et al., 2000). This phenomenon was also observed by Asahi et al. (2001) and Nosaka et al. (2005) which used color filters to filter out the UV light source and conducted bare anatase  $\text{TiO}_2$  for photocatalytic tests under visible light range. They still found some photo-activity of the bare anatase  $\text{TiO}_2$  in the visible light range.

In order to study the visible-light induced photocatalysis of odorous VOCs with another representative molecular structure (i.e., aromatic ring), the photocatalytic removals of toluene vapors via the N-doped and bare  $\text{TiO}_2$  in a batch reactor were also tested under both UV and visible light illumination and the results are shown in Figure 4.6. One can see that the N-doped  $\text{TiO}_2$  had higher activities than bare  $\text{TiO}_2$  under both UV and visible light sources. But at an initial time of less than 10 min, the removal rates of toluene were almost the same using the same photocatalyst under the same light intensity and were almost independent of the light source. After 10 min of

reaction time, the difference in the toluene removals between UV and visible light sources increased.

The toluene removal rates under visible light source were gradually retarded for both N-doped TiO<sub>2</sub> and bare TiO<sub>2</sub>. This might be caused by the formation of intermediate species such as benzoic acid, benzyl alcohol and benzaldehyde during the decomposition of toluene vapors. Such intermediate products which strongly adsorbed were less reactive on the catalysts surface and led to deactivation of the catalyst (d'Hennezel et al., 1998).

#### 4.2.2. Photocatalytic removals of NO by N-doped TiO<sub>2</sub> under UV and visible light irradiation

The NO is oxidized to NO<sub>2</sub> or NO<sub>3</sub><sup>-</sup> by the active oxygen species in the photocatalytic reaction (Sano et al., 2004). The removal of NO photocatalytic decomposition was tested in a continuous flow reactor with a residence time of 33.3 sec.

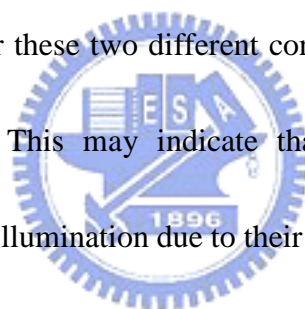
Figure 4.7 shows the concentrations of NO as well as NO<sub>2</sub> formed under illumination of visible light at NO inlet concentration of 16.7 ppm. The removal rate of NO is 1.61 μmol/hr, and the removal rate of NO<sub>x</sub> (NO + NO<sub>2</sub>) is 0.28 μmol/hr. The selective ratio of NO<sub>2</sub> is 82.6% as calculated from the following equation:

$$\text{Selective ratio} = \frac{[NO_2]_r - [NO_2]_i}{[NO]_i - [NO]_r} \times 100\% \quad (10)$$

The result showed that NO was mainly oxidized to NO<sub>2</sub> by visible light induced photocatalysis. The removal of NO was also tested under UV light illumination. The results are shown in Figures 4.8 and 4.9 at NO inlet concentrations of 17.4 and 10 ppm, respectively. One can observe in Figure

4.8 that the NO concentration decreased after light-on, and then gradually increased with time when NO inlet concentration was 17.4 ppm. But this phenomenon is not observed for NO inlet concentration of 10 ppm (Figure 4.9). This may indicate that more NO had been transformed to  $\text{NO}_3^-$  under relatively higher NO inlet concentration and this leads to deactivation of photocatalyst.

Figure 4.10 shows the removal rates of NO and  $\text{NO}_x$  at different inlet NO concentrations under UV light illumination. The removal rates of NO at inlet concentrations of 17.4 and 10 ppm are 4.92 and 3.22  $\mu\text{mol/hr}$ , respectively. And the removal rate of  $\text{NO}_x$  for NO inlet concentrations of 17.4 and 10 ppm are 3.81 and 2.37  $\mu\text{mol/hr}$ , respectively. Similar values of  $\text{NO}_2$  selective ratios are observed to be 6.31% and 6.83% for these two different concentration tests. They are much lower than that under visible light test. This may indicate that large amount of NO was mainly transformed to  $\text{NO}_3^-$  under UV light illumination due to their higher oxidative activity.



#### 4.2.3. Comparison of N-doped $\text{TiO}_2$ photocatalysis with commercial photocatalysts

The extent of decomposition of toluene vapor in a continuous-flow reactor with a residence time of 2.35 mins was evaluated to explore other application fields such as air cleaners. The comparison results of photocatalytic activity between the N-doped  $\text{TiO}_2$  produced in this study and the commercial photocatalysts of P25 and ST01 are shown in Figure 4.11. One can see that the toluene removal efficiency for N-doped  $\text{TiO}_2$  gradually increased with the time in the continuous flow reactor, and it then reached a plateau of around  $7.5\% \pm 0.5\%$ . On the other hand, the toluene removal efficiencies of both ST01 and P25 were less than that of the N-doped  $\text{TiO}_2$ . Although the toluene

removal efficiency of ST01 was slightly higher than that of P25, the difference in the removal efficiency was within 2%. With the relative reactivity of P25 photocatalyst (0.125  $\mu\text{mole/hr}$ ), defined by the accumulated amount of toluene removal over 60 mins of operation, as the reference base (relative reactivity = 1), it was calculated that the photoactivity of ST01 photocatalyst was approximately 3.2 times higher than that of P25 photocatalyst. The relative activity for the N-doped photocatalyst prepared in this study, in comparison, was notably greater than both commercial photocatalysts, with reactivity of 11.2 and 3.5 times higher than those of P25 and ST01 photocatalysts, respectively.

Few studies literature data have compared the visible-light induced photocatalytic activity of the N-doped  $\text{TiO}_2$  with those of the commercial photocatalysts. Li et al. (2005a, 2005b) prepared the N-doped and N-F-codoped  $\text{TiO}_2$  photocatalysts via spray pyrolysis and demonstrated that the photocatalytic activities of N-doped and N-F-codoped  $\text{TiO}_2$  were about 2 and 7 times, respectively, higher than that of the P25 photocatalyst in terms of the initial removal rate of acetaldehyde using a 150 W Xe lamp visible light source with 420 nm cut filter. Chen et al. (2005) prepared nanocolloid N-doped photocatalysts via a liquid phase method and found that the photocatalytic activity of the nanocolloid N-doped photocatalyst was 7 times higher than that of the P25 photocatalyst in terms of the methylene blue decomposition with a 540 nm visible light source. Our result on comparing the visible light-driven photocatalytic activity of the N-doped photocatalyst and the commercial P25 was qualitatively similar to those by Li et al. (2005b) and Chen et al. (2005) prepared via other

processes. In addition, the N 1s spectra of N-doped TiO<sub>2</sub> reported in this study was also very similar to those prepared by Chen et al. (2005), both exhibiting peaks at around 400-402 eV.

The Kubelka-Munk absorption spectra (Francisco et al., 2000) of N-doped TiO<sub>2</sub>, ST01 and P25 were shown in Figure 4.12. The UV-visible spectra of N-doped TiO<sub>2</sub>, ST01 and P25 were consistent with their toluene removal efficiency. As observed that the N-doped TiO<sub>2</sub> prepared in this study has a clear red shift into the visible light absorption range, with two absorption edges at around 400 and 520 nm. On the other hand, there was only one absorption edge at around 395 and 405 nm, respectively, for the ST01 and the P25 photocatalysts. Also, although the wavelength of the absorption edge of P25 was slightly larger than that of ST01, their removal efficiencies were very similar (<2%) in the visible light range as demonstrated in Figure 4.11. This might be due to that the photocatalytic activity was also influenced by many other factors such as crystalline size, surface and bulk defects, porosity, surface area, impurities and active sites such as Ti<sup>3+</sup> and OH sites.

#### 4.2.4. Summary

Effective removal of odorous VOCs in both batch and continuous flow photocatalytic reactors under visible and UV light sources were demonstrated as well. The results showed that the N-doped TiO<sub>2</sub> photocatalyst was more effective in removing IPA under both UV and visible light sources than the un-doped TiO<sub>2</sub> photocatalyst. Furthermore, the N-doped TiO<sub>2</sub> photocatalyst was superior in toluene removal than the commercial ST01 and P25 TiO<sub>2</sub> photocatalysts under visible light



irradiation. Considering that UV light accounts for only 3~5 % of the solar light intensity, and that indoor lighting is predominantly in the visible light range, the results presented in this study strongly suggest that the N-doped TiO<sub>2</sub> photocatalysts prepared via the APPENS process has a potential application in the arena of indoor and outdoor air pollution control.



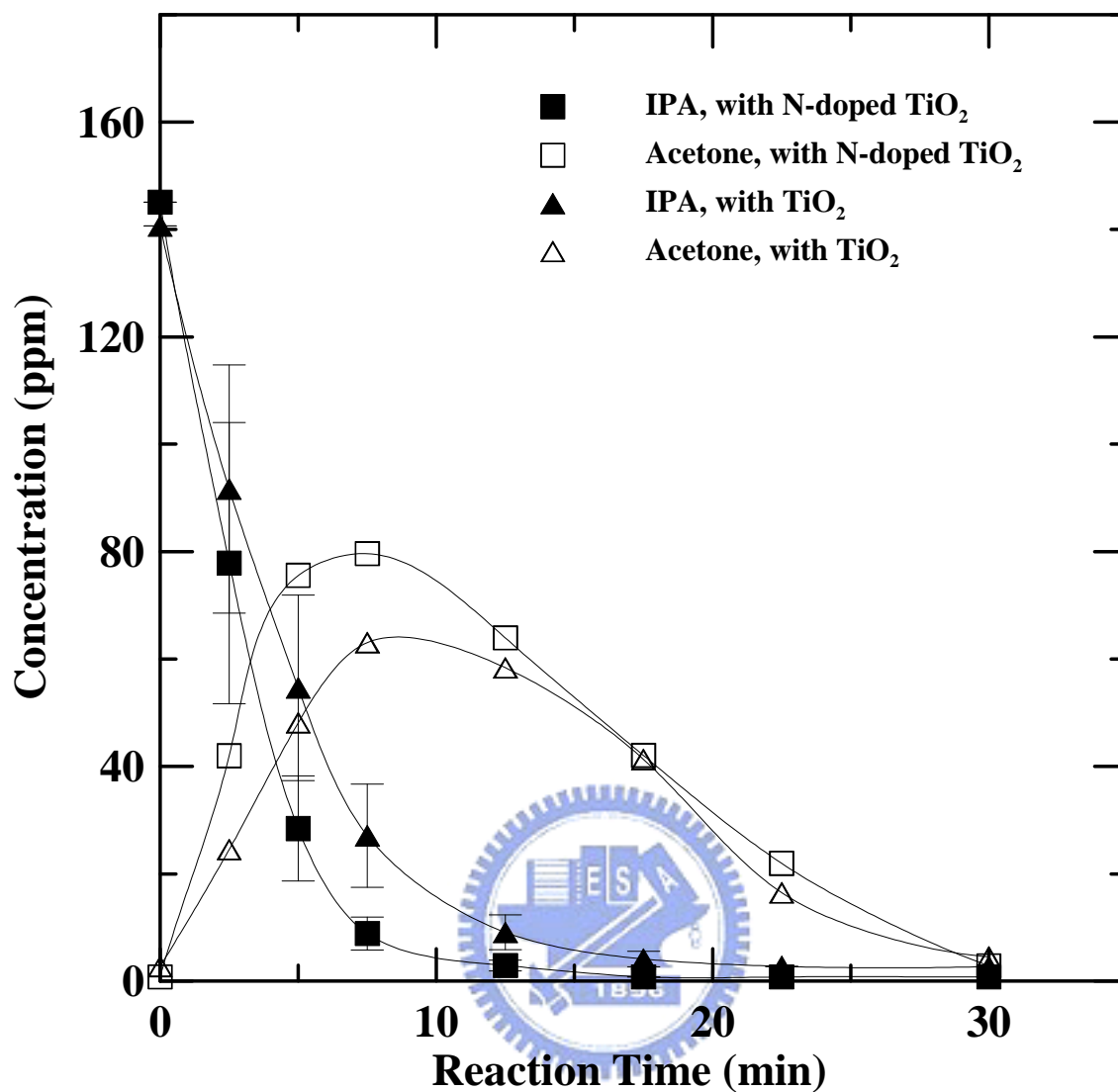


**Figure 4.5a** The decomposition of IPA and the formation of acetone in a batch photocatalytic reactor under UV light (10 W, peak at 364.2 nm). Error bars indicated the error range of repeated experimental data.

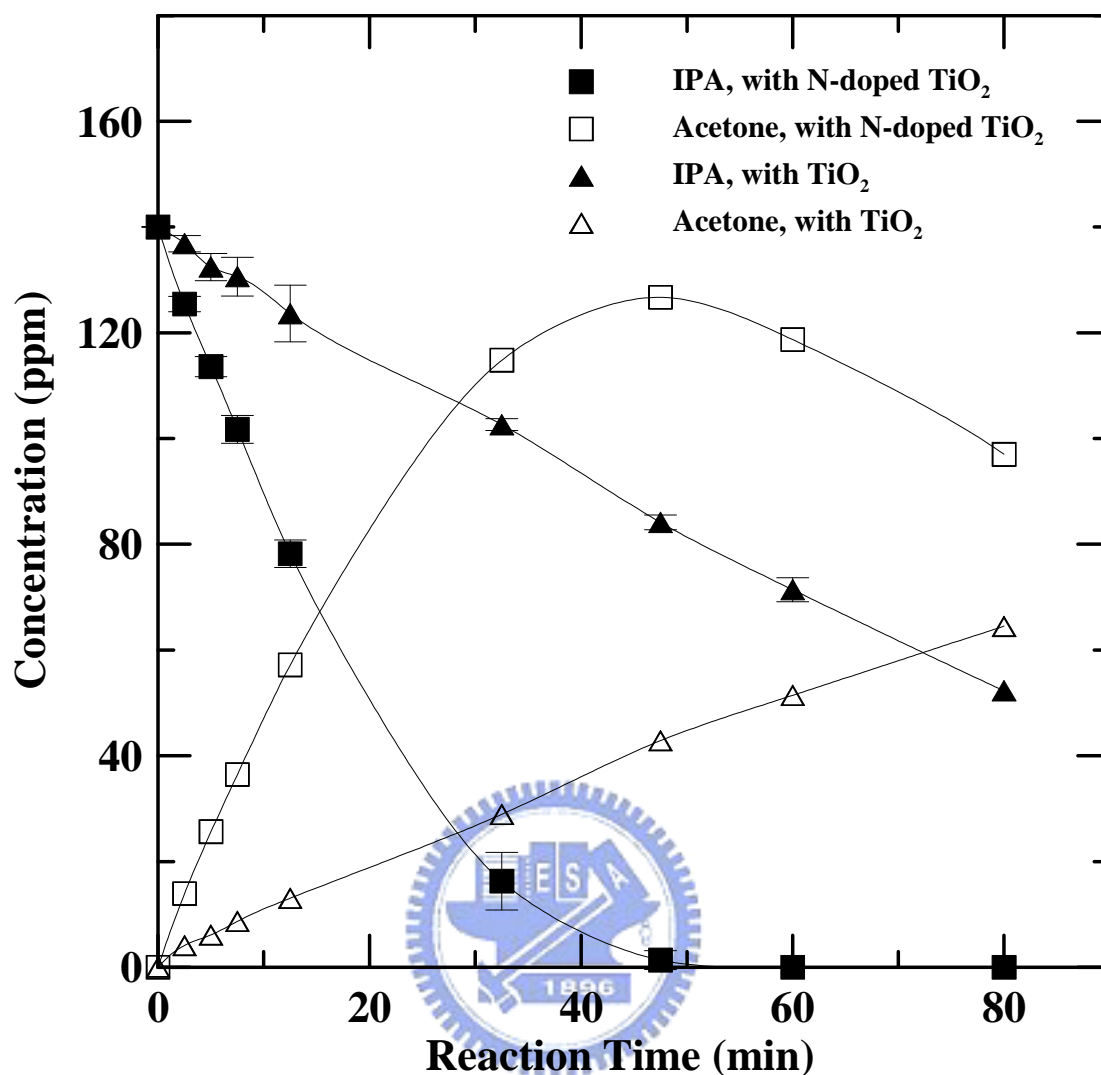


**Figure 4.5b** The decomposition of IPA and the formation of acetone in a batch photocatalytic reactor under visible light (10 W, peaks at 435, 488, 545, 587 and 611 nm). Error bars indicated the error range of repeated experimental data.

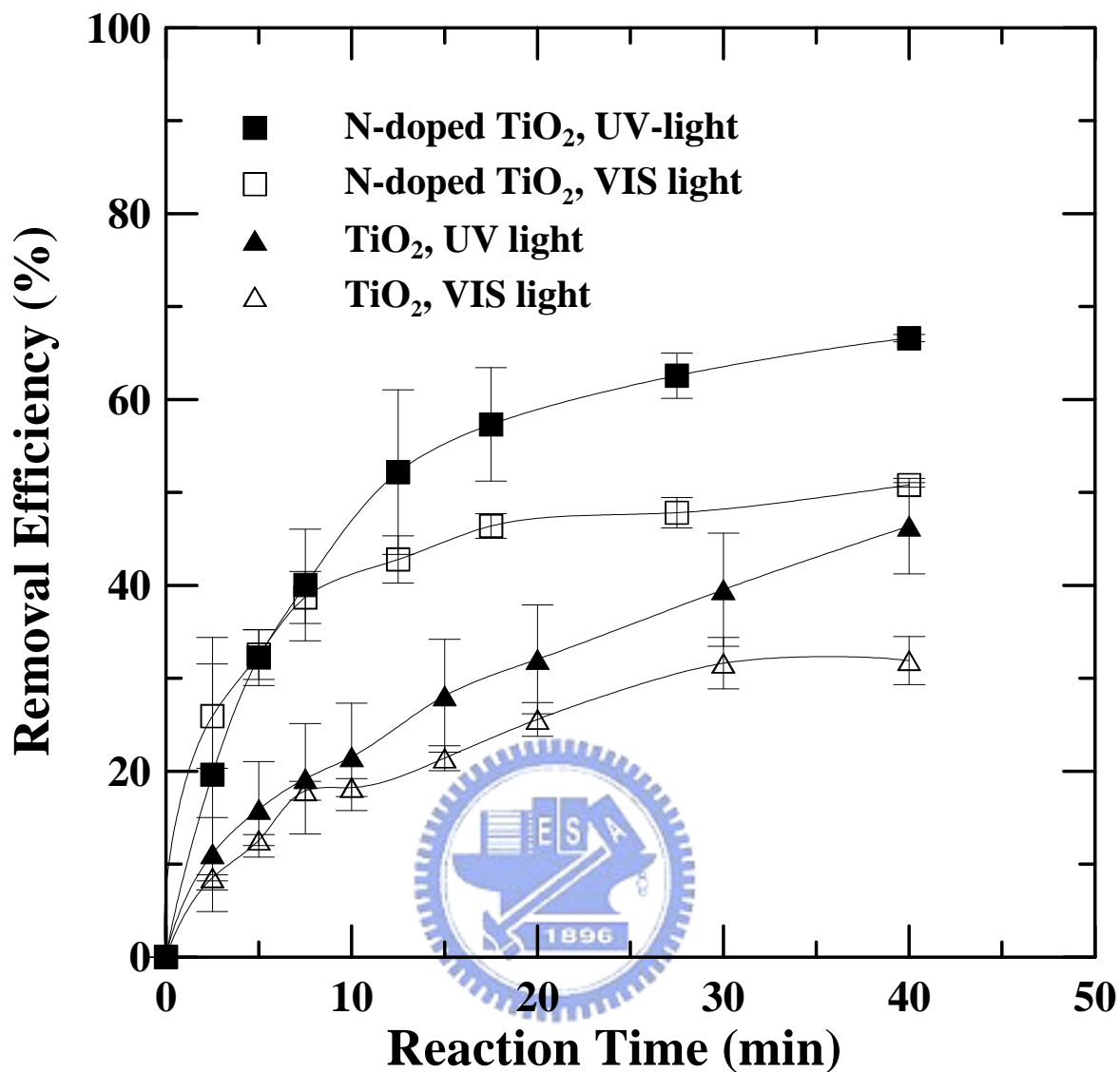


Figure 4.6 The removal efficiency of toluene as a function of time in a batch photocatalytic reactor under UV (10 W, peak at 364.2 nm) and visible light (10 W, peaks at 435, 488, 545, 587 and 611 nm) sources. Error bars indicated the error range of repeated experimental data.

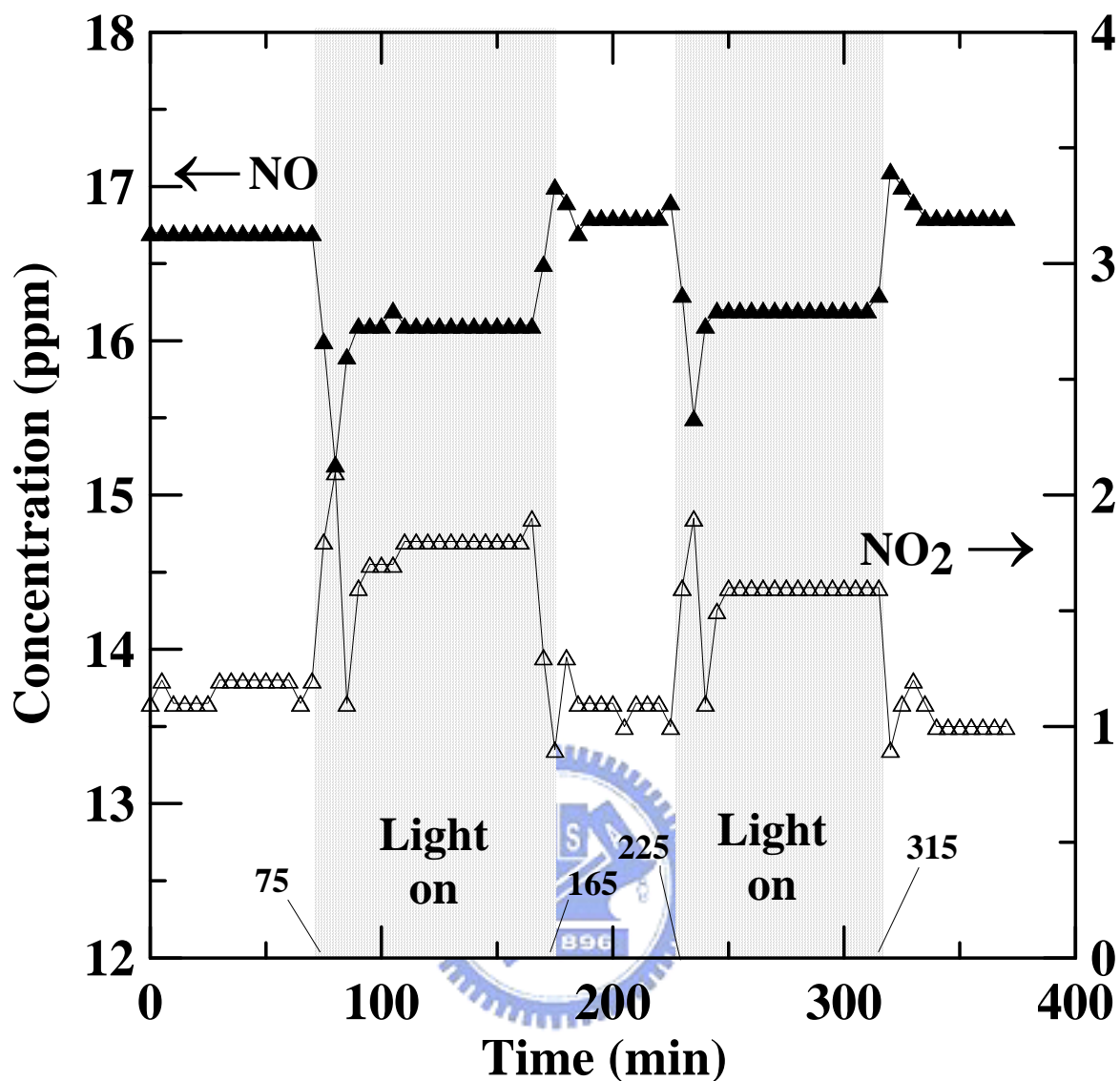


Figure 4.7 Concentration variation of NO and NO<sub>2</sub> by photo-catalytic reaction under visible light irradiation. The inlet concentrations of NO and NO<sub>2</sub> was 16.7 ppm and 1.1 ppm, respectively. The carrier gas composition was 20%N<sub>2</sub>+80%O<sub>2</sub>.

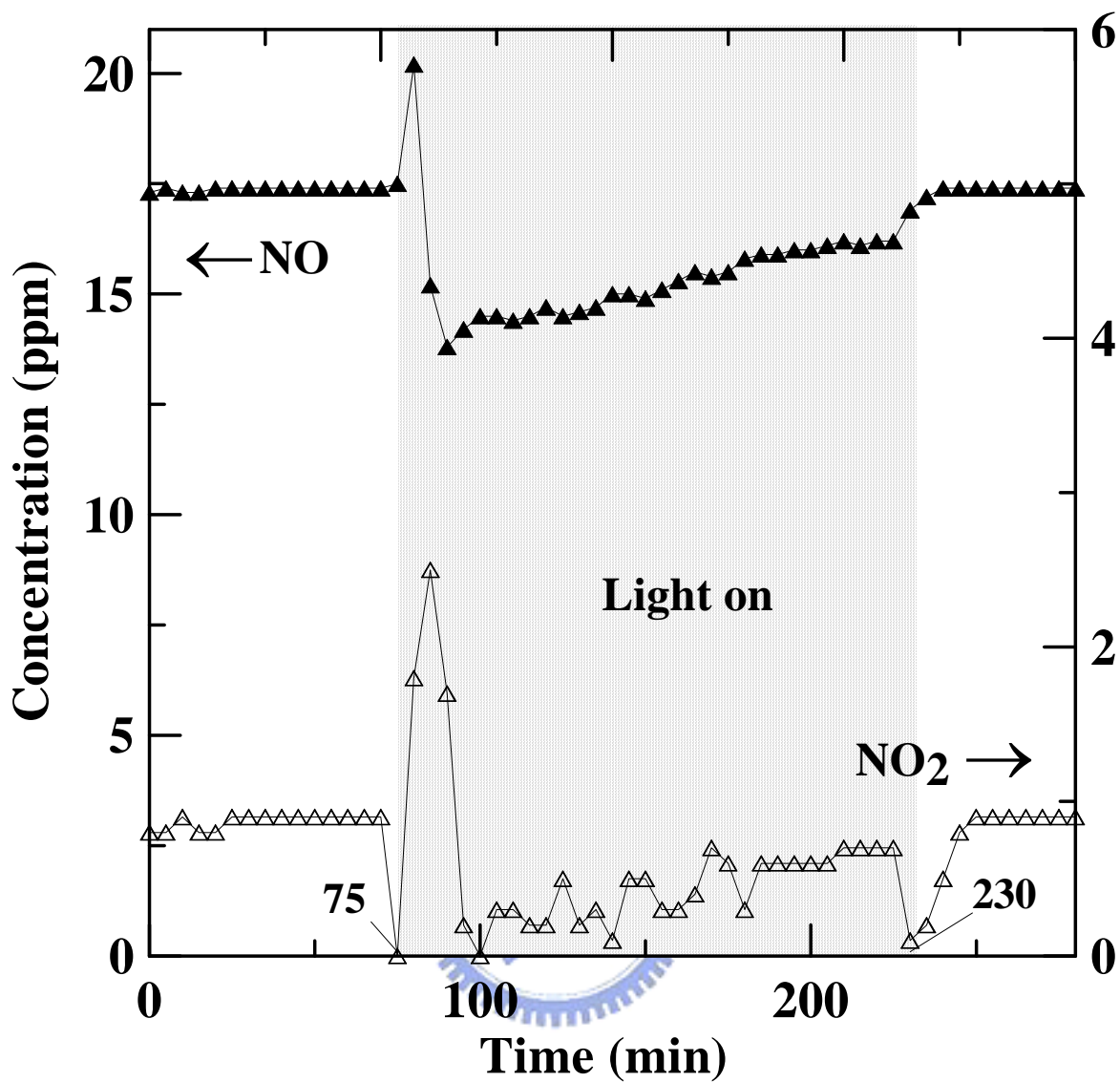
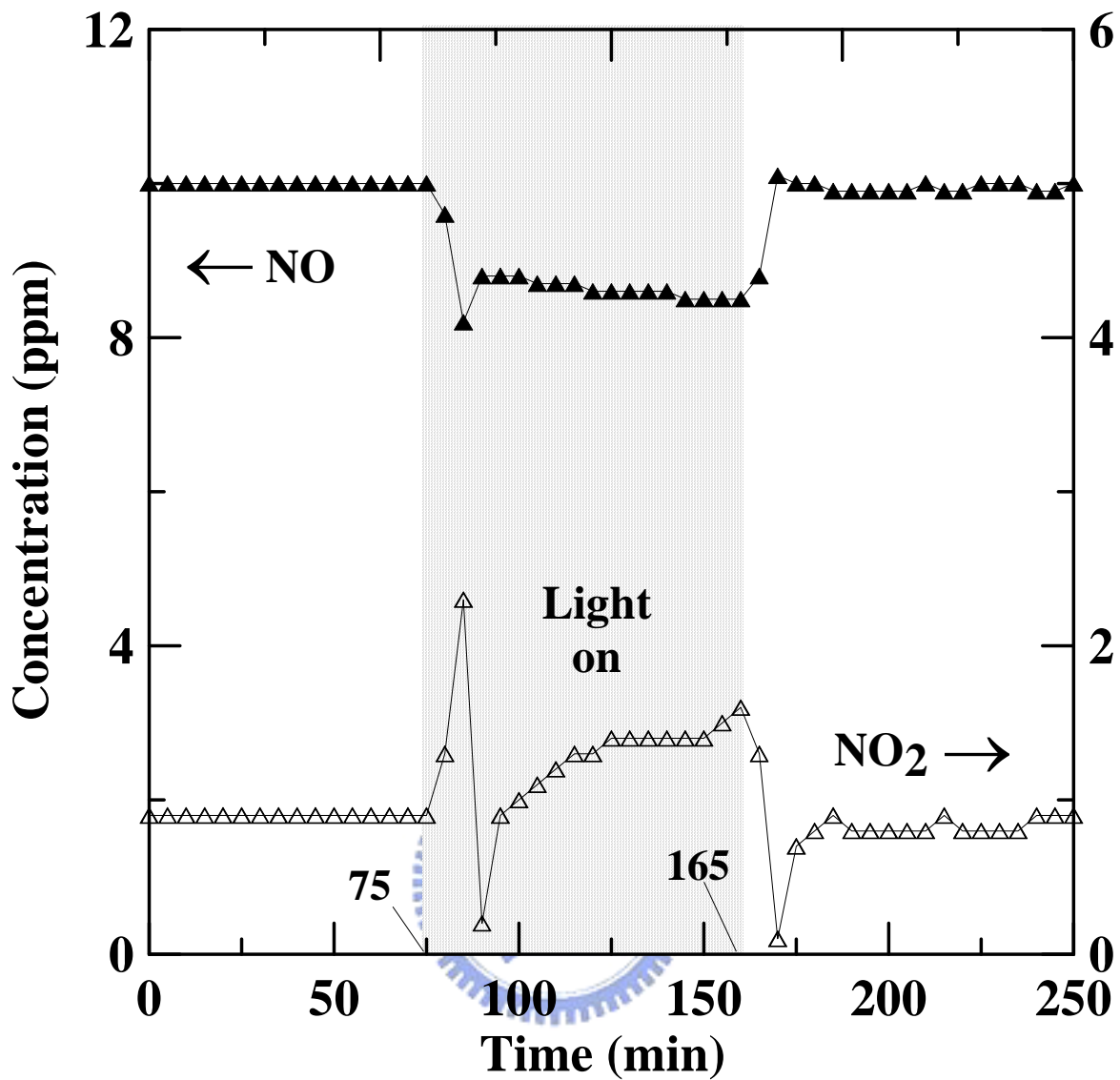


Figure 4.8 Concentration variations of NO and NO<sub>2</sub> by photo-catalytic reaction under UV light irradiation. The inlet concentrations of NO and NO<sub>2</sub> was 17.4 ppm and 0.9 ppm, respectively. The carrier gas composition was 20%N<sub>2</sub>+80%O<sub>2</sub>.



**Figure 4.9** Concentration variations of NO and NO<sub>2</sub> by photo-catalytic reaction under UV light irradiation. The inlet concentrations of NO and NO<sub>2</sub> was 10 ppm and 0.9 ppm, respectively. The carrier gas composition was 20%N<sub>2</sub>+80%O<sub>2</sub>.

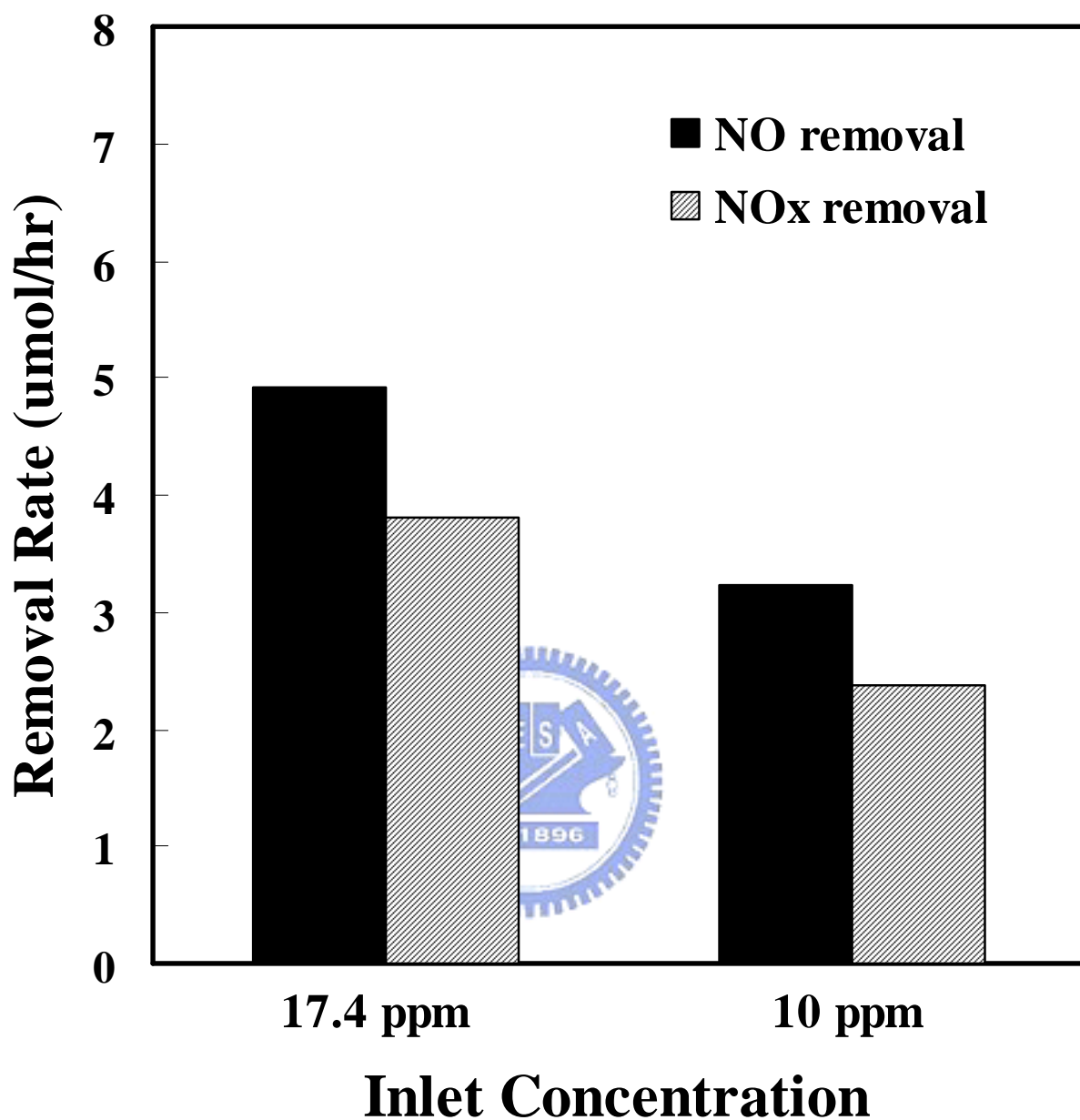


Figure 4.10 Removal rates of NO and NO<sub>x</sub> at different inlet NO concentrations under UV light irradiation



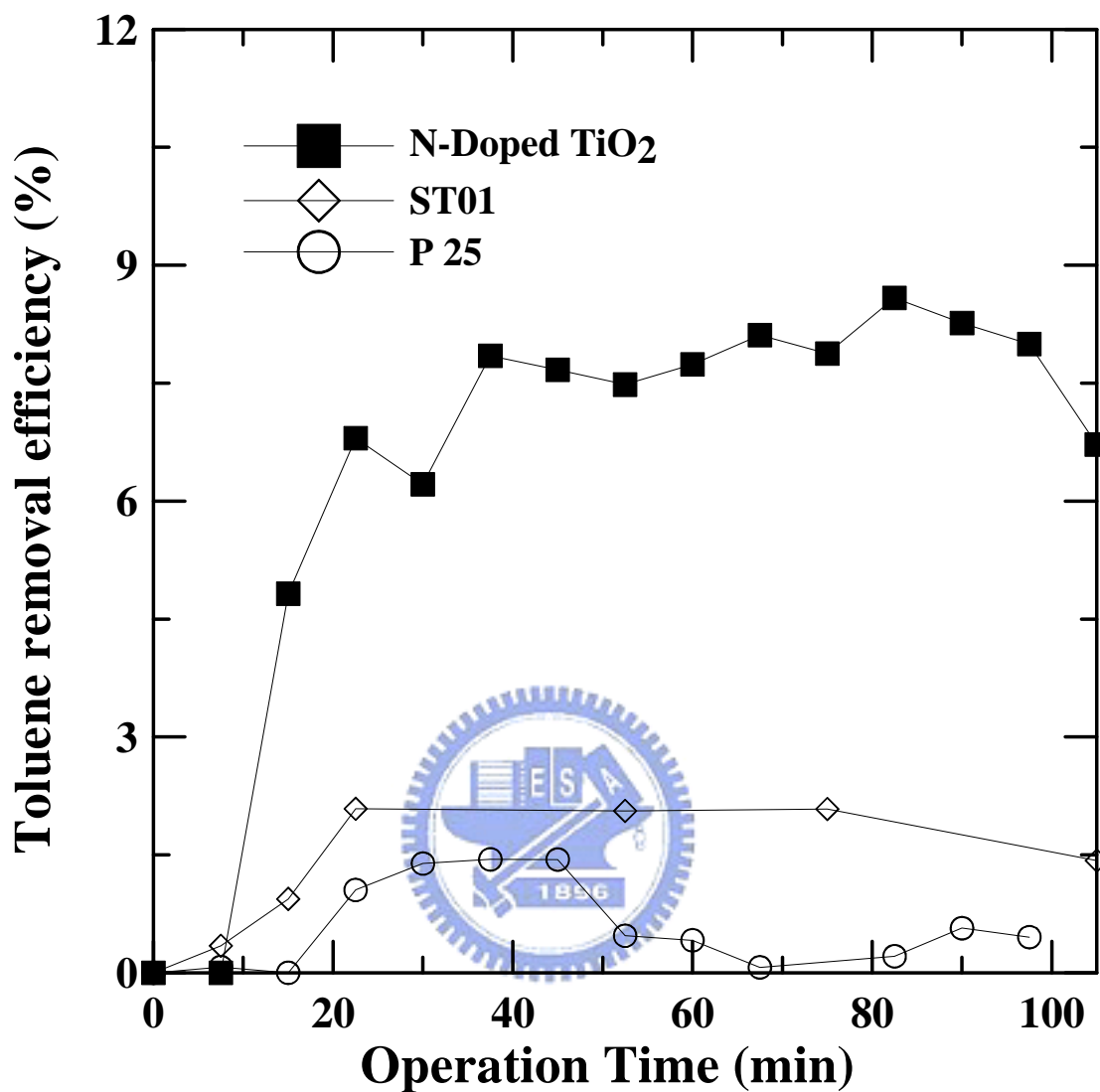


Figure. 4.11 Comparison of the toluene decomposition between P25, ST01 and the N-doped TiO<sub>2</sub> (TiO<sub>2-x</sub>N<sub>x</sub>) photocatalysts tested in a continuous flow reactor under visible light (10W) illumination. The residence time in the reactor was 2.35 minutes.

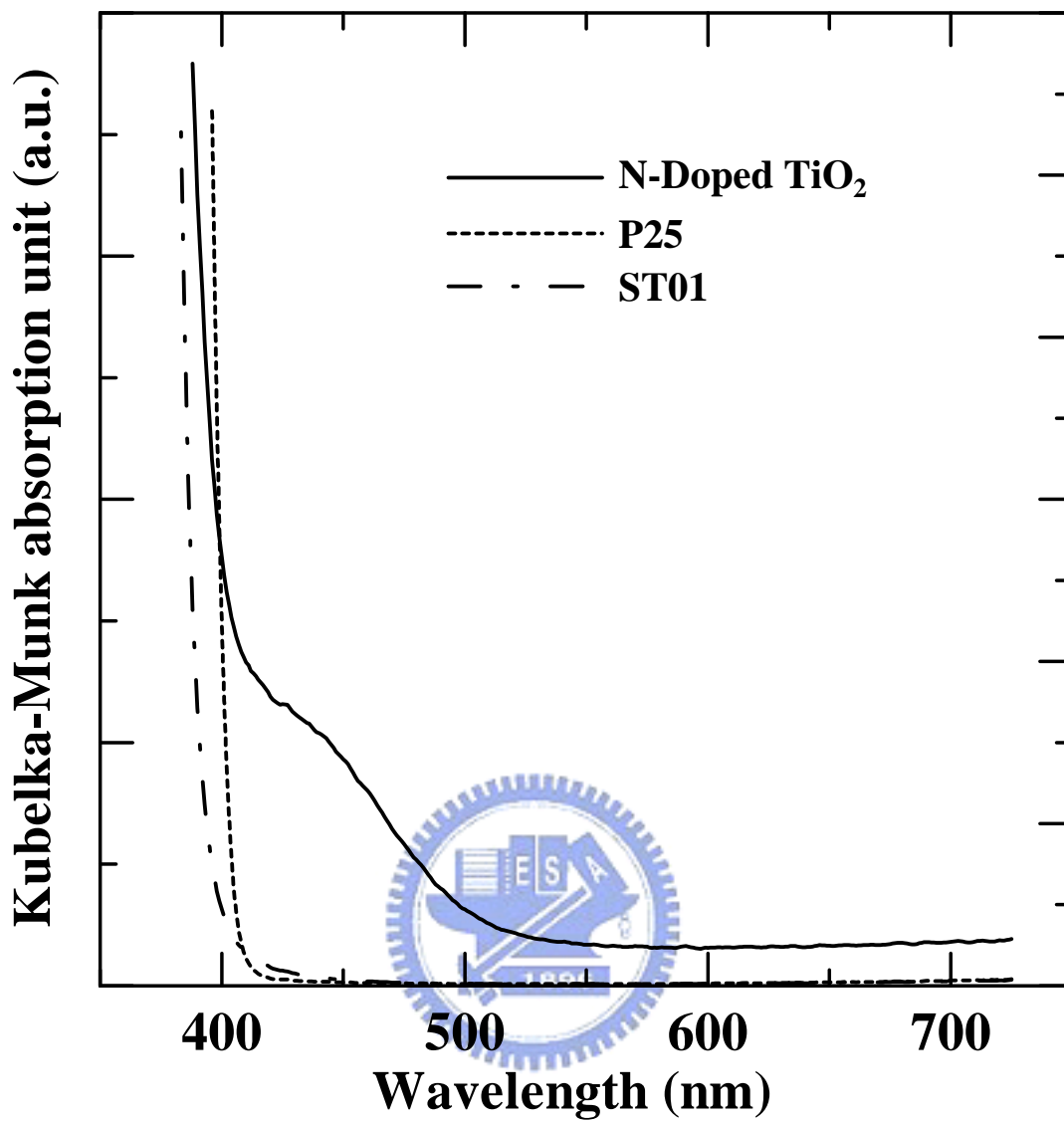


Figure 4.12 Kubelka-Munk absorption spectra of the commercial photocatalysts (P25 and ST01) and the N-doped TiO<sub>2</sub> (TiO<sub>2-x</sub>N<sub>x</sub>) photocatalyst prepared in this study.

### 4.3. EFFECT OF N-DOPING STATUS ON PHOTOCATALYTIC ACTIVITY OF TiO<sub>2</sub>

#### 4.3.1. IPA Conversion

The photocatalytic activities of SYN1 to SYN4 samples obtained under different plasma and annealing gases were examined via the IPA conversion, and the results are shown in Figures 4.13 and 4.14, respectively, with visible and UV light sources. It was observed that all types of TiO<sub>2</sub> particles including pure TiO<sub>2</sub> photocatalyst produced via SYN3 have some IPA conversion under visible light (Figure 4.13).

The photocatalytic activities in terms of IPA conversion are follow the order of SYN1 > SYN2 > SYN3 > SYN4 under both visible and UV light sources as observed in Figures 4.13 and 4.14. The difference in the IPA conversion is especially significant for the visible light test results as shown in Figure 4.13. A nearly complete removal of IPA can be achieved after around 60 mins for SYN1, but the IPA conversion was only around 40% for SYN4. In addition, the SYN4 photocatalyst has less IPA conversion than that of the pure TiO<sub>2</sub> particles (SYN3). The observations indicate that the N-doped TiO<sub>2</sub> photocatalyst may not necessarily have a higher photocatalytic activity under visible light source. Because the photocatalytic activity of TiO<sub>2</sub> particles may be affected by many factors such as particles size, crystal phase, UV-visible light absorption spectra, and the N-doped status, these factors are discussed in the followings.

#### 4.3.2. Crystallite and particle sizes

Figures 4.15(a) ~ 4.15(d) show the SEM images are shown for SYN1~SYN4 photocatalysts. It is observed that the photocatalytic particles synthesized under 100% N<sub>2</sub> plasma atmospheric (SYN1 and SYN2) were larger than those under 20% O<sub>2</sub> (SYN 3) and 10% N<sub>2</sub>+ 10% O<sub>2</sub> + 80% Ar (SYN4) plasma atmospheric. The particle sizes of SYN1 and SYN2 were around 50 nm as roughly estimated from the SEM images. And they were around 25 nm for SYN3 and SYN4. When calculating the crystallite size of particles (D, nm) from the Scherrer equation using the XRPD measurement data, however, the crystallite sizes of SYN1 ~ SYN4 were around 22.0±1.2 nm as listed in Table 4.2. Therefore, it can be conclude that the primary crystallite particle size of SYN1 and SYN2 are the similar to those of SYN3 and SYN4. But the strong agglomeration force for SYN1 and SYN2 particles led to the formation of secondary particles which may compose of more than two crystallites.

Several studies have shown that optimal size range of TiO<sub>2</sub> for achieving better photocatalysis were about 25~30 nm toward organic compounds removal in aqueous solution (Amquist and Biswas, 2002), while it was 13 nm in the gas phase destruction of acetone to form CO<sub>2</sub> (Ihara et al., 2003). Therefore if one considers the effect of particle size only, then SYN3 and SYN4 particles with an optimal size of around 25 nm should have better activities than SYN1 and SYN2 which have larger secondary sizes of around 50 nm. However this was not happened in this study. Hence one can conclude that the secondary particle size effect on the photocatalytic activity is not an

influential factor on the photoactivity in this study. This could be due to that the crystallite sizes of SYN1 to SYN4 are about the same at around 22 nm as calculated by the Scherrer equation.

#### 4.3.3. Crystal phase

The crystal phase of photocatalytic particles was determined with the XRPD pattern shown in Figure 4.16. The XRPD peaks at around 25.3°, 38.6°, 48.0°, 55.1° and 62.7° corresponding to anatase phase are observed for all synthesized nanoparticles, with the main significant peak at around 25.3°.

A minor peak at 27.5° (corresponding to rutile crystal) appeared for the product particles of SYN1 and SYN2. The SYN1 and SYN2 photocatalysts were both obtained under the same plasma conditions and same annealing temperature at 500°C. The phase transformation of nanocrystalline from anatase to rutile should appear at temperature higher than 600°C (Zhang and Banfield, 2005). However, it is also possible to occur at low temperature for N-doped photocatalysts (Maeda and Watanabe, 2006). But the ratios of signal to noise (S/N) of rutile phase for SYN1 and SYN2 photocatalyst are 1.15 and 1.29, respectively, which may be within the error range of detection as compared to the anatase phase. Thus it is concluded that the crystal phase should have minimal effect on the photocatalytic activity.

#### 4.3.4. UV-visible spectra

Figure 4.17 shows the Kubelka-Munk absorption unit spectra of the synthesized photocatalysts obtained by different processes of SYN 1 to SYN 4. The absorption edge of around 400 nm is

assigned to the pure  $\text{TiO}_2$  and appeared for all processes. On the other hand, a second absorption edge at around 520 nm appeared only for SYN1 and SYN2 and it should be attributed to the presence of N-doped ions. Although SYN4 was synthesized under  $\text{N}_2/\text{O}_2$  gas plasma, there is no obvious absorption edge in the visible light region. However, although SYN4 photocatalyst did not cause obvious red shift of the absorption edge in the UV-Vis absorption spectra, it still showed visible light photocatalytic effect as shown previously in Figure 4.13 due to the surface absorption or the oxygen vacancy (Livraghi et al., 2006; Huang et al., 2007).

#### 4.3.5. Core level binding energy

To minimize the interference of other factors such as crystallite size and particle size of  $\text{TiO}_2$  as well as its crystal phase on the photocatalytic activity, the photocatalysts were prepared under the same operating conditions in the APPENS reactor as shown previously. Thus the remaining important factor on the photocatalytic activity is the N-doping status of the photocatalysts.

The XPS spectra of Ti 2p, N 1s and O 1s for the photocatalytic particles synthesized in this study are shown in Figure 4.18. The core level binding energies of Ti 2p under different synthesized photocatalysts are around 457.0~459.0 eV for Ti  $2p_{3/2}$  and 463.0~464.0 eV for Ti  $2p_{1/2}$ . It is noted that the peaks at 458.0 eV for Ti  $2p_{3/2}$  and 463.7 eV for Ti  $2p_{1/2}$  are assigned to be  $\text{TiO}_2$ , which can be clearly seen for SYN 3 photocatalyst (Table 2.3). On the other hand, the presence of TiN (Ti  $2p_{3/2}$ , 455.2~456.0 eV) and  $\text{TiO}_{2-x}\text{N}_x$  (Ti  $2p_{3/2}$ , 456.0~459.0 eV) tends to shift the  $\text{TiO}_2$  peaks to

lower binding energy. It was observed that SYN1 photocatalyst has the most significant shift towards lower binding energy of 457.2 eV at Ti 2p<sub>3/2</sub>.

The most significant peak of N 1s (right spectra in Figure 4.18) for SYN1 photocatalyst is observed at around 402.9 eV (N(III)), while the most significant N 1s peaks for SYN2 and SYN4 are both located at around 398.5~400.8 eV (N(II)). On the other hand, there is no obvious N 1s peak for SYN3 photocatalyst since it was produced without the presence of nitrogen source.

The major O 1s peaks (left spectra in Figure 4.18) for SYN1 and SYN2 photocatalysts are both observed at around 529.7±0.3 eV (O(I)), while the major O 1s peaks for SYN3 and SYN4 photocatalyst are both located at around 531.5±0.5 eV (O(II)). One can see from Table 2.3. that the presence of O(I) peaks indicates that O atoms are bonded to metals such as Ti, while the O(II) and O(III) peaks reveals that the O atoms could be bonded to N or other atoms such as C and H, or simply as adsorbed O<sub>2</sub>. Because there was no nitrogen source in the SYN3 process, therefore for SYN3 photocatalyst the O atoms may be bonded as CO, substoichiometric oxide (TiO<sub>2-x</sub>) or appeared as adsorbed O<sub>2</sub>.

#### 4.3.6. N-doped status of the TiO<sub>2</sub> photocatalyst

The different N-doping structures in the TiO<sub>2</sub> particles can be seen more clearly by the cross comparison between N 1s and O 1s spectra as shown in Figure 4.19. The peaks of N(I) observed at around 395.8~397.8 eV indicates the possible presence of TiN. It may also indicate the presence of TiN<sub>x</sub>O<sub>y</sub> with the simultaneous appearance of O(II) at 531.0 eV (Guillot et al., 2002). Both the TiN

and  $\text{TiN}_x\text{O}_y$  peaks represent the N substitution for the O in  $\text{TiO}_2$  (Asahi et al., 2001; Maeda and Watanabe, 2006). And TiN bond was observed in SYN1, SYN2 and SYN4 photocatalysts.

The N(II) peaks located at the region of 398.8~401.2 eV indicates the possible presence of chemisorbed oxynitride with the simultaneous appearance of the O(II) peak at around 531.0~532.4 eV peak. The N(II) peak may be the Ti-(NO) structure (Sato et al., 2005; Chen et al., 2005; Gyorgy et al., 2003) or as impurities doped in the interstitial of  $\text{TiO}_2$  matrices (Maeda and Watanabe, 2006; Diwald., 2004). The above N-doped statuses are all denoted as Ti-(NO) in this study. And it was observed in SYN1, SYN2 and SYN4 photocatalysts.

The N(III) peaks located at about 402.0~403.0 eV correspond to the oxidized form of TiN into  $\text{O}_x\text{-Ti-N}_y$  as confirmed by the feature of O(II) peak at 531.9 eV (Chen et al., 2005; Chen and Burda, 2004; Esaka et al., 1997). The  $\text{O}_x\text{-Ti-N}_y$  bond was observed in SYN1, SYN2 and SYN4 photocatalysts. Finally, the N(IV) peak located at around 404.6 eV should be Ti-( $\text{NO}_2$ ) (Jill Eds., 1992; Lu et al., 2000; Rodriguez et al., 2000) with a cross comparison of the O(III) peak at 532.2 eV, it was appeared only for SYN4 photocatalyst.

Figure 4.19 also shows the percentage of total N relative to the Ti atomic ratio (denoted as  $N_{\text{total}}/\text{Ti}$  in Figure 4.19) as well as each type of N-doping relative to the total N-doping quantity ( $N/N_{\text{total}}$ ). One can see that the N-doped  $\text{TiO}_2$  obtained from SYN 2 has the highest  $N_{\text{total}}/\text{Ti}$  atomic ratio of 69%. This is much higher than SYN1 photocatalyst, which has  $N_{\text{total}}/\text{Ti}$  atomic ratio of only 24%. But the SYN1 photocatalysts still has higher photocatalytic activity than the SYN2



photocatalyst. Therefore one knows that the total quantity of nitrogen in the photocatalyst may not have a direct influence on the visible light photocatalysis. On the other hand, the N-doping status may have a deterministic effect on the photocatalytic activity.

The major type of N-doping for SYN1 is  $O_x-Ti-N_y$ , which accounts for 69.2% of the total N in the photocatalyst. There is also 21.2% of Ti-(NO) and only 9.6% of TiN observed for SYN 1 photocatalyst. On the other hand, Ti-(NO) is the most significant N bonding (70.2%) and TiN was the secondary bonding (22.8%) for SYN 2 photocatalyst. There is also a few percentage (7.0%) of  $O_x-Ti-N_y$  appeared in SYN2 photocatalyst. The N-doping status for SYN4 photocatalyst is very similar to that of SYN2, with the major peak as Ti-(NO) (76.7%) and minor peaks as  $O_x-Ti-N_y$  (8.6%) and TiN (6.2%). But the SYN4 photocatalyst has an additional peak of Ti-NO<sub>2</sub>. Besides, its TiN percentage is less than that of SYN2 photocatalyst (8.5%). It was also noted that the TiN located around 395~396 eV only appears for photocatalysts produced by nitrogen plasma process (SYN1& SYN2), while the TiN peak located at around 397 eV appears for SYN1, SYN2 and SYN4 photocatalysts.

By comparing the XPS results to the photoactivity results shown previously in Figure 4.13, one can suggest that Ti-N,  $O_x-Ti-N_y$  and Ti-(NO) doped TiO<sub>2</sub> photocatalysts have positive effects on the visible light photocatalysis, and thus the IPA removals efficiencies are higher with SYN1 and SYN2 photocatalysts. This result is similar to those of Sato et al. (2005), Yin et al. (2005) and Diwald et al. (2004), but opposite to that of Nosaka et al. (2005) The opposite result between these

studies are probably due to that N-induced localized state (Esaka et al., 1997; Jill Eds., 1992; Saha and Tompkins, 1992) causes the positive effect on the visible light photocatalysis as observed at Sato et al. (2005), Yin et al. (2005), Diwald et al. (2004) and in this study. But the photocatalyst prepared by Nosaka et al. (2005) could only absorb  $-(NO)$  on the catalyst surface and this resulted in a negative effect. However, it requires further studies to confirm this hypothesis.

The photocatalytic activity of  $O_X-Ti-N_Y$  may be superior to that of  $Ti-(NO)$  doped photocatalysts since  $O_X-Ti-N_Y$  is the major N-doping for SYN1 photocatalyst. This is in accordance with the studies of Chen et al. (2004; 2005) that  $O_X-Ti-N_Y$  is an effective doping. The results indicated that in addition to the widely accepted  $Ti-N$  bonding, both  $Ti-NO$  and  $O_X-Ti-N_Y$  type of N-doping  $TiO_2$  have positive effects on the visible light photocatalysis.

On the other hand, although SYN4 showed the presence of  $Ti-(NO)$  as major peak and  $O_X-Ti-N_Y$  and  $TiN$  as minor peaks, its photo-activity is much lower than those of the SYN1 and SYN2 photocatalysts and even worse than the pure anatase  $TiO_2$  made by SYN3. It may be distributed to the presence of  $Ti-(NO_2)$  doping as observed only for SYN4. Therefore one can suggest that  $Ti-(NO_2)$  doping tends have a negative effect on the visible light photocatalysis.

#### 4.3.7. Summary

N-doped  $TiO_2$  had been produced by APPENS process via different plasma and annealing gas compositions. The different binding energies of  $Ti\ 2p$ ,  $N\ 1s$  and  $O\ 1s$  obtained in this study via the XPS analysis had been grouped into several ranges as  $TiO_2$  and  $TiN$  at  $2p_{3/2}$  and  $2p_{1/2}$ ,  $N(I)\sim N(IV)$

for N 1s and O(I)~O(III) for O1s base on the literature data on N-doped TiO<sub>2</sub> photocatalysts. And the N-doping status of TiN, Ti-(NO), O<sub>X</sub>-Ti-N<sub>Y</sub> or Ti-(NO<sub>2</sub>) was confirmed by the cross comparison of chemical shift in the binding energies of N, Ti and O as shown in Table 4.3. It was found that Ti-(NO) and O<sub>X</sub>-Ti-N<sub>Y</sub> are the most significant structures of the N-doped TiO<sub>2</sub> for the N<sub>2</sub> plasma processes. But Ti-(NO<sub>2</sub>) may form under the presence of both O<sub>2</sub> and N<sub>2</sub> plasma gases. Results on the photocatalytic activities in terms of IPA conversion indicated that in addition to the widely accepted TiN doping, both Ti-(NO) and O<sub>X</sub>-Ti-N<sub>Y</sub> types of N-doping TiO<sub>2</sub> have positive effects, but the presence of Ti-(NO<sub>2</sub>) tends to have a negative effect on the visible light photocatalysis.



**Table 4.2 Crystallite sizes of SYN1~SYN4 photocatalytic particles. The crystallite sizes were calculated based on Scherrer equation with parameter values obtained from XRPD patterns (X-ray wavelength ( $\lambda$ ) was 0.154056 nm).**

Photocatalyst	Maximum Peak ( $2\theta$ )	FWHM ( $\beta$ )	Crystallite size (D, nm)
SYN1	25.23	0.00653	21.76
SYN2	25.28	0.00667	21.30
SYN3	25.38	0.00613	23.18
SYN4	25.36	0.00653	21.76

**Table 4.3 Plasma and annealing gas compositions and different N-doped status of TiO<sub>2</sub> photocatalysts.**

Photocatalysts	Plasma Gas	Anneal Gas	N-doping status
SYN1	100% N <sub>2</sub>	Air(20% O <sub>2</sub> + 80% N <sub>2</sub> )	TiN, TiN <sub>x</sub> O <sub>y</sub> , Ti-(NO), O <sub>x</sub> -Ti-N <sub>y</sub>
SYN2	100% N <sub>2</sub>	20% N <sub>2</sub> + 80% Ar	TiN, Ti-(NO), O <sub>x</sub> -Ti-N <sub>y</sub>
SYN3	20% O <sub>2</sub> + 80% Ar	20% O <sub>2</sub> + 80% Ar	--
SYN4	10% N <sub>2</sub> + 10% O <sub>2</sub> + 80% Ar	20% N <sub>2</sub> + 80% Ar	TiN, Ti-(NO), O <sub>x</sub> -Ti-N <sub>y</sub> , Ti-(NO) <sub>2</sub>

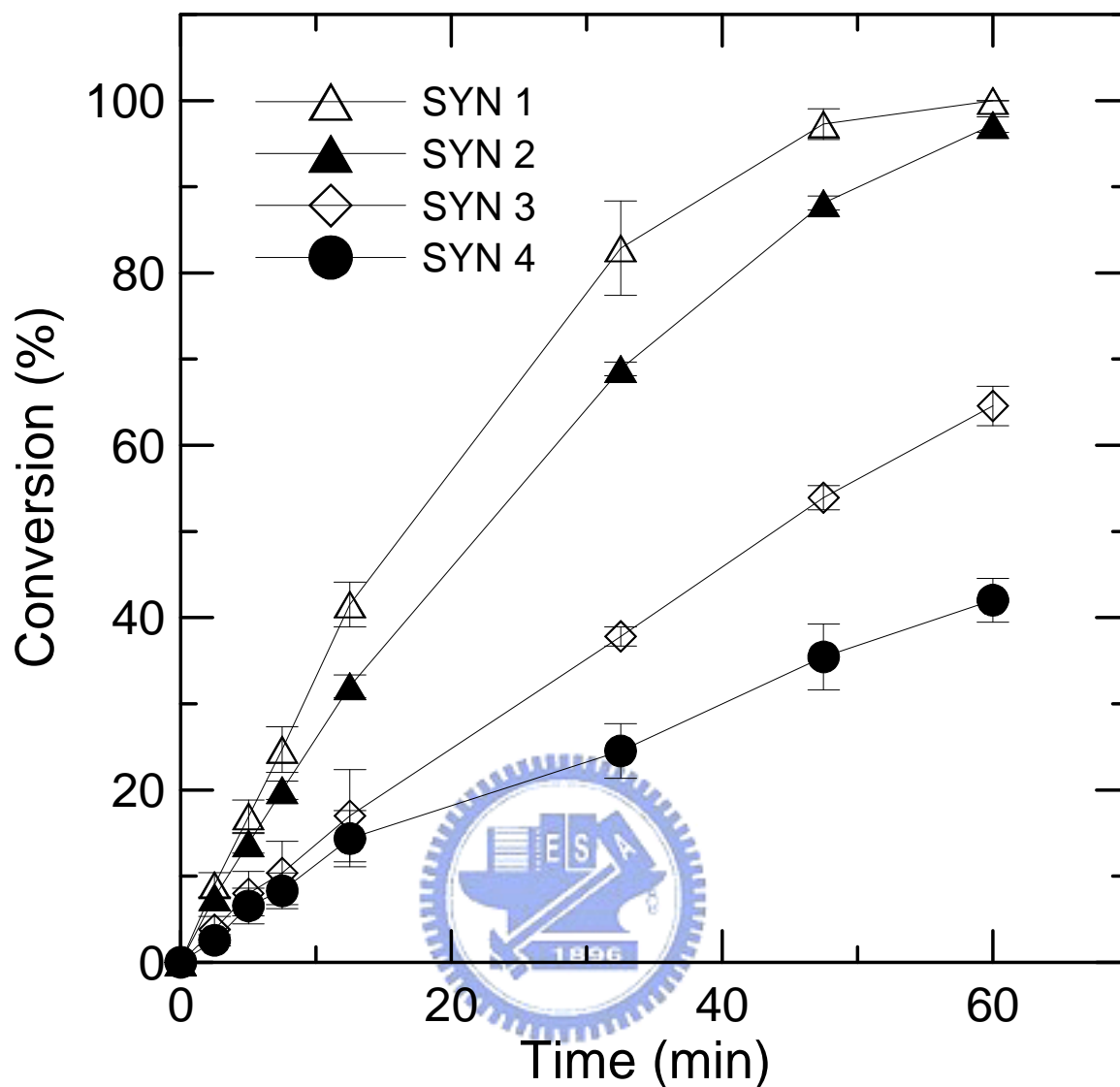


**Figure 4.13** The IPA conversion under visible light source (435, 488, 545, 587 and 611 nm, 10 W) at 45°C with a batch type photocatalytic reactor. All error bars of each data were determined from the repeated experimental data.

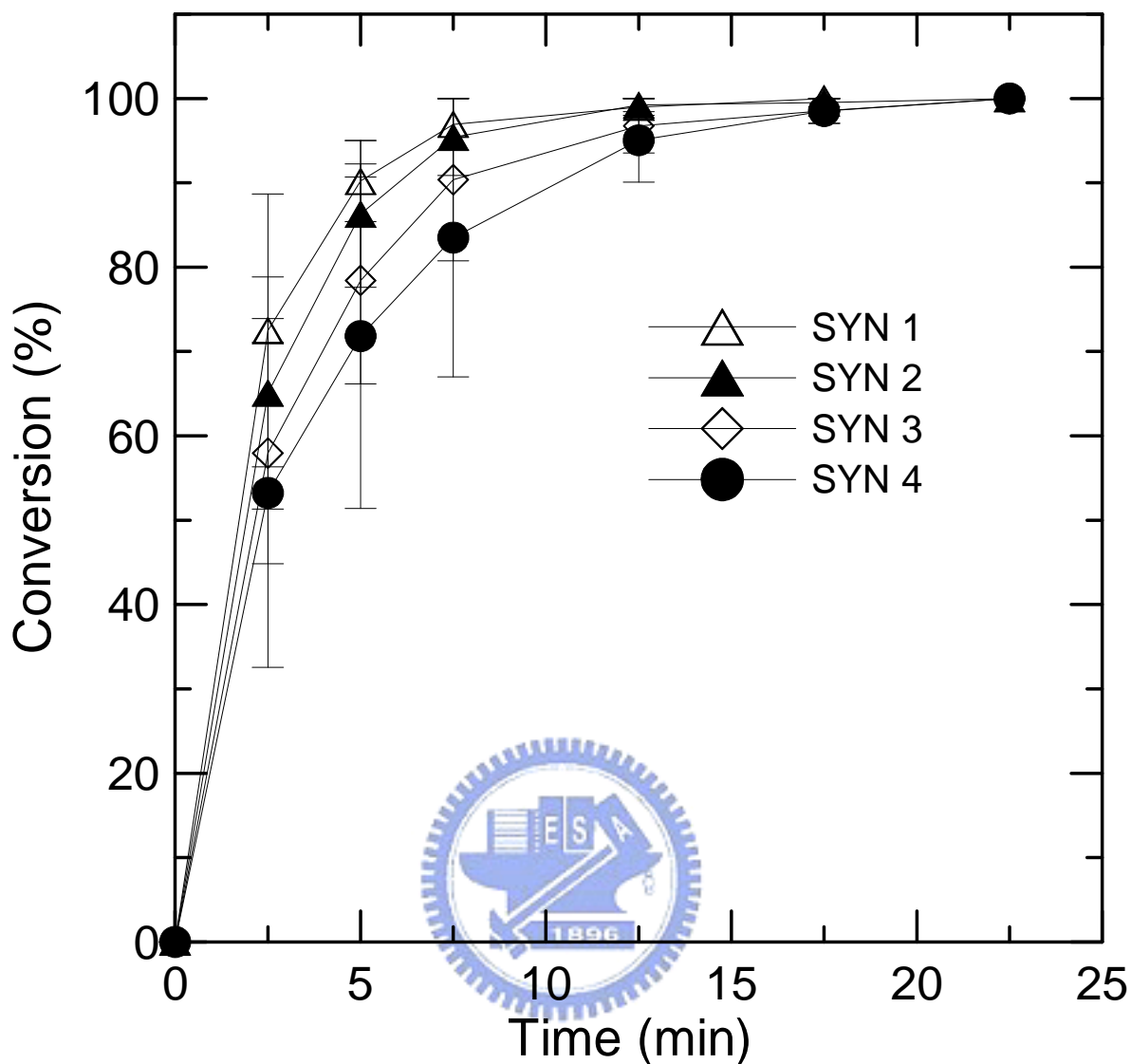


**Figure 4.14 The IPA conversion under UV light source (364.5 nm, 10 W) at 45°C with a batch type photocatalytic reactor. All error bars of each data were determined form the repeated experimental data.**

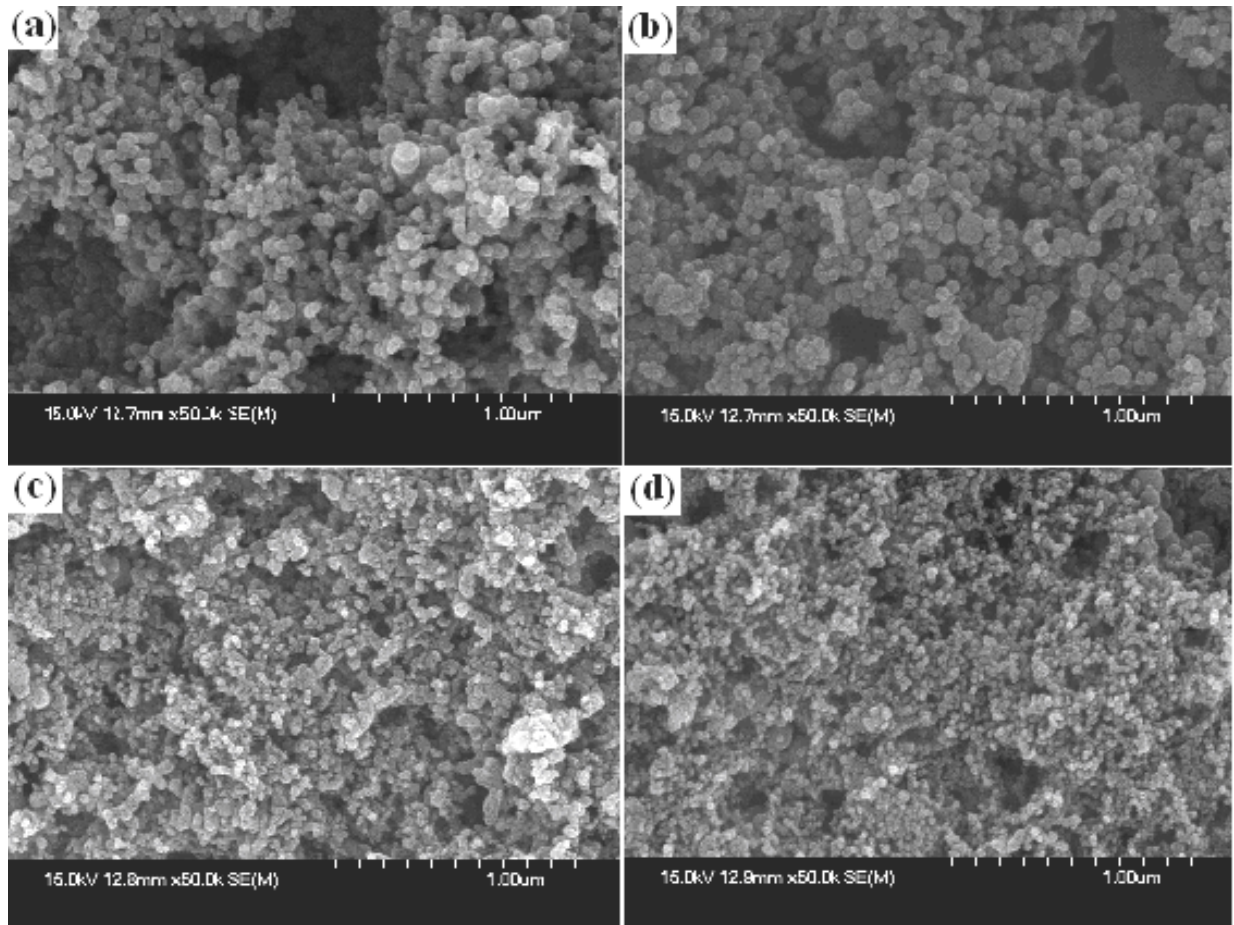


**Figure 4.15 SEM photo images of particles produced via (a). SYN1, (b) SYN2, (c). SYN3 and (d). SYN4.**

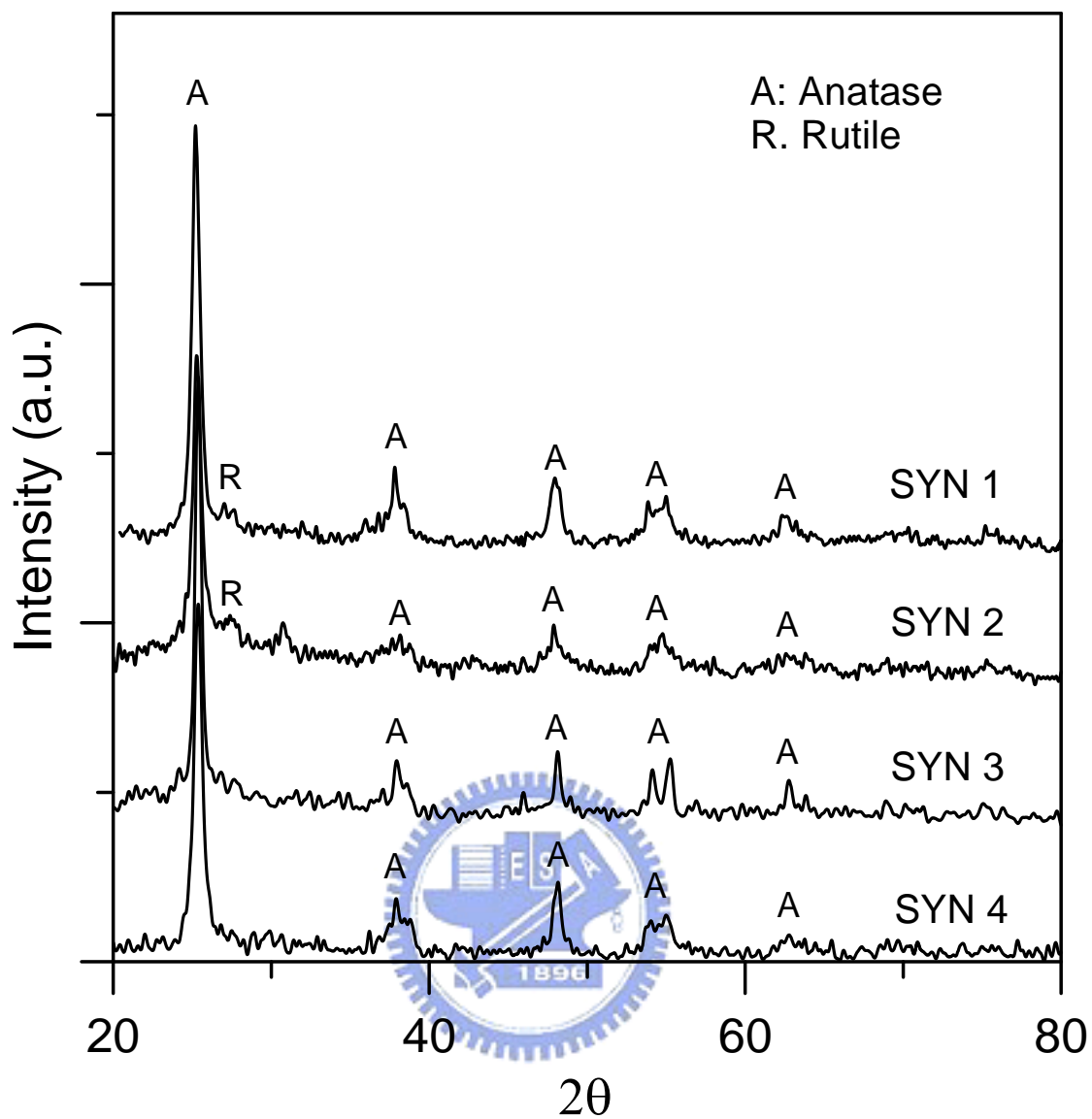
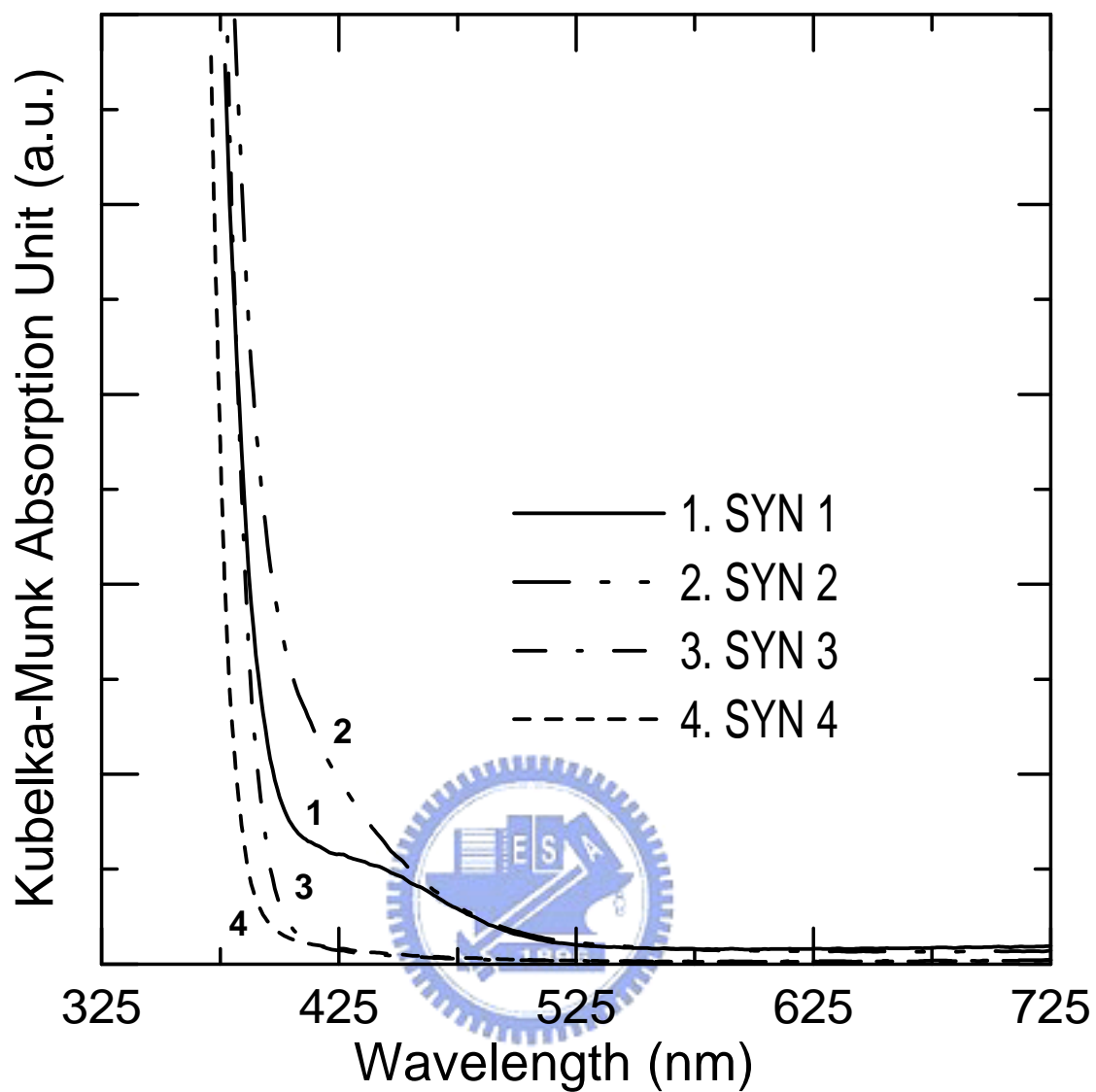
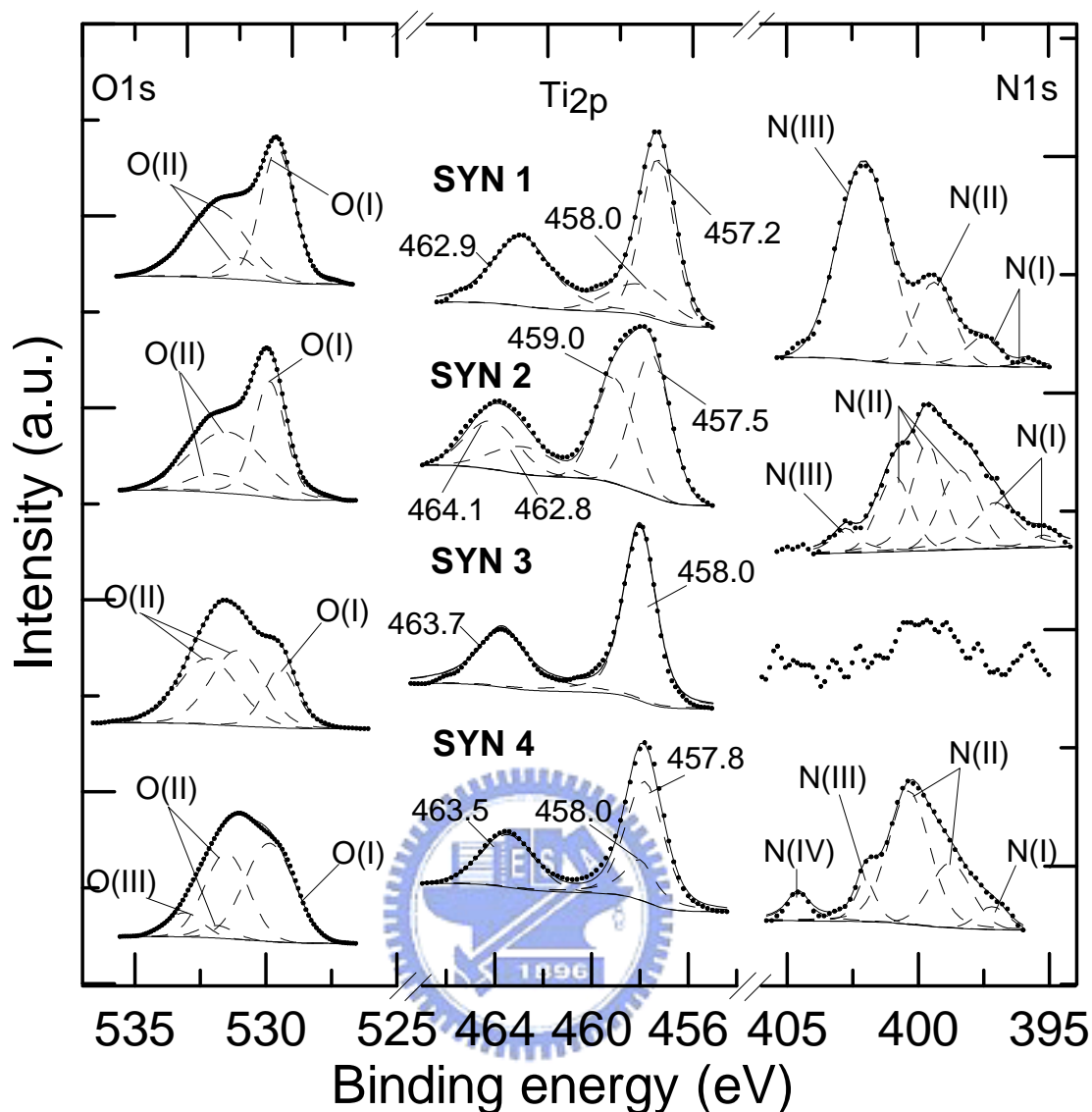


Figure 4.16 The XRPD patterns of photocatalytic particles synthesized in this study.





**Figure 4.17** The Kubelka-Munk absorption spectra of N-doped photocatalysts synthesized in this study.



**Figure 4.18** The XPS patterns of O 1s, Ti 2p and N 1s spectra for photocatalytic particles produced in this study. The spectra shown from top to bottom are for SYN1 to SYN4 photocatalysts. The dots were XPS measured spectra while the dash lines are the fittings of possible binding energy spectra to the XPS data, and the solid lines are the sum of the fitted data. Possible dopants of O(I)~O(III) and N(I)~N(IV) are referred to Table 2.3. And a cross comparison of the binding energy between O 1s, Ti 2p, N 1s to father clarify the N-doped status is shown latter in Figure 4.19.

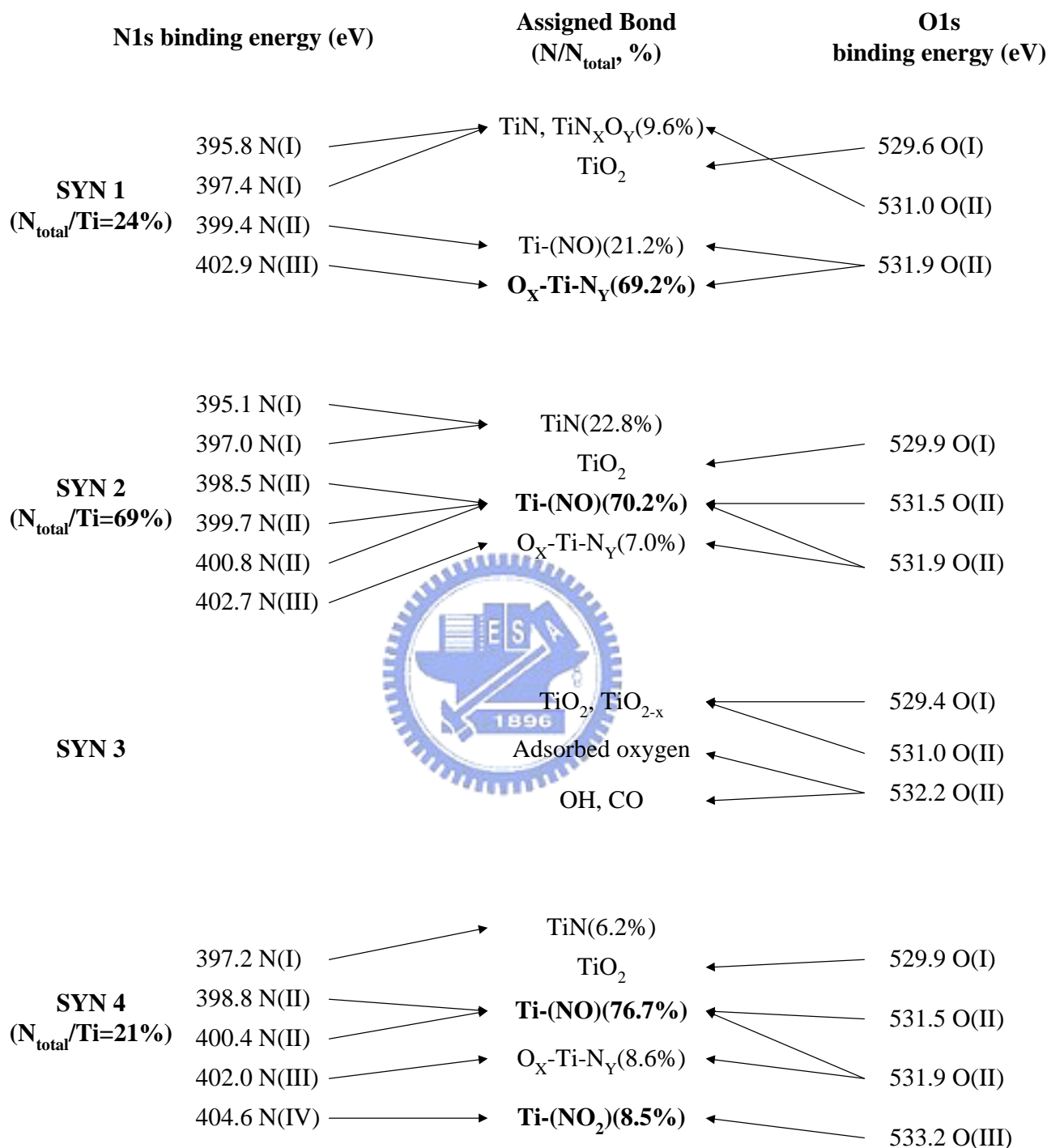
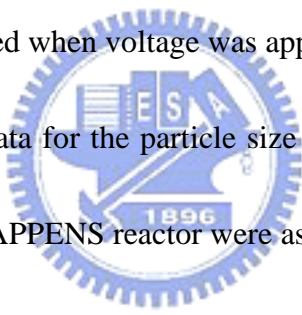


**Figure 4.19** The nitrogen doping status for SYN1~SYN4 synthesized photocatalysts based on cross comparison of N 1s and O 1s binding energies.

## 4.4. EFFECT OF PROCESS PARAMETERS IN CRYSTALLITE AND PARTICLE SIZE

### 4.4.1. Effect of applied voltage

For the study of the effect of applied voltage on the size distribution of generated particles, the TTIP/H<sub>2</sub>O precursor molar ratio was 11.9 as bubbled at temperature of 150°C and the frequency was 60 Hz in the aerosol generator. Figures 4.20(a)-(d) show the SEM images of the particles generated at applied voltage of 0, 6.48, 8.58 and 9.60 kV, respectively. It was observed that the generated particles were in a broad size distribution as no voltage was applied, and the particle sizes could be as large as 1 µm or smaller than 100 nm. On the other hand, the particle sizes became smaller and more uniformly distributed when voltage was applied.



The SMPS on-line measurement data for the particle size distribution are shown in Figure 4.21. The experimental conditions for the APPENS reactor were as the same as that shown in Figure 4.20. When no voltage was applied, the TiO<sub>2</sub> particles show bi-modal distribution with two mode sizes at around 106 nm and 372 nm, respectively. In addition, the particle size appears to be uni-modal distributed as the voltage was applied. The mode of particle size decreases from 163 nm to 27.9 nm as increasing the applied voltage from 6.48 to 8.58 kV. Further increases in the values of applied voltage to 9.60 and 10.20 kV result in increases in the mode size instead. The lognormal fittings (dashed-lines) seem to obtain good correlation with the SMPS online measurement data (step-lines) for the plasma produced particles. The calculated values of  $\sigma_g$  ranged from 1.43 to 1.83 for particles generated at the applied voltage of 6.48 to 10.20 kV.

Values of  $Dp_g$  of generated particles at applied voltage of 6.48, 8.58, 9.60 and 10.20 kV were also determined from the SEM images and they were 75, 31, 39 and 43 nm, respectively, with their corresponding values of  $\sigma_g$  of 1.5, 1.2, 1.4 and 1.3. By comparing values of  $Dp_g$  and  $\sigma_g$  determined from the SEM images to those from SMPS data, one can see that particle sizes measured by the SMPS were larger and the distribution were broader. This is opposite to those predicted by the diffusion and electrostatic mechanisms that particles deposited on the reactor wall should have broader size distribution than those penetrating the reactor. The larger  $Dp_g$  and  $\sigma_g$  of particles penetrating the reactor may be mainly caused by that loosely agglomerated particles were counted by the SMPS as one single particle. This is confirmed by that values of  $\sigma_g$  measured by the SMPS (shown in Figure 4.21) are larger than the value predicted by the self preserving size distribution theory for coagulating spheres, 1.33 (Vemury et al. 1994). Larger values of  $\sigma_g$  are typically the result of particle agglomeration without coalescence in the gas phase.

Nakaso et al. (2003) indicated that faster reaction rate of TTIP conversion led to narrow particle size distribution. In this study, the TTIP conversion rate is enhanced by applying the plasma in this system. In addition, the non-thermal plasma kept the gas temperatures to be low within and after the aerosol generator. This particular condition is similar to the effect of cooling gas which can restrain the coalescence between the particles (Joshi et al., 1990; Tsantilis and Pratsinis, 2004b). On the contrary of without applying any voltage or at low applied voltage, the bi-modal size distribution or broad distribution may be due to the slow reaction rate of precursors or particles (Kuster and

Pratsinis, 1995; Ahonen et al., 1999; Nakaso et al., 2003). Thus the application of plasma not only avoided the further coalescence of the agglomerated particles, but also enhanced the hydration rate of the precursors.

#### 4.4.2. Effect of electric frequency

The effects of electric frequency at 60, 120 and 240 Hz on the morphology and size distribution of particles were investigated by the SEM and SMPS analyses and results are shown in Figure 4.22.

The applied voltage was 10.20 kV and the TTIP/H<sub>2</sub>O precursor molar ratio was 11.9 by bubbling of the TTIP at 150°C. A very interesting phenomenon was observed from the SMPS data that as increasing the frequency from 60 Hz to 240 Hz, the particle concentration decreases significantly.

The SMPS distributions in Figure 4.22 for the 120 Hz and 240 Hz are so low in concentration that they may not be representative of the actual size distribution of the particles produced.

The SEM morphology of particles deposited in the reactor which generated at 240 Hz was very different from those at 60 and 120 Hz as seen from Figure 4.22. The particles seemed to develop a film at 240 Hz. The approximate sizes of particles from SEM images for 60 and 120 Hz are 43 and 34 nm, respectively. But the particle sizes of 240 Hz were difficult to calculate from this SEM image due to its film structure. This result is similar to reported data on the SiO<sub>2</sub> thin film deposited at high frequency of 20~100 KHz (Thyen et al., 1997; Foest et al., 2003). Therefore, most of the precursor vapors deposited in the plasma reactor and formed a thin film at frequency of 240 Hz. This may explain why a lower particle concentration was measured after the reactor by SMPS as the

applied frequency was increased. As a result, the APPENS could work as an aerosol generator at lower frequency of 60 Hz. And it can also be applied for producing thin film at higher frequency of 240 Hz. But for a frequency of 120 Hz, the SMPS detected too low particle concentration while the SEM did not observe a nice film developed so it maybe applied for neither purpose.

#### 4.4.3. Effect of precursor molar ratio

The crystalline phase of generated particles was determined by the XRPD patterns and the results are shown in Figure 4.23. The XRPD peaks at around 25.3°, 38.6°, 48.0°, 55.1° and 62.7° corresponding to anatase crystal are observed for all synthesized samples, with the most significant peak at around 25.3°. And the peak intensities at all angles seem to be increased with increasing the molar ratio. The effect of TTIP/H<sub>2</sub>O precursor molar ratios on the crystalline sizes of particles was estimated from XRPD data by Scherrer equation (Musić et al., 1997). The calculated crystalline sizes are listed in Table 4.4. As seen in Table 4.4, the average crystalline size of particles generated at TTIP bubbling temperature of 200°C is around 23.5±2.4 nm, which is slightly larger than the value of 22.2±1.1 nm at 150°C. And the average of all data is 22.8±2.0 nm. The data are within the experimental error and thus one can say that the effect of molar ratio on crystalline sizes of particles is not significant.

The primary particle can be composed of more than one crystal or can be partly crystalline and contain some amorphous TiO<sub>2</sub>. The effect of precursor molar ratio on the primary particle size is also evaluated via averaging over 80 particles in the SEM images under each test condition. The

results shown in Figure 4.24 with symbols indicate that the SEM averaged size distribution data and lines are logarithmic regression results of  $Dp_g$  and  $\sigma_g$  with respective to the precursor molar ratio.

One can see in Figure 4.24 that decreasing the precursor molar ratio results in a smaller and uniform particle size. Based on the regression curves,  $Dp_g$  of particles decreased from around 60 nm to 30 nm and  $\sigma_g$  of particle distribution is decreased from 1.6 to 1.2 as decreasing the TTIP/H<sub>2</sub>O precursor molar ratio from 76.1 to 0.4. The precursor molar ratio has a slightly stronger effect on  $Dp_g$  at TTIP bubbling temperature of 200°C. But values of  $\sigma_g$  for data obtained at 200°C do not seem to be increased further as increasing the TTIP/H<sub>2</sub>O molar ratio. It is noted that at very low TTIP/H<sub>2</sub>O precursor molar ratio the generated particle number concentration (<1.1) is much lower. Hence the decreasing of  $\sigma_g$  to monodisperse aerosol by decreasing TTIP/H<sub>2</sub>O precursor molar ratio is accompanied by that less particles are generated. This may not be acceptable for some particle generation applications.

To further verify the precursor effect on the particle size distribution, TEM images were also taken and shown in Figures 4.25(a) and (b), respectively, for TTIP/H<sub>2</sub>O precursor molar ratios of 1.1 and 76.1. The TEM images reveal similar trend to the SEM images shown in Figure 4.24 that increasing the precursor concentration leads to a broader size distribution. At a low TTIP/H<sub>2</sub>O precursor molar ratio of 1.1, the particle sizes are near uniform with size of around 30~40 nm. From Figure 4.24 one knows that at TTIP/H<sub>2</sub>O precursor molar ratio of 1.1 and TTIP bubbling temperature of 150°C, value of  $Dp_g$  is around 35 nm and  $\sigma_g$  is around 1.2. Based on the lognormal



distribution, 95% of the particles for such a size distribution should fall in the range 29-42 nm. This size range corresponds well with the TEM observation (Figure 4.25(a)). At a high TTIP/H<sub>2</sub>O precursor molar ratio of 76.1, the TEM observed a much broader particle size distribution with particle size ranges 15-80 nm.

The observation that higher precursor concentration leads to higher particle size distribution seems to be opposite to the TiO<sub>2</sub> thermo-decomposition result of Pratsinis and Spicer (1998), where surface reaction is the dominating mechanism for the change of particle size distribution. This can be explained by that the hydrolysis reaction of TTIP with H<sub>2</sub>O is much faster than the thermo-decomposition rate of TTIP (Okuyama et al., 1990; Seto et al., 1995). Thus hydrolysis reaction is the dominating mechanism for the formation of TiO<sub>2</sub> particles at low TTIP/H<sub>2</sub>O molar ratio, thus the particle size distribution is narrower. On the other hand, at high TTIP/H<sub>2</sub>O molar ratio (above the stoichiometric ratio of hydrolysis reaction) the formation of TiO<sub>2</sub> particles was firstly induced by hydrolysis reaction, then excess of TTIP forms TiO<sub>2</sub> monomers by thermo-decomposition mechanism, and the monomers either nucleate as new particles or condense onto the TiO<sub>2</sub> particles which were previously formed by hydrolysis reaction. As a result, the particle size distribution is broader at high TTIP/H<sub>2</sub>O precursor molar ratio due to both hydrolysis and thermo-decomposition reactions occurred for the formation of TiO<sub>2</sub> particles.

#### 4.4.4 Long term stability

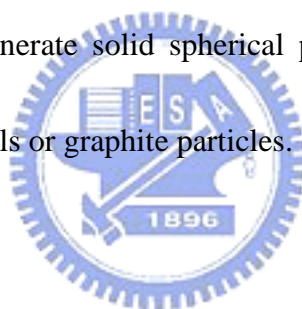
The size distributions of particles generated from APPENS reactor were measured continuously by SMPS for 1 hr to test the long term stability of the aerosol generator, and variations of  $Dp_g$  and  $\sigma_g$  with respect to time are shown in Figure 4.26. The generator was operated under conditions of TTIP/H<sub>2</sub>O precursor molar ratio of 0.7 (with TTIP bubbled at 150°C), applied voltage of 9.60 kV, frequency of 60 Hz and without any dilution. The average value of  $Dp_g$  of generated particles is  $40.7\pm 0.5$  and  $\sigma_g$  of them is  $1.43\pm 0.1$ . The result indicated that the particle size distribution is stable and the APPENS generator can be used for long term operation.

#### 4.4.5. Comparison of APPENS generator with commercial aerosol generators

Table 4.5 compares the properties of particles generated via the APPENS generator to the furnace reactor as well as to commercial nano-size range (<100 nm) aerosol generators. Both the APPENS and the furnace reactor produce particles via chemical process of gas to particle conversion. The furnace reactor produces TiO<sub>2</sub> particles at high temperature via thermo-decomposition mechanism and the particle number concentration is very high ( $10^{10}$  #/cm<sup>3</sup>) with  $\sigma_g$  of around 1.3~1.5. The APPENS generator is operated at room temperature and it produces TiO<sub>2</sub> particles via hydrolysis and thermo-decomposition mechanisms. It is capable of generating particles with number concentration of around  $10^6$  #/cm<sup>3</sup> and  $\sigma_g$  of around 1.2 to 1.5.

As for the commercial aerosol generators, the electrospray aerosol generator is a monodisperse nanoparticle generator, while the atomizer and the spark aerosol generators generate polydisperse

particles. The generated particles from both atomizer and spark aerosol generator (GFG-1000) are in a broad size range ( $\sigma_g > 1.6$ ) and thus classifiers are needed to produce monodisperse nanoparticles. The electrospray aerosol generator produces particles from the charged solution through the capillary by electrical field pulling. The atomizer atomizes liquid particles through an orifice by high-velocity jet. The spark aerosol generator (GFG-1000) uses high voltage to generate sparks between two graphite electrodes and forms graphite fine particles by evaporation-condensation mechanism. The morphologies of generated solid particles were spherical via APPENS and furnace reactor. The electrospray and atomizer can also generate spherical liquid aerosol, but they are difficult to generate solid spherical particles. The spark aerosol generator (GFG-1000) can generate either metals or graphite particles.



#### 4.4.6. Summary

The effects of applied voltage, frequency and the precursor molar ratio on particle morphology and particle size distributions were described in this section. The results showed that  $\text{TiO}_2$  particles appear to be in a broad size range of bi-modal distribution when no voltage is applied. While after applying the AC plasma they become uni-modal distributed with average sizes range from around 30 to 60 nm. But if the applied voltage is increased to be too strong ( $\sim 10.2$  kV), the melting possibility of smaller particles in the agglomerates is increased. This leads to larger product particles or hard agglomerates of small particles. Hence the optimal applied voltage is 9.6 kV for better production of catalytic particles with nanosize distribution, high production yield and less

agglomeration. The applied electric frequency can be adjusted to either generate nanoparticles after the plasma reactor or develop a thin film in the reactor. An increase in the precursor molar ratio leads larger particles with a broader size distribution.

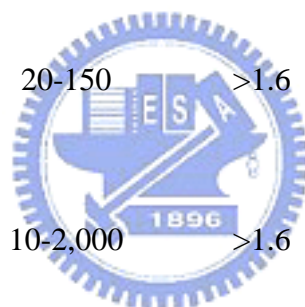


**Table 4.4 Crystallite size of TiO<sub>2</sub> particles generated via different TTIP/H<sub>2</sub>O precursor molar ratios. The crystalline sizes of primary particle were calculated using Scherrer equation with parameter values obtained from XRPD patterns at X-ray wavelength ( $\lambda$ ) of 0.154056 nm.**

TTIP bubbling temperature (°C)	Flow ratio (TTIP/H <sub>2</sub> O)	Molar ratio (TTIP/H <sub>2</sub> O)	FWHM	2 $\theta$ (degree)	Crystalline size (nm)
150	8	23.9	0.0064	25.33	22.2
150	2	6.0	0.0067	25.33	21.3
150	1	3.0	0.0065	25.28	21.8
150	0.125	0.4	0.0061	25.36	23.3
150	Average size	-	-	-	22.2±1.1
200	4	76.1	0.0067	25.31	21.1
200	1	19.0	0.0057	25.29	24.8
200	0.5	9.5	0.0058	25.30	24.5
200	0.25	4.8	0.0061	25.35	23.5
200	Average size	-	-	-	23.5±2.4
Total average size		-	-	-	22.8±2.0

**Table 4.5 Comparison of the APPENS generator with commercial aerosol generators. Only nano-size (<100 nm) aerosol generators are included.**

Aerosol generator	Particle Generation Mechanism	Size range (nm)	$\sigma_g$	Total concentration (#/cm <sup>3</sup> )	Morphology / Component of generated particles
This study (APPENS)	Nonthermal plasma/hydrolysis& thermal decomposition	<10~100 (with controllable average size ranges from 30-60)	1.2-1.5	10 <sup>6</sup>	Spherical (solid phase)/ TiO <sub>2</sub> at the present time
Furnace reactor (Nakaso et al., 2001)	High temperature flame/ Thermal decomposition	12-17 <sup>c</sup>	1.3-1.5	10 <sup>10</sup>	Spherical/ TiO <sub>2</sub>
		4-8 <sup>d</sup>	1.3-1.5	10 <sup>10</sup> -10 <sup>11</sup>	
Electrospray Aerosol Generator; 3480 <sup>a</sup>	Electrical field spray	2-100	1.1	10 <sup>7</sup>	Spherical (liquid phase)/ Soluble solids or nonvolatile liquids
Aerosol generator; GFG-1000 <sup>b</sup>	Spark	20-150	>1.6	10 <sup>7</sup>	Nature soot liked/ Graphite, metals
		10-2,000	>1.6	10 <sup>7</sup>	Spherical/ PSL <sup>e</sup> , DOP <sup>f</sup> , oils, and other aqueous or alcohol solutions or suspensions
Constant Output Atomizer; 3076, 3079, 9302 & 9306A <sup>a</sup> .	High velocity jet atomizing	10-2,000	>1.6	10 <sup>8</sup>	Spherical/ DEHS <sup>g</sup> , DOP, Emery 3004, Paraffines, PSL, Salt solutions
		10-2,000	>1.6	10 <sup>7</sup>	Spherical/ Water-soluble materials (salt or sugar)
		10-2,000	<2.0	10 <sup>7</sup>	Spherical/ PSL, DOP, DEHS, oils, and other aqueous or alcohol solutions or suspensions



<sup>a</sup>TSI Inc.

<sup>b</sup>PALAS® Aerosoltechnologie aerosol technology

<sup>c</sup>TTIP precursor

<sup>d</sup>TiCl<sub>4</sub> precursor

<sup>e</sup>PSL: Polystyrene latex

<sup>f</sup>DOP: Di-octyl phthalate

<sup>g</sup>DEHS: Di-ethyl-hexyl-sebacin acid

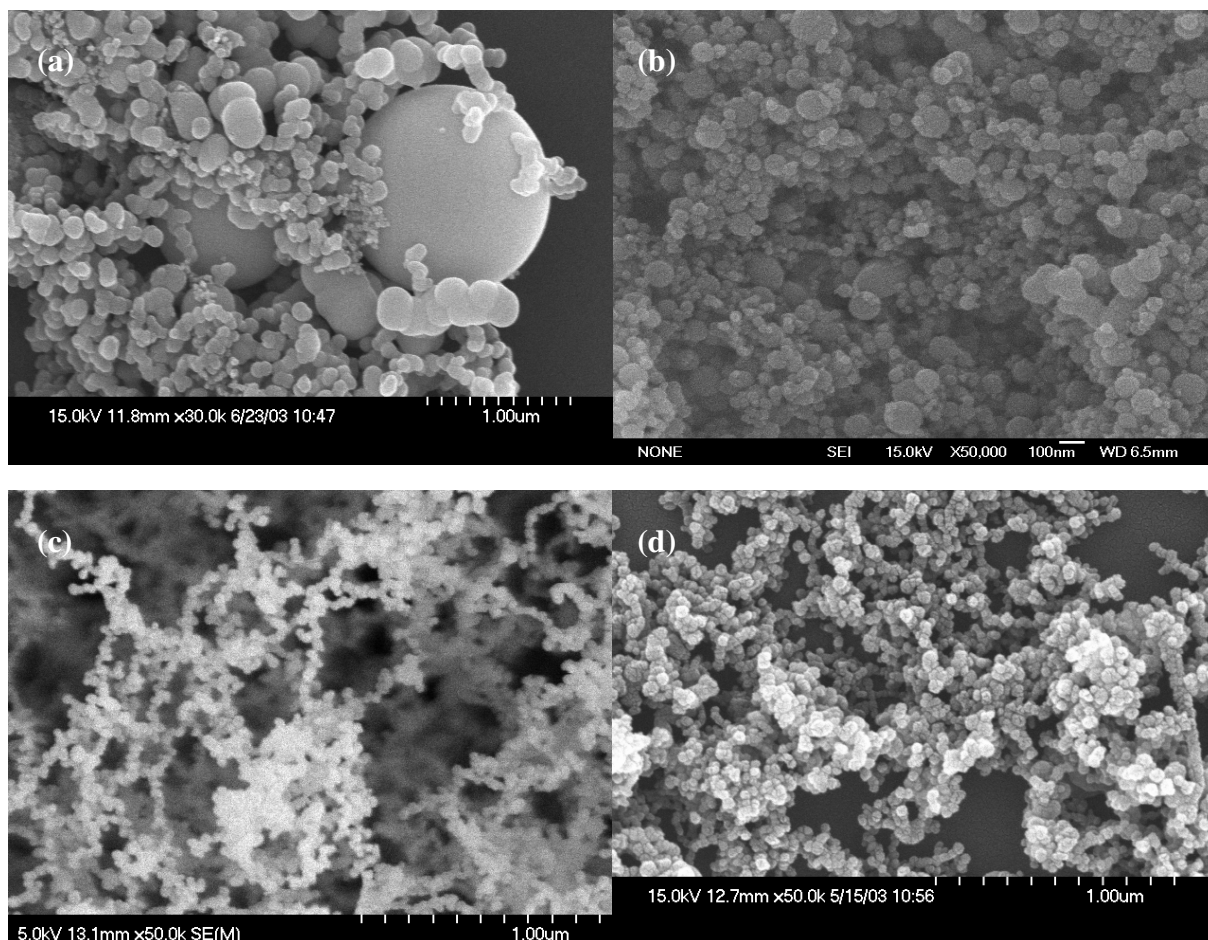


**Figure 4.20 SEM images of  $\text{TiO}_2$  particles collected in the reactor at different applied voltages. (a) No applied voltage, (b) 6.48 kV, (c) 8.58 kV and (d) 9.60 kV. The frequency was 60 Hz, the TTIP/ $\text{H}_2\text{O}$  precursors molar ratio was 11.9 as TTIP bubbled at  $150^\circ\text{C}$ . The scale bar in the SEM photo is 1  $\mu\text{m}$ .**

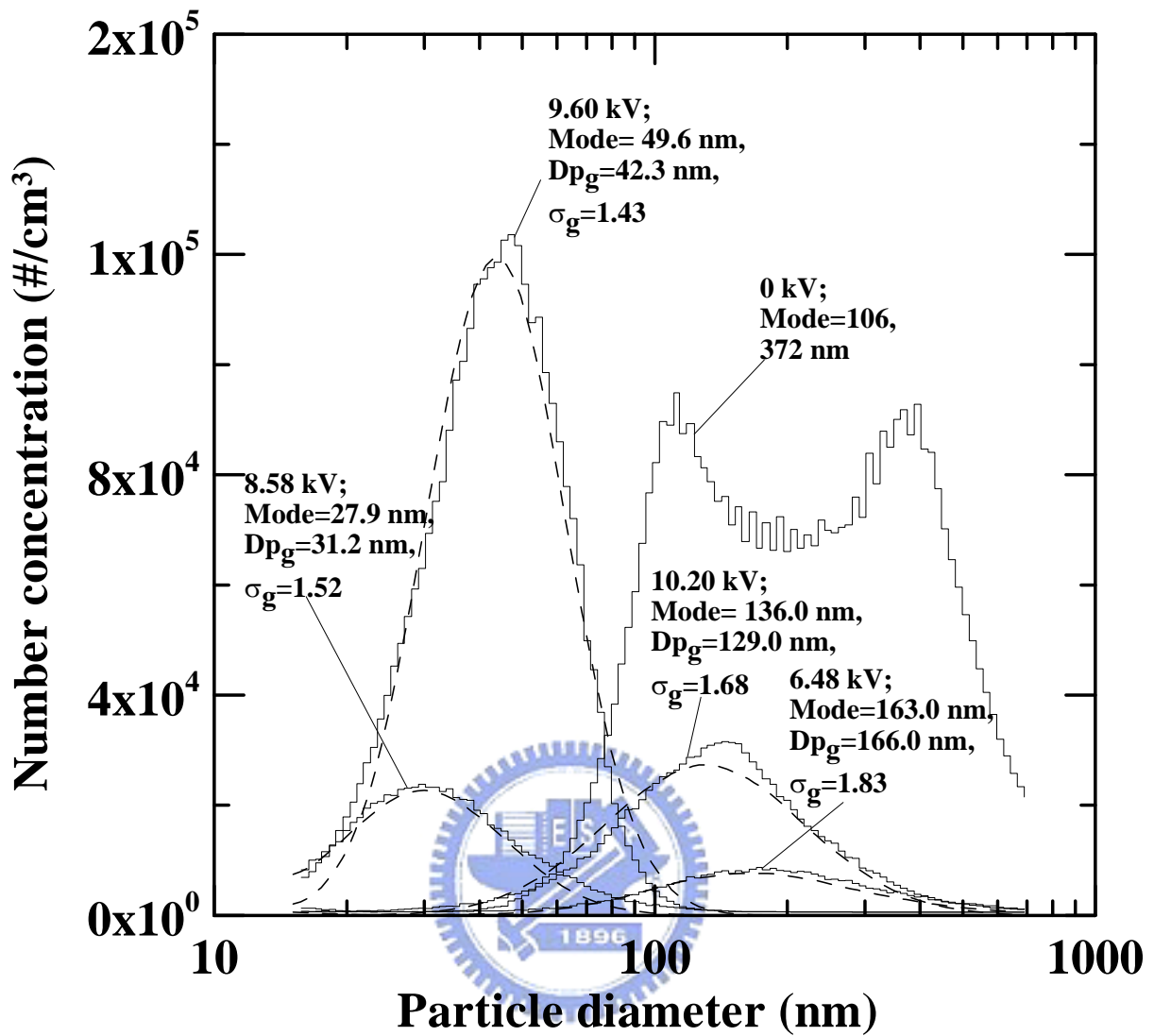
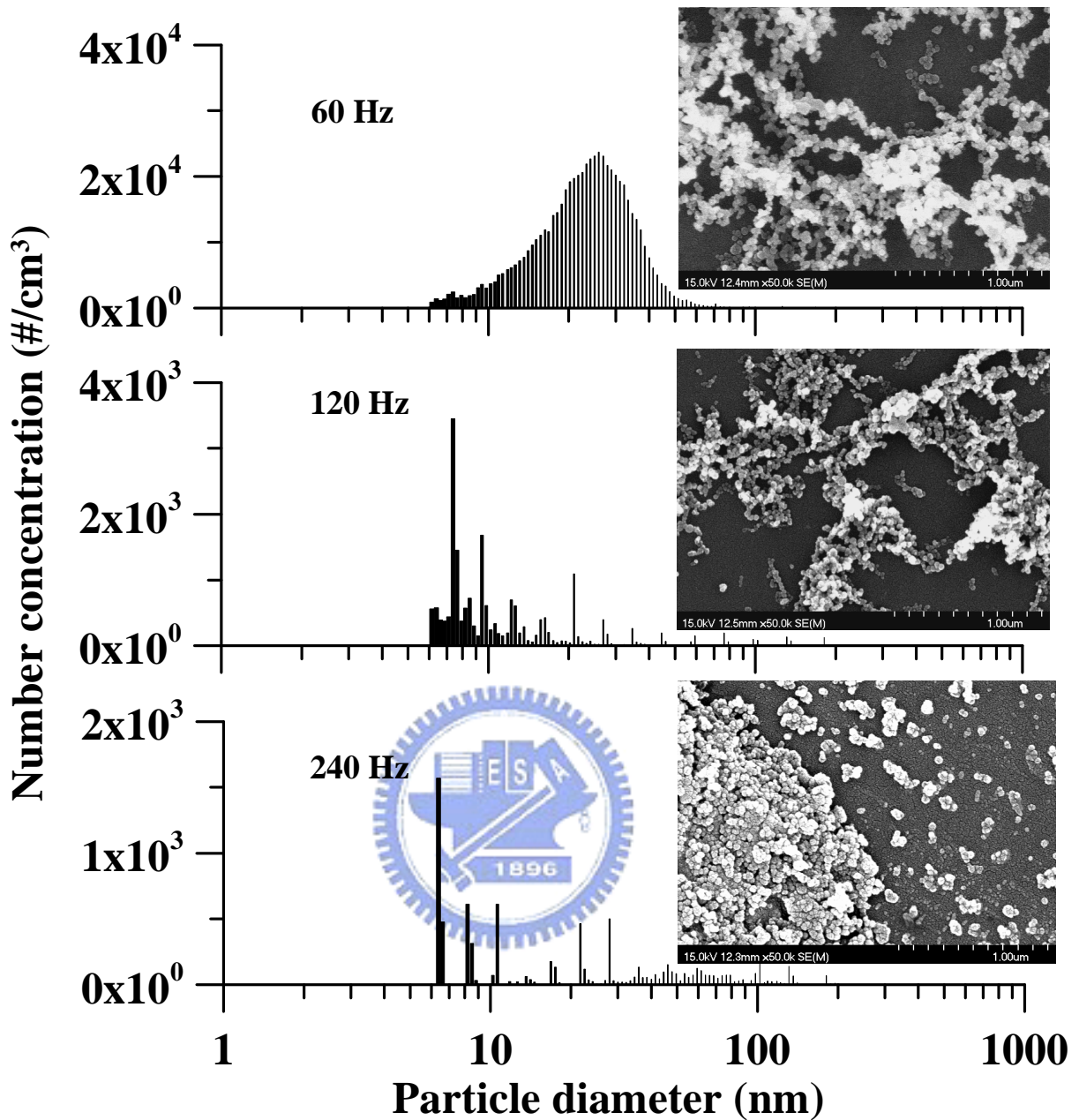


Figure 4.21 Particle size distributions measured by SMPS after dilution ratio of 1. The operation condition was the same as that of Figure 4.20. Step-lines are SMPS measured data obtained at different applied voltages, and dash-lines are their lognormal fittings.





**Figure 4.22 Particle size distributions measured by SMPS after dilution ratio of 12 under different electric frequencies. Also shown are SEM images of the reactor-deposited particles. The applied voltage was 10.20 kV, the TTIP/H<sub>2</sub>O precursor molar ratio was 11.9 as TTIP bubbled at 150°C.**

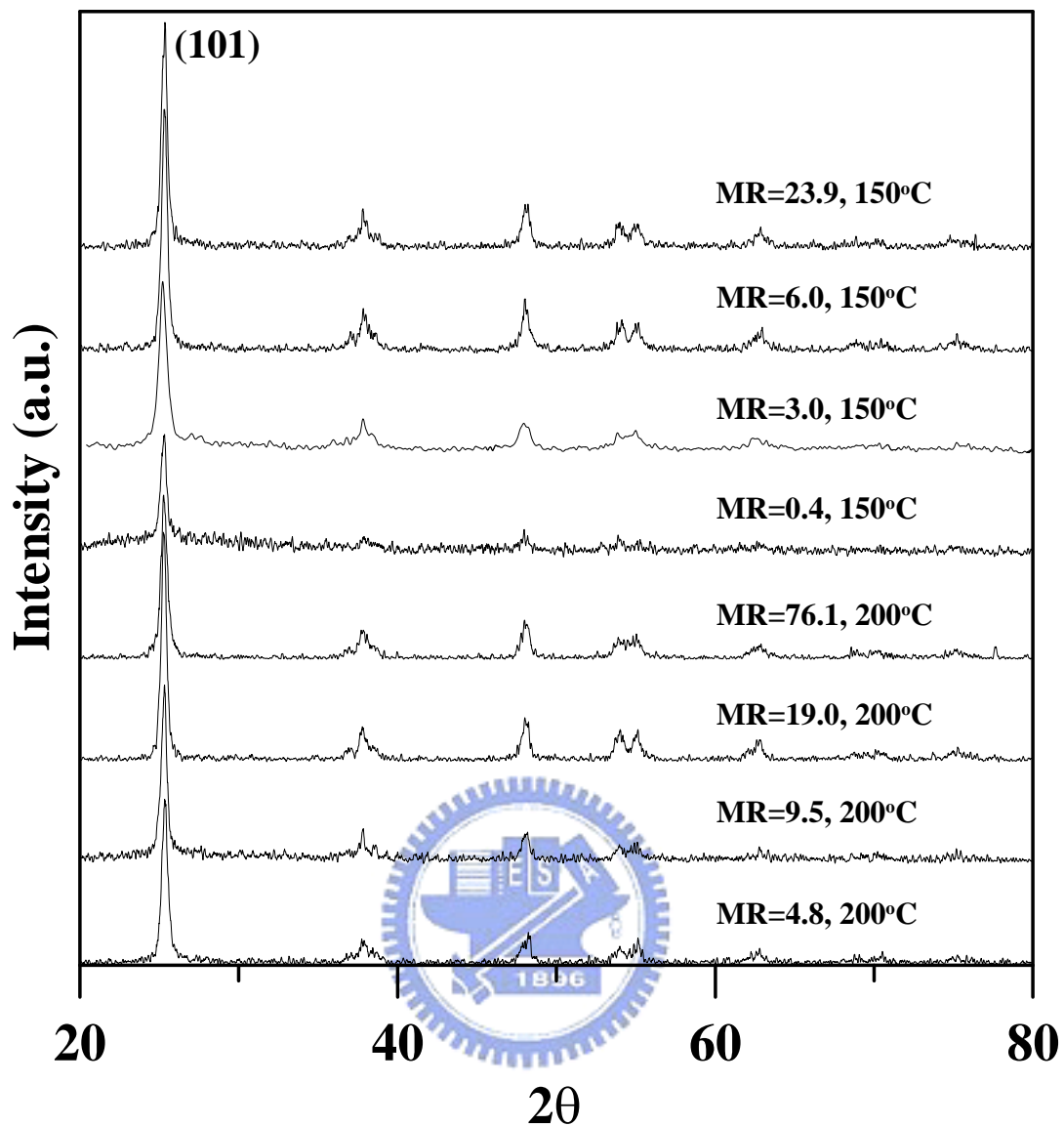


Figure 4.23 The XRPD patterns of generated particles synthesized in this study. The operation condition was the same as that of Table 1 with TTIP/H<sub>2</sub>O precursor molar ratio (MR) from 0.4 to 76.1 and TTIP bubbling temperature of 150 or 200°C.

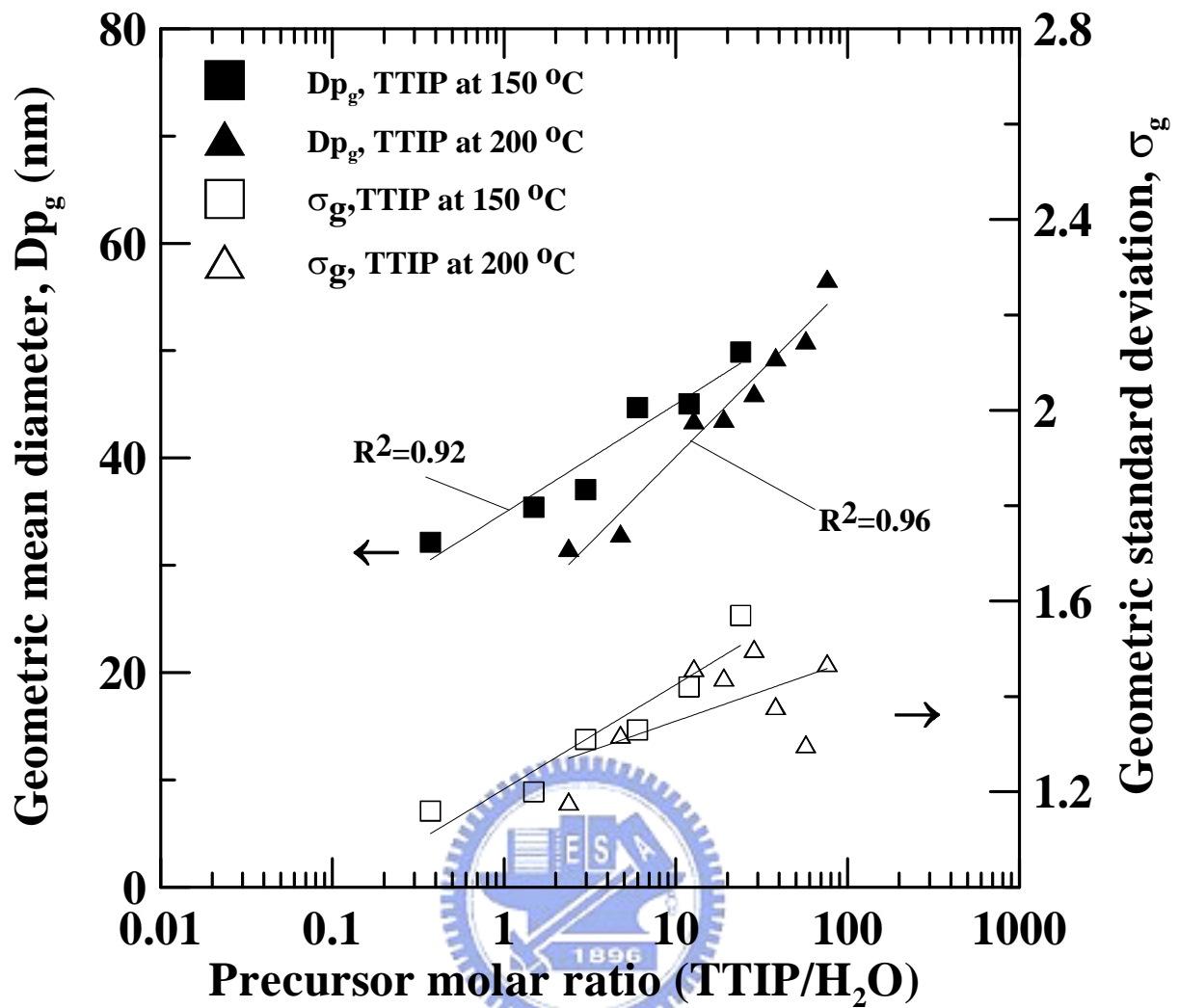
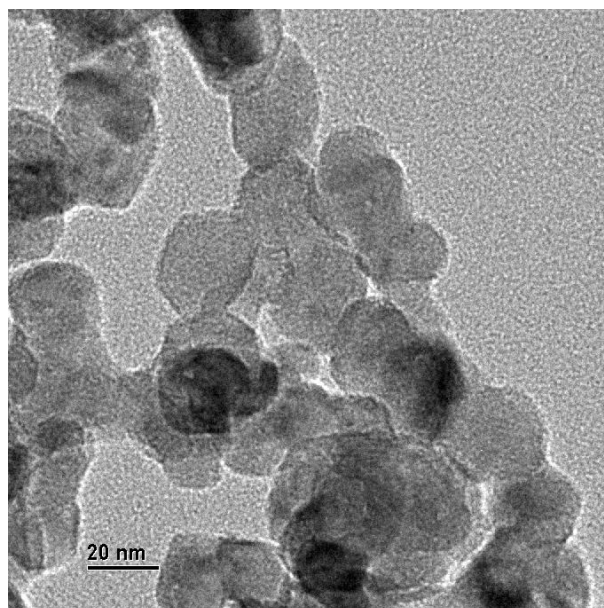
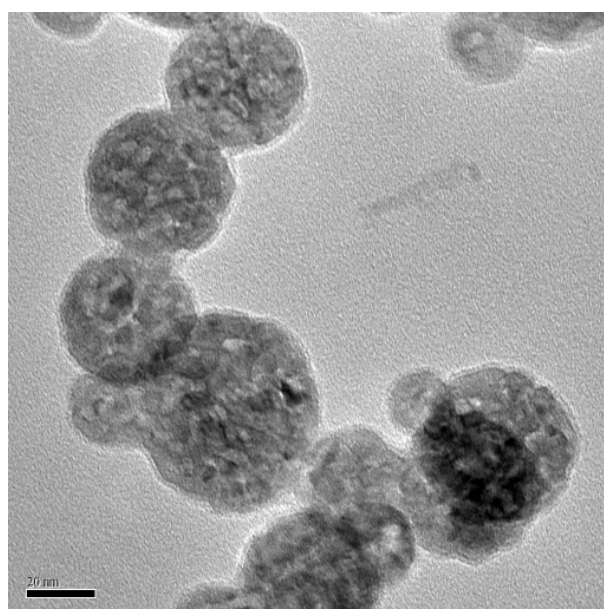


Figure 4.24 Effect of precursor molar ratio on the size distributions of particles collected in the reactor and measured by SEM images. The applied voltage was 9.60 kV and the TTIP bubbling temperatures were at 150 or 200°C.



(a). TTIP/H<sub>2</sub>O molar ratio= 1.1



(b). TTIP/H<sub>2</sub>O molar ratio= 76.1

**Figure 4.25 TEM images (scale bar = 20 nm) of particles collected in the reactor as obtained at two different TTIP/H<sub>2</sub>O precursor ratios of 1.1 and 76.1, respectively. The applied voltage was 9.60 kV and the TTIP bubbling temperatures were at 150 and 200°C, respectively. The low TTIP/H<sub>2</sub>O precursor ratio of 1.1 clearly indicates higher uniformity of TiO<sub>2</sub> particles.**

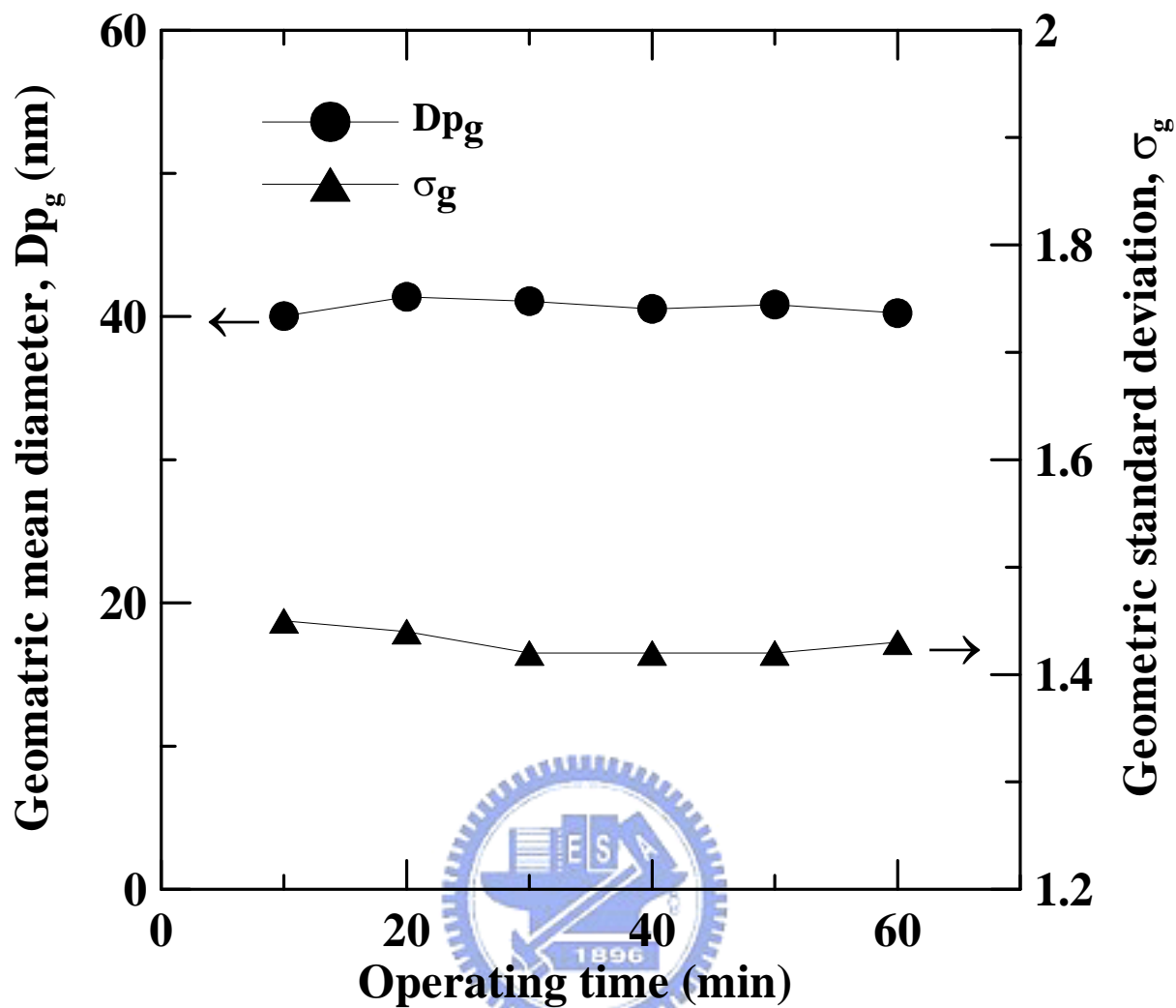


Figure 4.26 Stability of geometric mean particle diameter ( $D_{p_g}$ ) and geometric standard deviation ( $\sigma_g$ ) measured by SMPS during one hour of operation time. The frequency was 60 Hz, the TTIP/ $H_2O$  molar ratio was 0.7 as TTIP bubbled at  $150^\circ C$  and the applied voltage was 9.60 kV.

## CHAPTER FIVE CONCLUSIONS AND RECOMMENDATION

### 5.1. CONCLUSIONS

The N-doped TiO<sub>2</sub> photocatalyst particle was successfully prepared in this study via the APPENS process. The results showed that the N-doped TiO<sub>2</sub> photocatalyst was more effective in removing IPA under both UV and visible light sources than the un-doped TiO<sub>2</sub> photocatalyst. Effective removal of odorous VOCs in batch reactor; VOCs and NO<sub>x</sub> in continuous flow photocatalytic reactors under visible and UV light sources were demonstrated as well. The N-doped TiO<sub>2</sub> photocatalyst was superior in toluene removal than the commercial ST01 and P25 TiO<sub>2</sub> photocatalysts under visible light irradiation.

The different binding energies of Ti 2p, N 1s and O 1s obtained in this study via the XPS analysis had been grouped into several ranges as TiO<sub>2</sub> and TiN at 2p<sub>3/2</sub> and 2p<sub>1/2</sub>, N(I)~N(IV) for N 1s and O(I)~O(III) for O1s based on the literature data on N-doped TiO<sub>2</sub> photocatalysts. The N-doping status of TiN, Ti-(NO), O<sub>x</sub>-Ti-N<sub>y</sub> or Ti-(NO<sub>2</sub>) was confirmed by the cross comparison of chemical shift in the binding energies of N, Ti and O. It was found that Ti-(NO) and O<sub>x</sub>-Ti-N<sub>y</sub> are the most significant structures of the N-doped TiO<sub>2</sub> for the N<sub>2</sub> plasma processes. But Ti-(NO<sub>2</sub>) may be formed under the presence of both O<sub>2</sub> and N<sub>2</sub> plasma gases. Results on the photocatalytic activities in terms of IPA conversion indicated that in addition to the widely accepted TiN doping, both Ti-(NO) and O<sub>x</sub>-Ti-N<sub>y</sub> types of N-doping TiO<sub>2</sub> have positive effects, while the presence of Ti-(NO<sub>2</sub>) has a negative effect on the visible light photocatalysis.

The effects of applied voltage, frequency and the precursor molar ratio on particle morphology and particle size distributions were described in this study to explore the potential of APPENS as an aerosol generator. The APPENS generator can produce nanoparticles of uni-modal size distributions. It is concluded that the APPENS process has a high potential to be used as a size tunable monodisperse or polydisperse aerosol generator. The APPENS generator is simple to be composed of and can be scaled up by using several more parallel tubes to enlarge the production rate (Lin and Bai, 2001) as already approached for a commercial O<sub>3</sub> generator.

Considering that UV light accounts for only 3~5 % of the solar light intensity, and that indoor lighting is predominant in the visible light range, results presented in this study strongly suggest that the N-doped TiO<sub>2</sub> photocatalysts prepared via the APPENS process has a potential application in the area of indoor and outdoor air pollution controls. The advantages of the APPENS process, as compared to other plasma processes for producing N-doped TiO<sub>2</sub> films or particles, encompass advantages of operation under normal temperature and pressure as well as possessing a higher film deposition rate with lower power consumption.

## 5.2. RECOMMENDATION

NO removals by N-doped TiO<sub>2</sub> photocatalysts showed effectiveness under both UV and visible light illumination. However, the result that the transformation of NO to NO<sub>3</sub><sup>-</sup> need to be further studied and characterized. Although the chemical structures of N-dopants in the TiO<sub>2</sub> photocatalysts have been speculated in this study and their correlations with the photoactivity have been suggested, further work might still be necessary since there are several types of N-dopants presented in one

photocatalyst. And the actual coordination of the N-impurity can not be identified by the XPS data.

Furthermore, Livraghi et al. (2006) indicated that some of the N-induced defects are also responsible for the increased photoactivity. Therefore the simultaneous consideration of all possible factors for the photoactivity might be required. The production of a pure N-speciation in each photocatalyst to directly identify the N-dopant effect on the photocatalytic activity may be a challenge work in the future.

The APPENS process could be utilized for the purpose of either implication or application studies of TiO<sub>2</sub> nanoparticles. Further research work can be extended to generate other chemical components of nanoparticles such as SiO<sub>2</sub>, ZnO and MgO.





## REFERENCES

- Ahonen, P. P.; Kauppinen, E. I.; Joubert, J. C.; Deschanvres, J. L.; Tendeloo, G. V. (1999). Preparation of Nanocrystalline Titania Powder via Aerosol Pyrolysis of Titanium Tetrabutoxide. *J. Mater. Res.* 14, 3938-3948.
- Almquist, C. B.; Biswas, P. (2002). Role of Synthesis Method and Particle Size of Nanostructured TiO<sub>2</sub> on Its Photoactivity. *J. Catal.* 212, 145-156.
- Arabi-Katbi, O. I.; Pratsinis, S. E.; Morrision, P. W., Jr.; Megaridis, C. M. (2001). Monitoring the Flame Synthesis of TiO<sub>2</sub> Particles by in-situ FTIR Spectroscopy and Thermophoretic Sampling. *Comb. Flame.* 124, 560-572.
- Alberici, R. M.; Jardim, W. F. (1997). Photocatalytic Destruction of VOCs in the Gas-phase using Titanium Dioxide. *Appl. Catal. B* 14, 55-68.
- Asahi, R.; Morikawa, T.; Ohwaki, T.; Aoki, K.; Taga, Y. (2001). Visible-Light Photocatalysis in Nitrogen-Doped Titanium Oxides. *Science*, 293, 269-271.
- Bai, H.; Chen, C.; Lin, C.-H.; Den, W.; Chang, C. (2004). Monodisperse Nanoparticle Synthesis by an Atmospheric Pressure Plasma Process: An Example of a Visible Light Photocatalyst. *Ind. Eng. Chem. Res.* 43, 7200-7203.
- Battiston, G. A.; Gerbasi, R.; Gregori, A.; Porchia, M.; Cattarin, S.; Rizzi, G. A. (2000). PECVD of Amorphous TiO<sub>2</sub> Thin Films: Effect of Growth Temperature and Plasma Gas Composition. *Thin Solid Films* 371, 126-131.
- Berglund, R. N.; Liu, B. Y. H. (1997). Generation of Monodisperse Aerosol Standards. *Environ. Sci. Technol.* 7, 2, 147-153.
- Böer, K.W. (1990). Survey of Semiconductor Physics. *Van Nostrand Reinhold*. New York, 249.
- Brillas, E.; Mur, E.; Sauleda, R.; Sánchez, L.; Peral, J.; Domènech, X.; Casado, J. (1998). Aniline Mineralization by AOP's: Anodic Oxidation, Photocatalysis, Electro-Fenton and Photoelectro-Fenton Processes. *Appl. Catal. B* 16, 31-42.

- Cao, L.; Spiess, F. J.; Huang, A. M.; Suib, S. L.; Obee, T. N.; Hay, S. O.; Freihaut, J. D. (1999). Heterogeneous Photocatalytic Oxidation of 1-Butene on SnO<sub>2</sub> and TiO<sub>2</sub> Films. *J. Phys. Chem. B* 103, 2912-2917.
- Chang, M. B.; Kushner, M. J.; Rood, M. J. (1992). Gas Phase Removal of NO from Gas Stream via Dielectric Barrier Discharges. *Environ. Sci. Technol.* 26, 4, 777-781.
- Chein, H. -M.; Lundgren, D. A. (1995). A High-output, Size-selective Aerosol Generator. *Aerosol Sci. Technol.* 23, 510-520.
- Chen, C.; Bai, H.; Chang, S. -M.; Chang, C.; Den, W. (2007). Preparation of N-doped TiO<sub>2</sub> Photocatalyst by Atmospheric Pressure Plasma Process for VOCs Decomposition under UV and Visible Light Sources. *J. Nanoparticle Res.* 9, 365-375.
- Chen, D. -R.; Pui, D. Y. H.; Kaufman, S. L. (1995). Electrospraying of Conducting Liquids for Monodisperse Aerosol Generation in the 4 nm to 1.8 μm Diameter Range. *J. Aerosol Sci.* 26, 963-977.
- Chen, X.; Burda, C. (2004). Photoelectron Spectroscopic Investigation of Nitrogen-Doped Titania Nanoparticles. *J. Phys. Chem. B* 108, 15446-15449.
- Chen, X.; Lou, Y. -B.; Samia, A. C. S.; Burda, C.; Gole, J. L. (2005). Formation of Oxynitride as the Photocatalytic Enhancing Site in Nitrogen-Doped Titania Nanocatalysts: Comparison to a Commercial Nanopowder. *Adv. Funct. Mater.* 15, 41-49.
- Chen, X.; Mao, S. S. (2007). Titanium Dioxide Nanomaterials: Synthesis, Properties, Modifications, and Applications. *Chem. Rev.* 107, 2891-2959.
- Cho, K.; Biswas, P. (2006). Sintering Rates for Pristine and Doped Titanium Dioxide Determined Using a Tandem Differential Mobility Analyzer System. *Aerosol Sci. Technol.* 40, 309-319.
- d'Hennezel, O.; Pichat, P.; Ollis, D. F. (1998). Benzene and Toluene Gas-phase Photocatalytic Degradation over H<sub>2</sub>O and HCl Pretreated TiO<sub>2</sub>: by Products and Mechanisms. *J. Photochem. & Photobiol. A* 118, 197-204.
- Diebold, U. (2003). The Surface Science of Titanium Dioxide. *Surface Sci. Reports* 48, 53-229.

- Diwald, O.; Thompson, T. L.; Zubkov, T.; Goralski, Ed. G.; Walck, S. D.; Yates, J. T. Jr. (2004a). The Effect of Nitrogen Ion Implantation on the Photoactivity of TiO<sub>2</sub> Rutile Single Crystals. *J. Phys. Chem. B* 108, 52-57.
- Diwald, O.; Thompson, T. L.; Zubkov, T.; Goralski, Ed. G.; Walck, S. D.; Yates, J. T. Jr. (2004b). Photochemical Activity of Nitrogen-Doped Rutile TiO<sub>2</sub>(110) in Visible Light. *J. Phys. Chem. B* 108 , 6004 -6008.
- Di Valentin, C.; Pacchioni, G.; Selloni, A. (2004). Origin of the Different Photoactivity of N-doped Anatase and Rutile TiO<sub>2</sub>. *Phys. Rev. B* 70, 085116-085119.
- Di Valentin, C.; Pacchioni, G.; Selloni, A.; Livraghi, S.; Giamello, E. (2005). Characterization of Paramagnetic Species in N-Doped TiO<sub>2</sub> Powders by EPR Spectroscopy and DFT Calculations. *J. Phys. Chem. B* 109, 23, 11414 -11419.
- Duminica, F. -D.; Maury, F.; Senocq, F. (2004). Atmospheric Pressure MOCVD of TiO<sub>2</sub> Thin Films Using Various Reactive Gas Mixtures. *Surf. Coat. Technol.* 188-189, 255- 259.
- Esaka, F.; Furuya, K.; Shimada, H.; Imamura, M.; Matsubayashi, N.; Sato, H.; Nishijima, A.; Kawana, A.; Ichimura, H.; Kikuchi, T. (1997). Comparison of Surface Oxidation of Titanium Nitride and Chromium Nitride Films Studied by X-ray Absorption and Photoelectron Spectroscopy. *J. Vac. Sci. & Technol. A* 15, 5, 2521-2528.
- Evans, D. E.; Harrison, R. M.; Ayres, Je G. (2003). The Generation and Characterization of Metallic and Mixed Element Aerosols for Human Challenge Studies. *Aerosol Sci. Technol.* 37, 975-987.
- Foest, R.; Adler, F.; Sigener, F.; Schmidt, M. (2003). Study of an Atmospheric Pressure Glow Discharge (APG) for Thin Film deposition. *Surf. Coat. Technol.* 163 -164, 323-330.
- Francisco, H. I.; Berns, R. S.; Tzeng, Di-Y. (2000). A Comparative Analysis of Spectral Reflectance Estimated in Various Spaces using a Trichromatic Camera System. *J. Imaging Sci. Technol.* 44, 280-287.
- Friedlander, S.K. (2000). *Smoke, Dust and Haze: Fundamentals of Aerosol Dynamics*, 2<sup>nd</sup> ed.,

Oxford University Press, USA.

Fujishima, A.; Rao, T. N.; Tryk, D. A. (2000). Titanium Dioxide Photocatalysis. *J. Photochem. Photobiol. C: Photochem. Rev.* 1, 1-21.

Grätzel, M. (2001). Photoelectrochemical Cells. *Nature* 414, 338-344.

Gtill, A. (1992). *Cold Plasma in Materials Fabrication - From Fundamentals to Applications*. IEEE Press, New York.

Guillot, J.; Jouaiti, A.; Imhoff, L.; Domenichini, B.; Heintz, O.; Zerkout, S.; Mosser, A.; Bourgeois, S. (2002). Nitrogen Plasma Pressure Influence on the Composition of  $TiN_xO_y$  Sputtered Films. *Surf. & Interface Anal.* 34, 577-582.

György, E.; Pérez del Pino, A.; Serra, P.; Morenza, J.L. (2003). Depth Profiling Characterisation of the Surface Layer Obtained by Pulsed Nd:YAG Laser Irradiation of Titanium in Nitrogen. *Surf. and Coat. Technol.* 173, 265-270.

Hoffmann, M. R.; Martin, S. T.; Choi, W.; Bahnemann, D. W. (1995). Environmental Applications of Semiconductor Photocatalysis. *Chem. Rev.* 95, 69-96.

Horvath, H.; Gangl, G. (2003). A Low-voltage Spark Generator for Production of Carbon Particles. *J. Aerosol Sci.* 34, 1581-1588.

Huang, C. -M.; Chen, L. -C.; Cheng, K. -W.; Pan, G. -T. (2007). Effect of Nitrogen-plasma Surface Treatment to the Enhancement of  $TiO_2$  Photocatalytic Activity under Visible Light Irradiation. *J. Mol. Catal. A* 261, 218-224.

Ihara, T.; Miyoshi, M.; Iriyama, Y.; Matsumoto, M.; Sugihara, S. (2003). Visible-light-active Titanium Oxide Photocatalyst Realized by an Oxygen-deficient Structure and by Nitrogen Doping. *Appl. Catal. B* 42, 403-409.

Irie, H.; Watanabe, Y.; Hashimoto, K. (2003). Nitrogen-concentration Dependence on Photocatalytic Activity of  $TiO_{2-x}N_x$  Powders. *J. Phys. Chem. B* 107, 5483-5486.

Jill, C. Eds. *Handbook of X-ray Photoelectron Spectroscopy*, Perkin-Elmer Corp. Minnesota, (1992).

pp. 41-73.

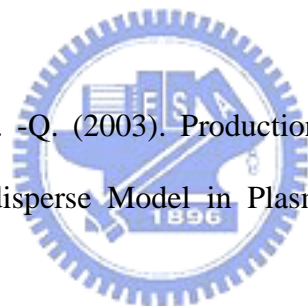
Jirsak, T.; Dvorak, J.; Rodriguez, J.A. (1999). Adsorption of NO<sub>2</sub> on Rh(111) and Pd/Rh(111): Photoemission Studies *Surf. Sci.* 436, L683-L690.

Joshi, S. V.; Liang, Q.; Park, J. Y.; Batdorf, J. A. (1990). Effect of Quenching Conditions on Particle Formation and Growth in Thermal Plasma Synthesis of Fine Powders. *Plasma Chem. Plasma Process.* 10, 2, 339-358.

Joung, S. -K.; Amemiya, T.; Murabayashi, M.; Itoh, K. (2006). Relation between Photocatalytic Activity and Preparation Conditions for Nitrogen-doped Visible Light-driven TiO<sub>2</sub> Photocatalysts. *Appl. Catal. A* 312, 20-26.

Kim, C. S.; Nakaso, K.; Xia, B.; Okuyama, K.; Shimada, M. (2005). A New Observation on the Phase Transformation of TiO<sub>2</sub> Nanoparticles Produced by a CVD Method. *Aerosol Sci. Technol.* 39, 104-112.

Kim, D. -J.; Kim, K. -S.; Zhao, Q. -Q. (2003). Production of Monodisperse Nanoparticles and Application of Discrete-monodisperse Model in Plasma Reactors. *J. Nanoparticle Res.* 5, 211-223.



Kitano, M. Matsuoka, M. Ueshima, M. Anpo, M. (2007). Recent Developments in Titanium Oxide-Based Photocatalysts. *Appl. Catal. A* 325, 1-14.

Kodas, T.T.; Hampden-Smith, M.J. (1999). *Aerosol Processing of Materials*, Wiley-VCH, New York.

Kulkarni, P.; Namiki, N.; Otani, Y.; Biswas, P. (2002). Charging of Particles in Unipolar Coronas Irradiated by In-situ Soft X-rays: Enhancement of Capture Efficiency of Ultrafine Particles. *J. Aerosol Sci.* 33, 1279-1296.

Kusters, K. A.; Pratsinis S. E. (1995). Strategies for Control of Ceramic Powder Synthesis by Gas-to-particle Conversion. *Powder Technol.* 82, 79-91.

Lee, D.; Choi, M. (2002). Coalescence Enhanced synthesis of Nanoparticles to Control Size, Morphology and Crystalline Phase at High Concentrations. *J. Aerosol Sci.* 33, 1-16.

- Lieberman, M. A.; Lichtenberg, A. J. (1994). *Principle of Plasma Discharges and Materials Processing*. John Wiley & Sons, Inc. New York.
- Li D.; Haneda, H.; Hishita, S.; Ohashi, N. (2005a). Visible-Light-Driven N-F-Codoped TiO<sub>2</sub> Photocatalysts. 2. Optical Characterization, Photocatalysis, and Potential Application to Air Purification. *Chem. Mater.* 17, 2596-2602.
- Li D.; Haneda, H.; Hishita, S.; Ohashi, N. (2005b). Visible-light-driven Nitrogen-doped TiO<sub>2</sub> Photocatalysts: Effect of Nitrogen Precursors on Their Photocatalysis for Decomposition of Gas-phase Organic Pollutants. *Mater. Sci. & Eng. B* 117, 67-75.
- Lin, C. -H.; Bai, H. (2001). Energy-effectiveness of Non-thermal Plasma Reactors for Toluene Vapor destruction. *ASCE J. Environ. eng.* 127, 7, 648-654.
- Livraghi, S.; Paganini, M. C.; Giamello, E.; Selloni, A.; Di Valentin, C.; Pacchioni G. (2006). Origin of Photoactivity of Nitrogen-Doped Titanium Dioxide under Visible Light. *J. Am. Chem. Soc.* 128, 15666-15671.
- Livraghi, S.; Votta, A.; Paganini, M. C.; Giamello, E. (2005). The Nature of Paramagnetic Species in Nitrogen Doped TiO<sub>2</sub> Active in Visible Light Photocatalysis. *Chem. Commun.* 498-500.
- Lu, F. -H.; Feng, S. -P.; Chen, H. -Y.; Li, J. -K. (2000). The Degradation of TiN Films on Cu Substrates at High Temperature under Controlled Atmosphere. *Thin Solid Films* 375, 123-127.
- Martin, S.; Massines, F.; Gherardi, N.; Jimenez, C. (2004). Atmospheric Pressure PE-CVD of Silicon Based Coatings Using a Glow Dielectric Barrier discharge. *Surf. Coat. Technol.* 177-178, 693-698.
- Maeda, M.; Watanabe, T. (2006). Visible Light Photocatalysis of Nitrogen-doped Oxide films Prepared by Plasma-enhanced Chemical Vapor Deposition. *J. Electrochem. Soc.* 153, 3, C186-C189.
- Miao, L.; Tanemura, S.; Watanabe, H.; Mori, Y. Kaneko; K.; Toh, S. (2004). The Improvement of Optical Reactivity for TiO<sub>2</sub> Thin Films by N<sub>2</sub>-H<sub>2</sub> Plasma Surface-treatment. *J. Crystal Growth* 260, 118-124.

- Mozia, S.; Tomaszewska, M.; Kosowska, B.; Grzmił, B.; Morawski, A. W.; Kalucki, K. (2005). Decomposition of Nonionic Surfactant on a Nitrogen-doped Photocatalyst under Visible-light Irradiation. *Appl. Catal. B* 55, 195-200.
- Musić S.; Gotić, M.; Ivanda, M.; Popvić, S.; Turković, A.; Trojko, R.; Sekulić, A.; Furić, K. (1997). Chemical and Microstructural Properties of TiO<sub>2</sub> Synthesized by Sol-gel Procedure. *Mater. Sci. Eng. B* 47, 33-40.
- Nakade, S.; Matsuda, M.; Kambe, S.; Saito, Y.; Kitamura, T.; Sakata, T.; Wada, Y.; Mori, H.; Yanagida, S. (2002). Dependence of TiO<sub>2</sub> Nanoparticle Preparation Methods and Annealing Temperature on the Efficiency of Dye-sensitized Solar Cells. *J. Phys. Chem. B* 106, 10004-10010.
- Nakamura, I.; Negishi, N.; Kutsuna, S.; Ihara, T.; Sugihara, S.; Takeuchi, K. (2000). Role of Oxygen Vacancy in the Plasma-treated TiO<sub>2</sub> Photocatalyst with Visible Light Activity for NO Removal. *J. Mole. Catal. A* 161, 205-212.
- Nakaso, K.; Fujimoto, T.; Seto, T.; Shimada, M.; Okuyama, K.; Lunden, M. M. (2001). Size Distribution Change of Titania Nano-particle Agglomerates Generated by Gas Phase Reaction, Agglomeration, and Sintering. *Aerosol Sci. Technol.* 35, 929-947.
- Nakaso, K.; Han, B.; Ahn, K. H.; Choi, M.; Okuyama, K. (2003a). Synthesis of Non-agglomerated Nanoparticles by an Electrospray Assisted Chemical Vapor Deposition (ES-CVD) Method. *J. Aerosol Sci.* 34, 869-881.
- Nakaso, K.; Okuyama, K.; Shimada, M.; Pratsinis, S. E. (2003b). Effect of Reaction Temperature on CVD-made TiO<sub>2</sub> Primary Particle Diameter. *Chem. Eng. Sci.* 58, 3327-3335.
- Ni, M.; Leung, M. K. H.; Leung, D. Y. C.; Sumathy, K. (2007). A Review and Recent Developments in Photocatalytic Water-splitting Using TiO<sub>2</sub> for Hydrogen Production. *Renewable & Sustainable Energy Rev.* 11, 401-425.
- Nosaka Y.; Matsushita, M.; Nishino, J.; Nosaka, A. Y. (2005). Nitrogen-doped Titanium Dioxide Photocatalysts for Visible Response Prepared by Using Organic Compounds. *Sci. & Technol.*

*Adv. Mater.* 6, 143-148.

Okuyama, K.; Kousaka, Y.; Tohge, N.; Yamamoto, S.; Wu, J. J.; Flagan, R. C.; Seinfeld, J. H. (1986). Production of Ultrafine Metal Oxide Aerosol Particles by Thermal Decomposition of Metal Alkoxide Vapors. *A.I.Ch.E.* 32, 2010-2019.

Okuyama, K.; Ushio, R.; Kousaka, Y.; Flagan, R. C.; Seinfeld, J. H. (1990). Particle Generation in a Chemical Vapor Deposition Process with Seed Particles. *A.I.Ch.E.* 36, 409-419.

Park, K.Y.; Ullmann, M.; Suh, Y.J.; Friedlander, S.K. (2001). Nanoparticle microreactor: Application to Synthesis of Titania by Thermal Decomposition of Titanium Tetraisopropoxide. *J. Nanoparticle Res.* 3, 309-319.

Pratsinis, S. E.; Zhu, W.; Vemury, S. (1996). The Role of Gas Mixing in Flame Synthesis of Titania Powder. *Powder Technol.* 87, 87-93.

Pratsinis, S. E.; Spicer, P. T. (1998). Competition between Gas Phase and Surface Oxidation of  $TiCl_4$  during Synthesis of  $TiO_2$  Particles. *Chem. Eng. Sci.* 53, 10, 1861-1868.

Peineke, C.; Attoui, M.B.; Schmidt-Ott, A. (2006). Using a Glowing Wire Generator for Production of Charged, Uniformly Sized Nanoparticles at High Concentrations. *J. Aerosol Sci.* 37, 1651-1661.

Prenni, A. J.; Siefert, R. L.; Onasch, T. B.; Tolbert, M. A.; DeMott, P. J. (2000). Design and Characterization of a Fluidized Bed Aerosol Generator: A Source for Dry, Submicrometer Aerosol. *Aerosol Sci. Technol.* 32, 465-481.

Ramis, G.; Busca, G.; and Lorenzelli, V. (1987). Structural Effects on the Adsorption of Alcohols on Titanium Dioxides. *J. Chem Soc. Farad. Transac.*, 83, 1591-1599.

Rodriguez, J. A.; Jirsak, T.; Dvorak, J.; Sambasivan, S.; Fischer, D. (2000). Reaction of  $NO_2$  with Zn and ZnO: Photoemission, XANES, and Density Functional Studies on the Formation of  $NO_3$ . *J. Phys. Chem. B* 104, 319-328.

Saha, N. C.; Tompkins, H. G. (1992). Titanium Nitride Oxidation Chemistry: An x-ray Photoelectron Spectroscopy Study. *J. Appl. Phys.* 72, 7, 3072-3079.



- Sakatani Y.; Ando, H.; Okusako, K.; Koike, H. (2004). Metal ion and N Co-doped TiO<sub>2</sub> as a Visible-light Photocatalyst. *J. Mater. Res.* 19, 2100-2108.
- Sano, T.; Koike, N.; Negishi, K.; Takeuchi, K.; Matsuzawa, S. (2004). Preparation of a Visible Light-responsive Photocatalyst from a Complex of Ti<sup>4+</sup> with a Nitrogen-containing Ligand. *J. Mater. Chem.* 14, 380-384.
- Sato, S.; Nakamura, R.; Abe, S. (2005). Visible-light Sensitization of TiO<sub>2</sub> Photocatalysts by Wet-method N doping. *Appl. Catal. A* 284, 131-137.
- Seto, T.; Shimada, M.; Okuyama, K. (1995). Evaluation of Sintering of Nanometer-sized Titania Using Aerosol Method. *Aerosol Sci. Technol.* 23, 183-200.
- Suda Y.; Kawasaki, H.; Ueda, T.; Ohshima, T. (2005). Preparation of Nitrogen-doped Titanium Oxide Thin Film Using a PLD Method as Parameters of Target Material and Nitrogen Concentration Ratio in Nitrogen/Oxygen Gas Mixture. *Thin Solid Films* 475, 337-341.
- Spicer, P. T.; Chaoul, O.; Tsantilis, S.; Pratsinis, S. E. (2002). Titania Formation by TiCl<sub>4</sub> Gas Phase Oxidation, Surface Growth and Coagulation. *J. Aerosol Sci.* 33, 17-34.
- Thompson, T. L.; Yates, J. T. Jr. (2006). Surface Science Studies of the Photoactivation of TiO<sub>2</sub>--New Photochemical Processes. *Chem. Rev.* 106, 4428-4453.
- Thyen, R.; Weber, A.; Klages, C. -P. (1997). Plasma-enhanced Chemical-vapor-deposition of Thin Films by Corona Discharge at Atmospheric Pressure. *Surf. Coat. Technol.* 97, 426-434.
- Tsantilis, S.; Kammler, H. K.; Pratsinis, S. E. (2002). Population Balance Modeling of Flame Synthesis of Titania Nanoparticles. *Chem. Eng. Sci.* 57, 2139-2156.
- Tsantilis, S.; Pratsinis, S. E. (2004a). Narrowing the Size Distribution of Aerosol-Made Titania by Surface Growth and Coagulation. *J. Aerosol Sci.* 35, 405-420.
- Tsantilis, S.; Pratsinis, S. E. (2004b). Soft- and Hard-agglomerate Aerosols Made at High Temperatures. *Langmuir.* 20, 5933-5939.
- Umebayashi, T.; Yamaki, T.; Yamamoto, S.; Miyashita, A.; Tanaka, S.; Sumita, T.; Asai, K. (2003). Sulfur-doping of Rutile-titanium Dioxide by Ion Implantation: Photocurrent Spectroscopy and

- First-principles Band calculation studies. *J. Appl. Phys.* 93, 5156-5160.
- Vemury, S.; Kusters, K. A.; Pratsinis, S. E. (1994). Time-lag for Attainment of the Self-Preserving Particle-Size Distribution by Coagulation. *J. Colloid Interf. Sci.* 165, 1, 53-59.
- Veranth, J. M.; Gelein, R.; Oberdörster, G. (2003). Vaporization-condensation Generation of Ultrafine Hydrocarbon Particulate Matter for Inhalation Toxicology Studies. *Aerosol Sci. Technol.* 37, 603-609.
- Wang, S.; Ang, H. M.; Tade, M. O. (2007). Volatile Organic Compounds in Indoor Environment and Photocatalytic Oxidation: State of the art. *Environ. Int.* 33, 694-705.
- Wang, Y.; Feng, C.; Jin, Z.; Zhang, J.; Yang, J.; Zhang, S. (2006). A Novel N-doped TiO<sub>2</sub> with High Visible Light Photocatalytic Activity. *J. Mole. Catal. A* 260, 1-3.
- Wang, Z. -M.; Yang, G.; Biswas, P.; Bresser, W.; Boolchand, P. (2001). Processing of Iron-doped Titania Powders in Flame Aerosol Reactors. *Powder Technol.* 114, 197-204.
- Wawrzyniak, B.; Morawski, A. W. (2006). Solar-light-induced Photocatalytic Decomposition of Two Azo Dyes on New TiO<sub>2</sub> Photocatalyst Containing Nitrogen. *Appl. Catal. B* 62, 150-158.
- Wu, P. -G.; Ma, C. -H.; Shang, J. K. (2005). Effects of Nitrogen Doping on Optical Properties of TiO<sub>2</sub> Thin Films. *Appl. Phys. A* 81, 1411-1417.
- Wu, H. Z.; Chou, T. C.; Mishra, A.; Anderson, D. R.; Lampert, J. K.; Gujrathi, S. C. (1990). Characterization of Titanium Nitride Thin Films. *Thin Solid Films* 191, 55-67.
- Yang, G.; Zhuang, H.; Biswas, P. (1996). Characterization and Sinterability of Nanophase Titania Particles Processed in Flame Reactors. *NanoStructured Mater.* 7, 6, 675-689.
- Yang, M. -C.; Yang, T. -S.; Wong, M. -S. (2004). Nitrogen-doped Titanium Oxide Films as Visible Light Photocatalyst by Vapor Deposition. *Thin Solid Films* 469-470, 1-5.
- Yang, T.-S.; Shiu, C.-B.; Wong, M.-S.; (2004). Structure and Hydrophilicity of Titanium Oxide Films Prepared by Electron Beam Evaporation. *Surface Sci.* 548, 75-82.
- Yin, S.; Aita, Y.; Komatsu, M.; Wang, J.; Tang, Q.; Sato, T. (2005). Synthesis of Excellent Visible-light Responsive TiO<sub>2-x</sub> N<sub>y</sub> Photocatalyst by a Homogeneous Precipitation-

solvothermal Process. *J. Mater. Chem.* 15, 674-682.

Yin, S.; Ihara, K.; Aita, Y.; Komatsu, M.; Sato, T. (2006). Visible-light Induced Photocatalytic Activity of  $\text{TiO}_{2-x}\text{A}_y$  (A = N, S) Prepared by Precipitation Route. *J. Photochem. Photobiol. A* 179, 105-114.

Yin, Y.; Alivisatos, A. P. (2005). Colloidal Nanocrystal Synthesis and the Organic–inorganic Interface. *Nature* 437, 664-670.

Zhang, H.; Banfield, J. F. (2000). Phase Transformation of Nanocrystalline Anatase-to-rutile via Combined Interface and Surface Nucleation. *J. Mater. Res.* 15, 437-448.

Zimmer, A. T.; Baron, P. A.; Biswas, P. (2002). The Influence of Operating Parameters on Number-weighted Aerosol Size Distribution Generated from a Gas Metal Arc Welding Process. *J. Aerosol. Sci.* 33, 519-531.

